TRANSVERSE FATIGUE CRACK DIAGNOSIS IN A ROTORDYNAMIC SYSTEM USING VIBRATION MONITORING

A Thesis
Presented to
The Academic Faculty

by

Philip A. Varney

In Partial Fulfillment
of the Requirements for the Degree
Master of Science in the
Woodruff School of Mechanical Engineering

Georgia Institute of Technology
May 2013

TRANSVERSE FATIGUE CRACK DIAGNOSIS IN A ROTORDYNAMIC SYSTEM USING VIBRATION MONITORING

Approved by:

Dr. Itzhak Green, Advisor
Woodruff School of Mechanical Engineering
Georgia Institute of Technology

Dr. Aldo Ferri
Woodruff School of Mechanical Engineering
Georgia Institute of Technology

Dr. Michael Leamy
Woodruff School of Mechanical Engineering
Georgia Institute of Technology

Dr. Brad Miller
Department of Engineering and Physics
Harding University

Date Approved: 28 March 2013

ACKNOWLEDGEMENTS

First and foremost, I would like to acknowledge and thank Dr. Itzhak Green for his continued support and thoughtful advice concerning the completion of this work. In addition, I would like to thank the mechanical engineering faculty at Harding University for their dedication to the education of their students and their impetus in encouraging me to seek a graduate degree. In particular I am grateful to Dr. Brad Miller, who went above and beyond to offer additional dynamics and vibration courses, thus imparting the skills, knowledge, and appreciation for the subject necessary for me to pursue a project focused on rotordynamics and vibrations. This research was conducted under support from National Science Foundation Grant No. 1100101.

TABLE OF CONTENTS

LIST OF TABLES

LIST OF FIGURES

NOMENCLATURE

a	Crack depth.
b	Crack half-width.
$[C]$	Compliance matrix.
$[D]$	Damping matrix.
$[E]$	Matrix containing centripetal terms.
E	Elastic modulus.
$\{F\}$	Vector of applied forces.
$[F]$	Field matrix.
$[G]$	Gyroscopic matrix.
I	Area moment of inertia of uncracked shaft.
I_j^C	Area moment of inertia of notched section about axis j.
I_p	Polar mass moment of inertia of rotor.
I_t	Transverse mass moment of inertia of rotor.
$J(y)$	Strain energy release rate.
L	Length of the undamaged shaft.
L_1	Length of shaft to the left of the crack.
L_2	Length of shaft to the right of the crack.
L_C	Length of notched section.
m	Mass of the overhung rotor.
m_ϵ	Imbalance mass.
$[M]$	Mass matrix.
M_j	Bending moment about axis j.
n	Shaft speed of system.
p	Inertial frame eigenvalue.
$[P]$	Point matrix.

P_i	Load applied in the direction of axis i.
p_r	Rotating frame eigenvalue.
$\{q\}$	Vector of rotor degrees of freedom.
R	Radius of shaft.
$\{S\}_j$	State vector at j^{th} node.
$[U]$	Overall transfer matrix.
u_x	Deflection of the rotor in the X direction.
u_y	Deflection of the rotor in the Y direction.
V_j	Shear force in direction of axis j.
XYZ	Rotating reference frame attached to hypothetical rotating undeflected shaft.

Greek Symbols:

α	Local crack depth along crack edge.
β	Proportional damping coefficient.
ϵ	Imbalance radius from rotor's geometric center.
γ	Total inertial frame angular response of the rotor.
γ_x	Rotation of the rotor about the X axis.
γ_y	Rotation of the rotor about the Y axis.
ψ_j	Right eigenvector j.
$\tilde{\psi}_j$	Left eigenvector j.
ν	Poisson ratio.
θ	Imbalance orientation from rotor body-fixed axes.
$\{\xi\}$	Vector of decoupled state space coordinates.
Ψ_j	Mass normalized eigenvector j.
$\xi\eta\zeta$	Inertial reference frame.

SUMMARY

To increase efficiency, shafts are made lighter and more flexible, and are designed to rotate faster to increase the system's power-to-weight ratio. The demand for higher efficiency in rotordynamic systems has led to increased susceptibility to transverse fatigue cracking of the shaft. Shaft cracks are often detected and repaired during scheduled periods of off-line maintenance. Off-line maintenance can be expensive and time consuming; on-line condition monitoring allows maintenance to be performed as-needed. However, inadequate (or a lack of) monitoring can allow rapidly propagating cracks to result in catastrophic shaft failure. It is therefore imperative to develop on-line condition monitoring techniques to detect a crack and diagnose its severity. A particularly useful method for transverse shaft crack detection/diagnosis is vibration monitoring.

Detection, and especially diagnosis, of transverse fatigue cracks in rotordynamic systems has proven difficult. Whereas detection assesses only the presence of a crack, diagnosis estimates important crack parameters, such as crack depth and location. Diagnosis can provide the operator with quantitative information to assess further machinery operation. Furthermore, diagnosis provides initial conditions and predictive parameters on which to base prognostic calculations.

There is a two-fold challenge for on-line diagnosis of transverse fatigue crack parameters. First, crack characterization involves specifying two important parameters: the crack's depth and location. Second, the nature of rotating machinery permits response measurement at only specific locations.

Cracks are typically categorized as breathing or gaping; breathing cracks open and close with shaft rotation, while gaping cracks remain open. This work concerns the diagnosis of gaping crack parameters; the goal is to provide metrics to diagnose a crack's depth and location. To this end, a comprehensive approach is presented for modeling an overhung cracked shaft. Two linear gaping crack models are developed: a notch and a gaping fatigue crack. The notch model best approximates experimentally manufactured cracks, whereas the gaping fatigue crack model is likely more suited for real fatigue cracks.

Crack diagnosis routines are established using free and forced response characteristics. Equations of motion are derived for both crack models, including excitation due to gravity and imbalance. Transfer matrix techniques are established to expediently obtain the steady-state system response. A novel transfer matrix technique, the Complex Transfer Matrix, is developed to distinguish forward and backward whirl components. The rotor's angular response is primarily employed in this work for crack detection and diagnosis. The overhung shaft induces an increased sensitivity to variations in crack depth and location. In addition, an available overhung rotordynamic experimental test rig allows for comparison of the current analytic results to previously obtained experimental results.

Under the influence of gravity, the steady-state response of the cracked system includes a prominent 2X harmonic component, appearing at a frequency equal to twice the shaft speed. The magnitude of the 2X harmonic is strongly influenced by the shaft speed. A resonant response occurs when the shaft speed reaches half of a system natural frequency. This work demonstrates that the profile of the 2X harmonic versus shaft speed is a capable diagnostic tool. Identification of the 2X resonance frequency restricts the crack parameters to certain pairs of location and depth. Following this limiting process, the magnitude of the 2X harmonic is used to identify the crack's depth and location. Orbital shapes at the rotor are discussed, as are orbital modes of the shaft deflection. Quantitative results and qualitative observations are provided concerning the difficulty of crack detection and diagnosis.

CHAPTER I

INTRODUCTION

Safe and economical operation of rotordynamic machinery necessitates adherence to condition monitoring protocols. Condition monitoring assesses machinery health on a periodic or continuous schedule to ensure continued successful operation. In rotordynamic systems, condition monitoring is categorized as off-line or on-line. Off-line condition monitoring is performed when the shaft has ceased rotation. Various off-line condition monitoring methods exist, including visual inspection, ultrasound techniques, static deflection tests, etc. These off-line condition monitoring techniques require inspection and maintenance be performed on a periodic schedule, imposing lengthy periods of costly downtime.

On-line condition monitoring is executed during normal (or pseudo-normal) operation; costly and time-consuming downtime is therefore avoided. Pseudo-normal operation entails deviation from normal operating conditions (for example, varying the shaft speed away from the normal operational speed). This pseudo-normal running up and coasting down can provide valuable diagnostic information. Another pseudo-normal form of condition monitoring involves exciting the system to observe the transient response.

Judicious application of on-line condition monitoring for rotating machinery imparts numerous benefits to the operator. First, repairs can be made on an as-needed basis rather than relying on scheduled periodic maintenance. The cost associated with scheduled maintenance is often immense for large turbo-machinery systems, such as power-generating steam turbines. Second, on-line condition monitoring can provide a real-time diagnosis of fault severity. Based on the fault's severity, the operator can

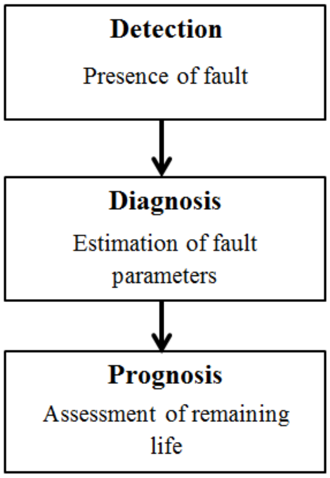

Figure 1.1: Relationship between detection, diagnosis, and prognosis

make an informed decision on whether to continue operation or repair the machine. Third, on-line condition monitoring decreases the probability of catastrophic failure by providing a continuous assessment of fault progression.

Three levels of condition monitoring systems exist, according to their respective objectives: detection, diagnosis, and prognosis. The relationship between detection, diagnosis, and prognosis is summarized in Fig. 1.1. Detection is a binary fault judgment; the condition monitoring system only indicates the presence of a fault, and a signal indicating a fault is sufficient for the operator to take corrective action. Diagnosis improves upon detection by estimating the parameters of a fault, and is the focus of this work. For example, a rotordynamic crack detection condition monitoring system would alert the operator to the mere presence of a crack, whereas diagnosis would also provide an estimate of the fault parameters (i.e., crack depth and location). Prognosis is the most advanced stage of condition monitoring, and adds to diagnosis by employing the fault parameters to assess the machinery's remaining life. To continue with the example, prognosis would estimate the number of cycles remaining until crack propagation resulted in shaft failure.

Rotordynamic systems are susceptible to mechanical faults in several key areas:

bearings, seals, lubrication, and the shaft or rotor. The type of condition monitoring system employed depends on the type of fault expected. For example, oil analysis has proven well-suited for the detection and diagnosis of bearing faults and lubrication issues, while vibration monitoring is used to diagnose faults associated with the shaft or rotor. The wide array of rotordynamic faults has led to a broad range of condition monitoring techniques.

The aspiration of any on-line condition monitoring system should be multiple fault detection and diagnosis. Multiple fault condition monitoring describes a system that can detect or diagnose significantly different faults, such as mechanical seal face contact and transverse fatigue cracks. The difficulty of multiple fault condition monitoring is that different faults often produce similar signatures when observed with the same monitoring technique, such as vibration monitoring. A synthesis of monitoring techniques is therefore often employed to distinguish different faults. However, simplicity and comparatively lower cost makes single-source condition monitoring attractive and often advantageous.

The first step in developing an on-line condition monitoring system is to characterize each fault. Multiple fault detection and diagnosis is possible only if each fault is individually understood. The methods used to detect and diagnose each fault serve as one facet of multiple fault condition monitoring. Only when the facets are assembled is successful multiple fault detection attainable. The current work focuses on one facet in particular: transverse fatigue cracking of the rotating shaft.

Transverse fatigue cracking of the shaft in a rotordynamic system is an increasingly common problem. To increase efficiency, shafts are being made lighter and more flexible, and they are designed to rotate faster to increase the system's power-to-weight ratio. This demand for increased efficiency of modern rotordynamic systems heightens susceptibility to transverse fatigue cracking of the shaft. Shaft cracking is particularly dangerous, as cracks are often difficult to detect until latter stages of propagation. Severe cracks can result in catastrophic shaft failure, an exceptionally dangerous and expensive event. The ability to detect and diagnose transverse shaft cracks soon after their onset is a vital component of any rotordynamic condition monitoring system.

Vibration monitoring has proven to be a capable tool for fault detection and diagnosis [1, 2]. Vibration monitoring directly observes the system's forced response; in rotordynamic systems, forcing typically arises from gravity or imbalance. In this work, monitoring the dynamic response of a system is referred to as vibration monitoring, due to identical measurement procedures and terminology. In rotordynamics, the presence of a fault in conjunction with forcing (such as gravity) often generates shaft speed harmonics occurring at integer multiples of the shaft speed. Most works using vibration monitoring to detect rotordynamic faults employ these harmonics. The primary goal of this work is to employ vibration monitoring to detect a transverse fatigue crack and diagnose its parameters.

The success of an on-line crack diagnosis regimen hinges on the accuracy of the crack model employed. Cracks are typically categorized as either gaping or breathing. As the name suggests, gaping cracks remain open throughout rotation of the shaft, resulting in a stiffness asymmetry which is time-invariant in a shaft-fixed rotating reference frame. Contrary to gaping cracks, breathing cracks open and close periodically as a function of shaft rotation. The breathing behavior of the crack results in a time periodic stiffness asymmetry even in a shaft-fixed reference frame. Regardless of whether the crack is gaping or breathing, the crack model should account for the crack's depth and location, as both can have a profound impact on detection and diagnosis. Negating the influence of crack location ignores a crucial component of real cracks.

An on-line vibration monitoring procedure is proposed herein to assist in diagnosing the location and depth of a gaping transverse shaft crack. A gaping crack is selected for the analysis to provide a well-understood feasibility benchmark. It is hypothesized that if the condition monitoring techniques are successful for gaping cracks, the same techniques can be extended to incorporate breathing behavior. An overhung rotordynamic system is employed to emulate an available novel rotordynamic test rig capable of extracting the rotor's dynamic angular response. The overhung model is selected for several reasons. First, the model's simplicity allows the crack's influence to be easily isolated. In addition, the rotor's overhung nature induces prominent gyroscopic effects, the magnitude of which assists in experimentally measuring the rotor's response. Similarly, the system is relatively flexible compared to a similar simply-supported shaft; the crack's influence on the dynamic response is therefore easier to measure experimentally.

This introduction chapter presents concepts fundamental to rotordynamic condition monitoring. The problem of detection and diagnosis of transverse shaft cracks in rotordynamic systems is motivated through its applicability to on-line multiple fault detection. The difficulties and rewards of successful multiple fault detection are elucidated, including a brief introduction to various crack models.

Works relevant to transverse shaft crack detection and diagnosis are reviewed in Chapter 2. Furthermore, Chapter 2 examines the history of research leading to this work, with particular emphasis on mechanical face seal detection. Various crack models are discussed, as well as numerical and analytical techniques used to analyze the crack models. Previous attempts to detect and diagnose transverse shaft cracks using experimental methods are provided. Shortcomings of previous developments are highlighted in relation to the goals of this work.

Chapter 3 develops two crack models: a finite-width rectangular notch and a true gaping fatigue crack. A model of an undamaged (i.e., healthy) rotordynamic system is first presented to provide a consistent framework for formulating the dynamics of the system. By using a consistent dynamic framework, the differences between the crack models can be isolated and investigated. Basic characteristics of each crack model are discussed, as well as the global stiffness of the overhung rotordynamic system displaying each crack. The dynamic interplay between crack depth and location is emphasized throughout. The previously constructed overhung rotordynamic test rig is summarized, along with pertinent test rig parameters used in the analysis (Chapters 5 and 6 give a comparison to previously obtained experimental results).

The transfer matrix method is developed in Chapter 4. The method is a numeric technique particularly useful for analyzing rotordynamic systems. Various transfer matrix methods are presented, including transfer matrices corresponding to each crack model. The advantages of transfer matrix methods are discussed. A novel transfer matrix technique, the Complex Transfer Matrix, is developed to alleviate several concerns typically associated with real-valued transfer matrix analysis (such as the inability to distinguish forward and backward whirl).

Free and forced analytic results are presented in Chapters 5 and 6, respectively. Results for both the notch and gaping fatigue crack are provided. Furthermore, two cases for each crack model are examined: the first investigates a fixed-location crack, while the second examines variations in both crack depth and location. Beyond providing insight into the influence of crack depth, the fixed-location results allow comparison to experimental and analytic results given by Green and Casey [1] and Varney and Green [2]. The equations of motion are placed in a state-space form and decoupled to provide for expedient solution. Expedient solution is crucial, as the equations are solved for many combinations of crack locations and depths over a range of shaft speeds. In addition, transformations necessary to move between the rotating and inertial reference frames are developed. The influence of crack depth and location on the system response is emphasized throughout Chapters 5 and 6.

The results from Chapters 5 and 6 are applied to crack detection and diagnosis strategies in Chapter 7 (experimental implementation is left for future work). A method employing the profile of the 2X harmonic versus shaft speed is used to diagnose crack depth and location. Practical considerations, qualitative observations, and trends relevant for crack diagnosis are discussed.

The conclusions of the work, as well as avenues for further research, are provided in Chapter 8.

CHAPTER II

LITERATURE SURVEY

In the past several decades, a large volume of work has been performed on the modeling and detection of transverse shaft cracks in rotordynamic systems. Beginning in the 1960's, several researchers (most notably A. D. Dimarogonas) began developing methods to detect transverse shaft cracks in the rotors of large steam turbines. Since this preliminary investigation, significant gains have been made towards modeling cracked rotordynamic systems and creating methods to accurately detect these cracks shortly after initiation. The contributions of this work are discussed herein in relation to this diverse body of previous research.

Efforts to increase the efficiency and power output of rotordynamic systems have led to lighter and more flexible shafts designed to rotate faster. These changes increase the propensity for transverse fatigue cracking, which can lead to catastrophic failure if not detected at an early stage. Catastrophic shaft failure must be avoided, from the perspective of both safety and economy. Bently and Muszynska [3] state that from 1976 to 1986, 28 significant rotor failures due to shaft cracking occurred in the United States power industry. The review by Sabnavis et al. [4] states that the Electric Power Research Institute estimates the financial losses due to shaft cracking in the power industry at approximately US $1 billion. A successful and widely adaptable crack detection and diagnosis routine is thus invaluable.

The relation of this work to research performed on seal face dynamics is first discussed to contextualize the contribution of the present work.

2.1 Mechanical Face Seal Dynamics

The current work on transverse shaft crack detection is an outgrowth of research performed over the past two decades investigating the dynamics of a flexibly mounted rotor (FMR) mechanical face seal system. In the 1980's and early 1990's, non-contacting mechanical face seals were increasingly employed in high performance turbomachinery applications. Though designed and utilized for their hypothetical long life and reliability, non-contacting mechanical face seals were found to be susceptible to premature failure. The dynamics of the non-contacting mechanical face seal were thoroughly investigated in an effort to understand these seemingly random failures.

The underlying kinematic model of the seal is essential to any work investigating mechanical face seal dynamics. Green and Etsion [5] develop a kinematic model for two seal types: a flexibly-mounted rotor (FMR) and flexibly-mounted stator (FMS) seal configuration. Green [6] greatly expands upon the model by drawing a comparison to the kinematic equivalence of the space cone/body cone system. These kinematic models, valid for many arrangements of anti-rotation and positive drive devices, mathematically state that a constraint exists which forces corresponding points on the seal rings to return to their original relative position following the completion of each revolution of relative whirl. An integral contribution of their investigation to this work is the presentation of the flexibly mounted rotor's angular momentum.

Until the early 1990's, much of the work concerning mechanical face seals did not consider coupling of the shaft and seal dynamics. Lee and Green [7] develop a seminal work on this subject, presenting the Complex Extended Transfer Matrix (CETM) for investigating the coupled dynamics of a flexible shaft and a non-contacting mechanical face seal riding on the shaft. The CETM is a transfer matrix technique allowing for the inclusion of forcing (and thus, coupling) through an expansion of the system field and point matrices (as summarized in Chapter 4). The CETM technique allows for a numerical solution of the system dynamics at a given shaft speed, and thus provides

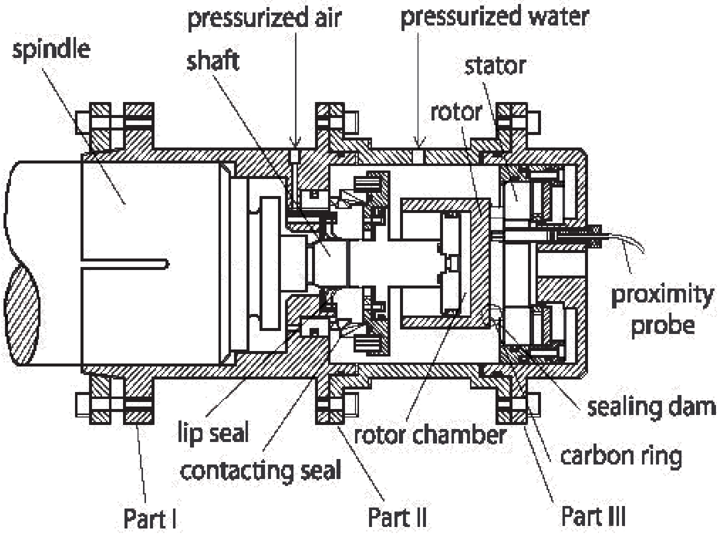

Figure 2.1: Overhung rotordynamic test rig

a powerful tool for analyzing forced rotordynamic systems.

Following the development of the CETM, an overhung FMR non-contacting mechanical face seal test rig was constructed to investigate the mechanical face seal dynamics experimentally [8] (the rotordynamic model used in this work emulates the overhung test rig). Though only a summary is given here, the characteristics of the test rig, as well as the data collection and analysis techniques, are discussed extensively by Lee and Green [9]. The test rig consists of an overhung shaft with a flexibly mounted rotor, as shown in Fig. 2.1. A carbon ring mounted on the rotor, in conjunction with a cone-faced stator, forms a non-contacting mechanical face seal. Hydrostatic effects generated by a water pump system are used to separate the faces, while an air pressure supply maintains seal clearance. The angular response of the rotor is extracted by a system of three stator-mounted eddy-current proximity probes.

During construction and testing of the experimental test rig, a unique vibratory phenomenon was observed. In the steady-state rotor response, higher harmonic oscillations occurring at frequencies equal to integer multiples of the shaft speed appeared in the power spectral density (PSD) of the rotor's response [8]. Furthermore, the periodic nature of these higher harmonic oscillations indicated that they originated from the system operation itself rather than random noise. Following experimental component isolation tests and an analytic investigation of non-linear effects, it was determined that the higher harmonic oscillations were generated by seal face contact. Similarities between an analytic Fourier analysis and the measured response were used to verify the likelihood of seal face contact. In addition, specific changes to the test rig were successfully employed to reduce the possibility of seal face contact, thus eliminating higher harmonic oscillations from the response.

Seal failure is often precipitated by excessive seal face wear induced by rubbing contact. Therefore, a seal condition monitoring system could incorporate seal face contact detection to mitigate premature seal failure. Condition monitoring implies real-time data collection and analysis to accurately detect the onset of a fault. Zou et al. [10] modify the aforementioned test rig to allow real-time monitoring of the rotor's angular response. Furthermore, the angular orbit is introduced as a tool to assist in real time seal face contact detection. Whereas a typical orbit gives a trace of the rotor center as the shaft whirls (i.e., lateral deflections), an angular orbit provides a trace of the rotor tilt (i.e., the path traced by the tip of a vector formed by the orthogonal components of the rotor tilt).

Zou et al. [11] use two qualitative response signatures to detect seal face contact: sudden deviation of the angular response orbit from a circular shape, and an increase in the energy of the 2X and 3X higher harmonic oscillation peaks in the PSD. Once detected, seal face contact must be remedied to avoid eventual seal failure. Zou and Green [10] introduce a PI controller to maintain the clearance of the seal to a set of prescribed values. Following this development, a feasibility study is performed showing that contact can be eliminated through real time control of the seal clearance [12]. Dayan et al. [13] develop an actively controlled contact elimination system to eliminate seal face contact and reduce seal leakage.

Rotordynamic systems are susceptible to many faults of vastly differing natures. Thus, a successful condition monitoring system should be capable of detecting and diagnosing a myriad of different faults. For simplicity and economy, it is desirable that the system employ the same signal (e.g., angular response of the rotor) to detect different faults. However, the difficulty in single-signal multiple fault detection is that vastly different faults can generate similar response attributes. For example, a transverse shaft crack also induces higher harmonic oscillations in a similar manner to mechanical face seal contact.

Green and Casey [1] advance the aforementioned research by studying the feasibility of using the current seal face contact detection system to detect a transverse shaft crack. A gaping shaft crack (as will be discussed shortly) is introduced, and the rotor's angular response is obtained analytically and experimentally. Green and Casey conclude that simultaneous detection of seal face contact and shaft cracks is feasible due to differences in the angular response orbit; particularly, that the level of orbit asymmetry is much greater for a cracked system than a system undergoing mechanical face seal contact. The work by Green and Casey on transverse shaft crack detection serves as the genesis of the current work.

The discussion of the research directly leading to this work serves several purposes. Foremost, the evolution of the prior work (from investigation to multiple fault detection) contextualizes the desired outcome of the present work: to place a 'piece' into the puzzle of rotordynamic multiple fault detection. Second, the works highlighted above provide an invaluable resource for understanding the basis of the rotordynamic model employed in this work, as the models here emulate the test rig discussed above. Finally, the work on seal face contact detection provides a model for designing detection systems concerning other faults, from concept inception and analytical work to experimental work and real fault detection.

2.2 Modeling Transverse Shaft Cracks

The ability of a condition monitoring system to detect and diagnose transverse shaft cracks hinges on how well the crack model emulates the actual cracked system: the model must capture the same behavior on which the condition monitoring system relies. The key aspect of any crack model is the reduction in stiffness introduced by the crack. The localized reduction in stiffness is directly related to crack depth, whereas the global reduction in stiffness is influenced by both crack depth and crack location along the shaft. Unfortunately, many researchers opt to either ignore crack location or mitigate its effects.

Transverse shaft cracks are typically categorized as either gaping or breathing. Gaping cracks remain open regardless of the shaft's angular orientation; the faces of the crack never contact [14]. A breathing crack is defined by the opening and closing behavior of the crack faces. As such, the shaft's stiffness is a function of its angular orientation. Breathing cracks are often modeled as having either smoothly varying stiffness or stepped stiffness (i.e., the crack is either entirely closed or entirely open). Physical characteristics, common modeling approaches, and response characteristics of both crack models are discussed.

2.3 Gaping Cracks

Gaping crack approximations are common because the models are simple compared to breathing cracks. Gaping cracks remain open regardless of the angular orientation of the shaft; even when the crack is in compression, the faces of the crack do not contact. The gaping crack therefore creates a stiffness asymmetry which is constant in a shaft-fixed rotating frame. According to Papadopoulos [15], the assumption of a gaping crack is valid only when static displacements are small. Another possible scenario in which a crack remains open is when the crack is of finite width, such as a manufactured notch [1]. In his review, Dimarogonas [16] provides a word of caution considering the

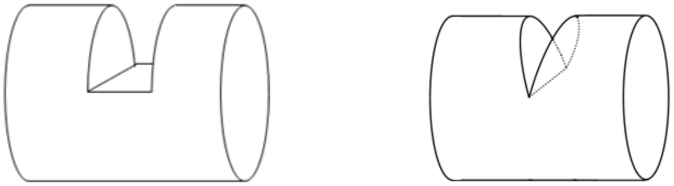

(a) Notch (b) Gaping fatigue crack

Figure 2.2: A comparison of gaping cracks

treatment of notches versus cracks: many authors model cracks but manufacture notches, when thin notches and real cracks behave very differently. Dimarogonas states that in his experience, notches result in a substantially less stiffness reduction than a crack of commensurate depth. Silva and Gomez [17, 18] verify this observation experimentally. These observations are likewise corroborated by the results presented herein. To summarize, it is crucially important to select an appropriate model of the gaping crack's compliance.

2.3.1 Physical Characteristics

There are several categories of physical characteristics for gaping cracks, shown exaggerated in Fig. 2.2. The first category is finite-width notches, which are relatively narrow asymmetric shaft segments. The asymmetric stiffness is generated by differing area moments of inertia [1, 19]. These notches have a finite measurable width, and as such cannot propagate. The other category of gaping cracks is true fatigue cracks, which propagate due to cyclic stresses in the shaft and a very large stress concentration at the crack tip. Such gaping fatigue cracks are of negligible width and terminate in a sharp edge.

Cracked shafts, and especially shafts displaying a gaping crack, behave similarly to asymmetric shafts. The stiffness of both is constant in a rotating reference frame but contingent on the shaft's angular orientation in an inertial frame [1, 19, 20]. The connection between globally asymmetric shafts and gaping cracks is recognized intuitively, as the cross-section of the shaft at the gaping crack is equivalent to the cross-section at any location along a globally asymmetric shaft. Both Green and Casey [1] and Rao [19] discuss the modeling of globally asymmetric shafts by characterizing shaft stiffness using Euler-Bernoulli beam theory. Green and Casey [1] use a globally asymmetric shaft to qualitatively understand the dynamic response of an overhung rotordynamic system displaying a gaping crack. A globally asymmetric shaft is created by replicating the depth of the crack across the entire shaft as a 'worst-case' scenario. However, diagnostic condition monitoring systems must rely on quantitative aspects of the dynamic response, necessitating a crack model whose accuracy extends beyond the simple virtues of an asymmetric shaft model.

2.3.1.1 Notches

One such gaping crack model is the aforementioned notch. The difficulty in manufacturing true fatigue cracks has led many researchers to utilize finite-width notches in both their analytical work [1, 2] and experimental work [1, 17, 21, 22]. This conclusion is corroborated by the literature reviews performed by Sabnavis and Dimarogonas [4, 16], which state that most experimental work focuses on notches because they are simple to fabricate.

Many examples concerning the manufacture of notches can be found in the literature. Green and Casey [1] manufacture a rectangular notch of width 0.3 mm via electrical discharge machining (EDM). Varney and Green [2] discuss such a notch in detail, and provide a comparison to a gaping fatigue crack. Inagaki [21] likewise manufactures a notch for experimental purposes, while Mayes and Davies manufacture a small notch using EDM to facilitate formation of a true fatigue crack under cyclic loading [20]. Silva and Gomez [17] manufacture a notch of width 0.5 mm using a thin cutting tool in a milling machine, whereas Gomez and Silva [18] compare the compliance of the aforementioned notch to that of a true fatigue crack generated via a three-point bending test. Their work concludes that a true fatigue crack results in a greater loss of stiffness than a commensurate notch.

Though not quantitatively accurate compared to a true fatigue crack, the prevalence of notch models demonstrates the concept's value for developing crack detection and diagnosis condition monitoring systems. Understanding a simple model such as the notch serves as a conceptual base for future work on more realistic crack models.

2.3.1.2 Gaping Fatigue Cracks

Fatigue is the primary mechanism driving the initiation and propagation of cracks in real rotordynamic systems. Many authors have developed various techniques for estimating the stiffness of rotordynamic systems displaying gaping fatigue cracks, though a majority of methods employ concepts from fracture mechanics. Dimarogonas and Papeitis [14, 23] pioneer a method for estimating crack compliance using strain energy methods [24]. The technique employs fracture mechanics principles, and specifically the strain energy release rate (SERR), to estimate the local crack compliance. Dimarogonas et al. first employ the concept on non-rotating shafts [23, 25, 26, 27], emphasizing the appearance of coupling effects induced by the crack. Dimarogonas and Papadopoulos [25] expand the SERR-based crack compliances by developing a six degree of freedom crack compliance matrix. These concepts are subsequently extended to rotating shafts [15, 28]. An excellent survey of the SERR approach for modeling cracked rotordynamic shafts is provided by Papadopolous [29], who references many works employing the SERR technique to estimate crack compliance.

Papadopoulos [30] provides a letter to the editor in which the nuances of the crack compliance calculations are explained. A discussion is given concerning the singularity which appears in the calculation when the crack depth is greater than the shaft radius. Darpe et al. [31] give a thorough treatment of the crack compliances for a fully populated six degree of freedom compliance matrix. Such a matrix allows for full coupling between the lateral, axial, and torsional degrees of freedom.

Dimarogonas et al. [14, 15, 23] place the crack at the mid-span of the rotor to obtain an expression for the shaft's global stiffness. Darpe et al. [31] likewise investigate only the scenario in which the crack is centrally located on the shaft. Negating the influence of crack location provides an understanding of the effect of crack depth, but does little to provide useful diagnostic information for real cracks. In fact, as will be seen, very deep cracks can remain undetected, given that the crack is located within certain regions of the shaft.

Penny and Friswell [32] make it clear that though many techniques exist for estimating fatigue crack compliance, the best method remains unsettled. However, several authors have experimentally obtained crack compliances. Papadopolous and Dimarogonas [25] compare several such experimental analyses to the crack compliances obtained from the SERR approach, and find good agreement between the measured and predicted values.

2.3.2 Modeling and Response Characteristics

The hallmark dynamic response signature of a cracked (gaping) or asymmetric shaft is the appearance of a 2X shaft speed harmonic induced by radial forcing in a constant direction, such as gravity [1, 15, 19]. The 2X harmonic appears in the frequency spectra at twice the frequency of shaft rotation. The presence of a frequency component at twice the shaft speed creates a resonance at half of a natural frequency; this resonant shaft speed is referred to as the 2X resonance frequency. The 2X resonance frequency is often referred to as the 2X critical speed or half critical speed.

As discussed later, the 2X harmonic is a widely-used indicator for crack detection systems. Several authors [1, 2, 22] state that as the shaft speed is brought closer to resonance, the magnitude of the 2X harmonic increases, reaching a maximum magnitude at the 2X resonance frequency. As the shaft speed deviates from resonance, the magnitude of the 2X harmonic decreases pronouncedly. The profile of the 2X harmonic during run-up and coast-down can thus provide meaningful detection and diagnosis information.

The transfer matrix method is often used in rotordynamic analysis [1, 2, 33]. The transfer matrix is first developed by Pestel and Leckie [34]. The method gives a matrix representation of the steady-state equations of motion for various system components. Genta [35] demonstrates that the transfer matrix method and the finite element method provide equivalent results, so long as the same discretization is used. Inagaki [33] analyzes a generally asymmetric rotor-bearing system using the transfer matrix technique. The analysis highlights the appearance of the 2X harmonic in the presence of shaft asymmetry. In addition, the analytic results are compared to measured results from a real turbomachinery system and found to be in good agreement. Various transfer matrix techniques are discussed in the literature survey by Papadopoulos [29].

Green and Casey [1] employ the Complex Extended Transfer Matrix method developed by Lee and Green [7] to analyze an overhung rotordynamic system. The system contains a gaping fatigue crack 6.35 mm (0.25 inches) from the support. The objective of the work is to demonstrate the feasibility of using the previously discussed test rig [10] to also detect a gaping shaft crack. The influence of crack location on dynamic response is not investigated. Green and Casey provide transfer matrices for a four degree of freedom overhung rotor system including gyroscopic effects, damping effects, and forcing due to gravity. In addition, the transfer matrices are provided in a rotating reference frame such that the stiffness of the shaft is invariant relative to the frame (Varney and Green [36] further expound upon the use of transfer matrices in a rotating reference frame). The results of the analysis indicate that the 2X harmonic is small when the shaft speed is far from the 2X resonance frequency. In addition, they demonstrate that as crack depth increases the magnitude of the 2X tilt resonance increases while the 2X resonance frequency decreases. The analytic results are verified experimentally, as discussed by Casey [37] and Varney and Green [2].

Though Green and Casey [1] employ a gaping fatigue crack in their analytic modeling, they manufacture a notch for experimental purposes. As such, some discrepancy is found between the predicted and measured 2X resonance frequencies. The predicted 2X resonance frequency decreases more pronouncedly with crack depth than the experimental results indicate. To model the experimental notch more accurately, Varney and Green [2] develop a transfer matrix accounting for asymmetric beam segments. The transfer matrix method utilized by Green and Casey accounted only for the local compliance of the gaping fatigue crack, and did not account for the finite-width nature of the asymmetric beam segment (i.e., the notch). As expected, the predicted 2X resonance frequencies more closely align with those measured experimentally by Casey [37]. The less pronounced decrease in 2X resonance frequency occurs because a notch represents a less severe decrease in stiffness than a commensurate gaping fatigue crack. Dimarogonas [23] confirms this observation by comparing analytic results for the stiffness of a gaping fatigue crack to experimental results for a notched shaft obtained by Grabowski [38].

A majority of authors discussing transverse fatigue cracks and asymmetric shafts solve the full equations of motion. Dimarogonas obtains a system of linear differential equations for a system with a gaping crack at the shaft's mid-span [23]. The degrees of freedom employed are the lateral displacements of the rotor located at the midpoint of the shaft. The equations of motion are solved analytically to expose the 2X harmonic component of the system response. Dimarogonas, Papadopoulos, and Gounaris [23, 25, 26] obtain the equations of motion of various cracked beams (i.e., non-rotating shafts) via finite element formulations. The results are extended to rotating shafts in further works by the same authors [15, 28]. In both works, the equations of motion are solved via steady-state harmonic response techniques, and the crack's influence on the coupling between various rotor degrees of freedom is discussed. Gounaris et al. [28] provide monograms giving the amplitude of the coupled response as a function of crack location and depth. However, the coupled response is obtained from harmonic forcing of the shaft, which is not a natural scenario. Wauer [39] develops a system of six degree of freedom equations of motion for a cracked Timoshenko shaft, and solves the equations analytically using variational principles. Wauer then provides the first fundamental frequency decrease as a function of crack depth for several crack locations.

Note that in all of the aforementioned works addressing equations of motion, only those employing discrete formulations, such as finite element methods or the transfer matrix, incorporate the effects of crack location. Furthermore, out of the references employing finite element techniques, only a single reference [28] provides quantitative results for the influence of crack location on the dynamic response.

2.4 Breathing Cracks

The incorporation of breathing behavior into a dynamic model of a cracked rotordynamic system represents a significant increase in complexity over similar gaping crack models. The nature of the breathing crack can introduce nonlinearities, which complicate efforts to solve and interpret the system's dynamic response. However, breathing behavior often provides a more realistic transverse fatigue crack model [4], as static displacements typically dominate vibration amplitudes.

2.4.1 Physical Characteristics

Breathing cracks differ from gaping cracks in that the stiffness of the cracked shaft is time dependent even in a rotating reference frame. As the shaft rotates, forcing in a constant inertial direction (such as gravity) keeps a portion of the shaft cross-section in compression and a portion in tension. The section of the crack face under tensile stress opens, while the section of the crack face under compression closes. Therefore, for cracks smaller than the radius of the shaft, there is an angular position at which the crack is completely closed (the shaft behaves as if there is no crack) and an angular position at which the crack is completely open. Most breathing crack models rely on the assumption that vibration amplitudes are negligible compared to static displacements [38, 40]. The small vibration amplitude assumption allows the shaft stiffness to be calculated as a function of only the shaft's angular position.

The complicated nature of breathing behavior in cracks results in a slew of approximations. These approximations are categorized in order of increasing complexity as step models, sinusoidally-varying models, and vibration-dependent models. The simplest breathing crack models are step models (also known as hinge or switching models), which approximate the crack as either entirely opened or closed at any state in time. Gasch [40, 41] discusses such a hinge model, in which the shaft's stiffness is bi-linear. Dimarogonas [23] uses a similar step function to approximate the switching behavior of a breathing crack. Szolc [42] employs a switching crack model, though the switching behavior is dependent on the shaft's curvature at the crack's location rather than the angle of rotation.

Mayes and Davies [20] pioneered the use of smoothly varying breathing models to describe shaft stiffness as a function of shaft angular position through the use of the following steering function:

$$f(\theta) = \frac{1 + \cos\theta}{2}, \tag{2.1}$$

where θ is the angle of shaft rotation. Modulating the stiffness of the shaft by Eq. 2.1 provides a method for incorporating breathing behavior. Such a method better approximates the breathing of the crack by allowing a smooth transition between the opened and closed states of the crack. Several other authors [43, 44, 45] also use such a steering function. Grabowski [38] also employs a method for determining the stiffness of the cracked shaft as a function of angular position, and graphically provides the shaft stiffness as a function of shaft rotation.

The most complicated breathing models are those in which the open-closed state of the crack is vibration-dependent. Darpe et al. [31] provide a robust method for capturing the breathing behavior of a cracked rotating shaft using the Crack Closure Line (CCL). The CCL is the position along the crack edge where the crack faces switch from being opened to being closed. In the fully open state, the compliance of the crack is calculated by the method of Papadopolous and Dimarogonas [15]. To determine the position of the CCL, a total stress intensity factor (SIF) is found at each location along the crack edge; the SIF depends on the nodal forces at the crack, and thus, is vibration-dependent. Furthermore, the sign of this SIF dictates whether the stress at that location is tensile or compressive. The position where the SIF changes from positive to negative signifies where the crack faces have switched from being opened to being closed. The crack's compliance is then calculated by adjusting the integration bounds found in [15]. Various other works incorporate this concept of the CCL [46, 47, 48, 49].

Though only several examples of breathing crack models are provided here, Papadopoulos [29], Dimarogonas [16], and Sabnavis [4] provide many references to various breathing crack models in their excellent literature reviews.

2.4.2 Mathematical Modeling and Response Characteristics

While gaping cracks produce only a 2X shaft speed harmonic, breathing cracks produce pX shaft speed harmonics, where p is any positive real integer [20, 23, 38, 40, 41]. The primary shaft speed harmonics induced by breathing behavior occur at the 1X, 2X, and 3X, though shaft speed harmonics exist at integer multiples above 3 [44]. In fact, Sabnavis [4] suggests in his literature review that changes in the 1X harmonic can serve as a more reliable crack indicator than the 2X harmonic.

The typical method for obtaining the response of a shaft displaying a breathing crack is numerical solution of the (often non-linear) equations of motion. Gasch [41] numerically integrates gravity-forced two degree-of-freedom equations of motion for a crack whose stiffness is bi-linearly dependent on the crack orientation (e.g., the hinge crack model). The inertial frame degrees of freedom are the rotor's transverse displacements. The results clearly indicate multiple resonance peaks, where the dominant peaks are induced by the 1X and 2X harmonics. The results are subsequently extended [40] to provide the direction (backward or forward) of the primary shaft speed harmonics. Mayes [20] analytically solves the nonlinear cracked shaft equations-of-motion to give a simple expression relating the change in natural frequencies to crack location. Several measurement positions on a real rotor system are used to estimate the crack depth and location, with mediocre results. Mayes discusses the appearance of primarily 1X and 2X harmonics in the response.

Grabowski [38] demonstrates the appearance of 1X, 2X, and 3X harmonics, though he shows the 3X harmonic is significantly smaller than both the 1X and 2X components. The influence of crack location on system response is not provided quantitatively, though it is stated that the crack induced vibration is influenced strongly by crack position relative to the excited mode of the shaft.

In the past decade, many works have addressed nonlinear aspects of the response of breathing crack models. Sawicki et al. [45] develops a three degree of freedom modified Jeffcott model of a cracked rotordynamic system, including a torsional degree of freedom. Breathing is accounted for using a smooth steering function, and three forms of excitation are applied: gravity, imbalance, and harmonic torsional excitation. The equations of motion are solved numerically, and the lateral and torsional response is provided in the form of bifurcation diagrams, power spectra, and rotor orbits. Coupling induces the appearance of torsional excitation frequencies in the lateral vibration spectrum. In addition, chaotic behavior is observed; the authors suggest that these response characteristics could be employed to diagnose the crack parameters, though crack location is not discussed in their results.

Wu [43] expands upon the work by Sawicki et al. [45] by modeling a two-mass turbine-generator system; the presence of the additional mass necessitates the inclusion of an additional torsional degree of freedom. The equations are integrated numerically, and various shaft speed harmonic peaks are observed when the torsional and lateral natural frequencies are an integer fractional ratio (such as the 1X, 2X, and 3X harmonics). For different ratios of the torsional to lateral natural frequencies, the critical speeds are no longer integer fractional multiples of the torsional natural frequency. Only a single crack location is discussed, and no conclusions are drawn concerning crack detection and diagnosis.

Darpe et al. [31] employ a finite element formulation of a breathing crack system. The stiffness is approximated using the aforementioned Crack Closure Line, and the subsequent nonlinear equations of motion are integrated numerically. The shaft's stiffness is reevaluated at every degree of rotation.

Szolc [42] employs a unique hybrid model of a cracked rotordynamic system. A real turbo-generator is modeled using 49 elements and seven fluid film bearings, where the elements are continuous shaft models coupled through boundary conditions. The crack is incorporated through a modification of the boundary conditions joining the beam segments to the left and right of the crack. The boundary conditions are modified such that an additional compliance, found using Dimarogonas' method [23], acts as a spring between two elements. Various shaft speed harmonics are shown to appear in the results. Many crack depths and locations are investigated, as will be discussed shortly.

2.5 Crack Detection and Diagnosis

Many works presenting shaft crack diagnosis routines share several common aspects. Though the stated objective of many works is application to rotating shafts, stationary shafts are investigated [21, 50]. Complicated algorithms, in conjunction with many measurement points along the shaft, are often used to provide only a marginally successful estimation of the crack depth and location [28, 51].

For rotordynamic systems, it is desirable to develop an on-line crack diagnosis routine. Furthermore, in rotordynamic systems, very few measurement locations are available due to the nature of the system. Szolc [42] addresses this concern by only using realistic measurement locations as the basis for his diagnostic routine (such as lateral displacements at the bearings). Several diagnosis routines for stationary and rotating shafts use mode shape analysis [20, 25, 50] or other similar techniques requiring an array of measurement locations along the shaft [51]. Experimental mode shape analysis is restricted by the number of measurement points available on the shaft. A large number of measurement points is not only economically impractical, but also infeasible for rotating systems. Many routines, including those employing active magnetic bearings or coupled response measurements, use harmonic forced excitations [25, 28, 50, 52] to diagnose the crack parameters. Such procedures employing application of harmonic forcing are often expensive, procedurally difficult, and impractical [28, 32, 53].

The primary techniques for crack detection and diagnosis in rotordynamic systems are, in order of decreasing prevalence, vibration monitoring, experimental modal analysis, and alternative techniques such as wavelet analysis. Vibration monitoring observes the forced response, and specifically, phenomena such as shaft speed harmonics or coupling. Transducers such as accelerometers or proximity probes measure the forced dynamic response of the system, which is typically induced by imbalance or gravity.

The difficulties of accurate crack detection and diagnosis using vibration monitoring are well understood, especially for shallow cracks. Penny and Friswell [32] explain that though a cracked shaft changes the dynamic response of the system, detecting these changes for small or even medium depth cracks is exceptionally difficult. Casey and Green [1] expound upon this issue by highlighting that the magnitude of the 2X harmonic introduced by the crack is very small away from the 2X resonance frequency. If the machinery is not operating near the 2X resonance frequency, which it likely is not, a true on-line condition monitoring system stands little chance of detecting the crack if based only upon the presence of the 2X harmonic.

Many authors employ the presence of a 2X harmonic to detect a transverse shaft crack. Bently et al. [54] reveal that their field experience with the early detection of shaft cracks indicates that more than 70% of early warnings occur because of changes in the 1X harmonic, whereas the remaining 30% occur with the 2X harmonic. Changes in the 1X harmonic serve as an early warning signal because most cracked shafts experience bow due to the crack, which generates a prominent 1X harmonic.

Several papers explore crack detection and diagnosis via coupled response measurements [15, 25, 27, 28]. The presence of a crack introduces coupling between the degrees of freedom; this coupling can indicate a crack. Gounaris [28] measures lateral displacements induced by axial excitation to diagnose crack parameters in a rotordynamic system. Though the method provides a rigorous procedure to separate crack depth and location, the need for axial excitation at a range of frequencies and shaft speeds is often impractical. Several other authors [31, 43, 45, 46, 48, 49] suggest the use of coupling to detect shaft cracks, though none suggest corresponding diagnostic routines.

Experimental modal analysis extracts a system dynamic model by de-convolving the measured response from the known forcing. Bucher [53] provides an excellent review of experimental modal analysis for rotating structures. The limited number of excitation and measurement points complicates experimental modal analysis in rotating systems. Application of harmonic forcing to rotordynamic systems is difficult, though some have seen limited success through the use of active magnetic bearings

[52]. Though promising, active magnetic bearings suffer from a number of practical shortcomings. Penny and Friswell [32] mention several shortcomings, namely, the inability of the bearing to provide a true step excitation and the limited maximum rate of change of the bearing force.

Many authors provide experimental crack detection and diagnosis procedures, using both experimental test rigs and real turbomachinery systems. Mayes and Davies [20] employ changes in pairs of natural frequencies of a stationary shaft (non-rotating), and also changes in the shaft deflection modes, to estimate crack location and depth in a large generator rotor. Though the predicted parameters are relatively close to the actual values, extensive ultrasonic measurement is still required to pinpoint the exact location and depth of the crack. Green and Casey [1] and Varney and Green [2] discuss the feasibility of using an existing overhung rotordynamic test rig to detect both transverse shaft cracks and mechanical face seal contact, though only the influence of crack depth is discussed. Imam et al. [55] discuss the application of a transverse crack detection regime to a real rotordynamic system. It is stated that the method can detect cracks as shallow as one to two percent of the shaft diameter. Other experimental techniques are discussed in the literature reviews provided by [4, 16, 29].

Various alternative techniques have emerged in the past several years for crack detection, such as wavelet analysis and stochastic methods. Wavelet analysis essentially recovers transient information lost during frequency domain analysis. Sabnavis [4] discusses wavelet analysis, as well as other atypical techniques, in his literature review of crack detection in rotordynamic systems. Darpe [47] also discusses the use of wavelets pertaining to cracked rotordynamic systems, as do Sinou [22] and Nagaraju [56]. Szolc [42] implements a stochastic method relying on comparison between measured results and a large data base of response profiles generated from many combinations of crack location and depth. An initial estimate is made, and the database is then refined in the neighborhood of the initial estimate. Szolc reports that only very large databases produce usable results, and even then, the best accuracy obtained is approximately 5 - 10% of the shaft length for crack location and 10 - 15% of the shaft diameter for crack depth. The error in crack depth is significant, as cracks above 40% of the shaft diameter are often easily detected.

2.6 The Complex Transfer Matrix

A subsidiary contribution of this work is the development of the Complex Transfer Matrix (CTM). Previous works employing transfer matrix methods, such as those by Varney and Green [2], Green and Casey [1], and Lee and Green [7], rely on a transfer matrix with real-valued coordinates. Though physically insightful, and often required for analysis of non-isotropic systems, the real-valued transfer matrix results in an 8×8 formulation which is computationally inefficient, sometimes prone to inaccuracy, and, most importantly, fails to distinguish between forward and backward whirl frequencies. This method is deemed the Real Transfer Matrix, due to the size of the matrices and the ability to account for deflections in orthogonal planes. A complex-valued redefinition of the state variable elements is introduced to reduce the size of the transfer matrix to 4×4. The mathematical nature of the redefined transfer matrix gives a reduced order characteristic equation which intrinsically separates backward and forward whirl. The Complex Transfer Matrix is provided herein for both inertial and rotating reference frames, with discussion highlighting key differences between analysis in each frame.

Determination of whirl frequencies is an integral component of rotordynamic analysis. Whirl frequency computation is a free (or natural) response analysis, and requires solution of the corresponding eigenvalue problem. The importance of the free response analysis has led to the development of many analysis techniques, both analytical and numerical. Prior to providing a detailed review of these techniques, several aspects of shaft whirl must be discussed.

Whirl is characterized by its direction relative to the shaft rotation. Whirl in the direction of shaft rotation is deemed forward whirl, while whirl in the direction opposite shaft rotation is labeled backward whirl [35]. Furthermore, synchronous whirl occurs when the whirl frequency and shaft rotation frequency coincide [19]. As many prevalent rotordynamic excitations occur at the shaft speed, such as imbalance, operation of the system at a shaft speed equal to the synchronous whirl frequency can produce a resonant-like response. Thus, shaft speeds at which the forcing frequency coincides with the whirl frequency are deemed critical speeds.

Since specific faults excite either forward or backward whirl, or a combination thereof, determining the whirl direction is important. It is well known that excitation due to rotating imbalance excites forward whirl. On the other hand, rotor-stator rub excites backward whirl [49]. According to Ding [57], this rotor/stator contact under certain conditions induces synchronous backward whirl known as dry whip, which can quickly lead to catastrophic failure. Moreover, Jiang [58] provides evidence that backward whirl exists in a non-synchronous state well before the onset of dry whip. Likewise, transverse shaft cracks [4, 59] have been shown to excite both forward and backward whirl (this conclusion is also validated in this work). Determining whirl frequencies and their directions is important for the safe operation of rotordynamic machinery, and also important in the diagnosis of various common faults.

2.7 Conclusions

A great amount of research has been performed investigating the dynamics of cracked rotating structures. Beyond merely modeling these structures, many experimental works involving both experimental test rigs and real turbomachinery systems are discussed. Despite this wealth of knowledge, standard procedures for on-line crack diagnosis in rotordynamic systems is lacking. The reason for this is the difficulty of diagnosing both crack location and depth while the machinery is in operation. This difficulty is seen in the literature, as discussion of the influence of crack location on system response is tenuous at best. Many techniques have arisen to address the problem, such as vibration monitoring, experimental modal analysis, and alternative techniques such as wavelet analysis or stochastic methods. In the authors opinion, vibration monitoring is a preferred technique due to the simplicity of the measurements and the avoidance of the issue of limited excitation and measurement locations on a real rotordynamic system.

This work aims to discuss the feasibility of using simple vibration monitoring techniques, such as observation of the 2X harmonic response component, to detect transverse fatigue cracks in rotordynamic systems and to provide methods to diagnose their parameters. For simplicity, a gaping crack is employed in the analytic modeling. The profile of the 2X harmonic, particularly near resonance, is discussed as a simple signal with applicability for transverse shaft crack diagnosis.

Many previous works on crack detection and diagnosis have ignored or vastly simplified the influence of crack location; this work aims to robustly incorporate the effects of crack location and depth. In addition, most works proposing crack diagnostic procedures suggest complicated, expensive, and impractical procedures for diagnosing the crack parameters of interest. This work hypothesizes that simple vibration monitoring techniques can be successfully applied to diagnose multiple crack parameters.

CHAPTER III

THEORETICAL DEVELOPMENT: MODELING THE CRACK

The ability to detect and diagnose cracks soon after initiation is imperative to avoid catastrophic shaft failure and plan accordingly for repairs. A condition monitoring system's ability to diagnose crack parameters strongly depends on the accuracy of the crack model. Transverse shaft crack models should account for the crack's depth and location, as both parameters significantly influence the dynamic response of the system via a reduction of the stiffness. As discussed in Chapter 2, the influence of crack location on the system response is often neglected in lieu of discussion on crack depth, especially concerning crack diagnosis. Understanding the dynamic interplay between crack location and depth is crucial for diagnosis.

Before the specific crack models can be discussed, it is necessary to provide a consistent model of the undamaged overhung rotordynamic system. Adherence to a consistent dynamic framework allows the differences between the crack models to be isolated, investigated, and interpreted. Relevant degrees of freedom are presented prior to derivation of the equations of motion of the undamaged overhung rotordynamic system.

Two gaping crack models are proposed following formulation of the rotordynamic model of the undamaged system. The local stiffness of each crack is discussed, and the stiffness matrix of the cracked overhung rotordynamic system is provided. The first crack model represents a finite-width gaping crack typically manufactured for experimental purposes, and is designated the notch model. The second model, the gaping fatigue crack, assumes a true fatigue crack of negligible width. The crack

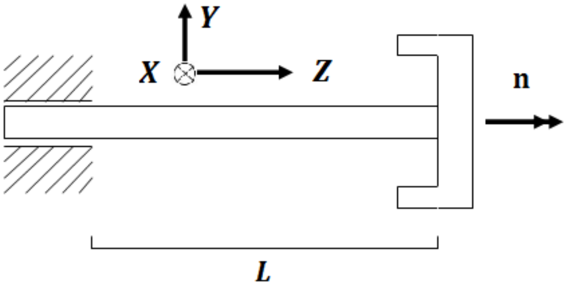

Figure 3.1: Undamaged overhung rotordynamic system

compliance is obtained using fracture mechanics and energy principles. A gaping fatigue crack is more likely to be encountered in the operation of real turbomachinery systems.

In addition, an available overhung rotordynamic test rig is summarized. The overhung test rig is pertinent to this work, as the models employed herein emulate the test rig. Physical parameters of the test rig are provided, as well as a discussion on damping.

3.1 Undamaged Rotordynamic System Model

An undamaged overhung rotordynamic system is shown in Fig. 3.1; this rotordynamic model emulates the experimental test rig discussed in Chapter 2, Section 2.1. Beyond being a simple and realistic model of many real rotordynamic systems, the test rig model is used in this work for several reasons. First, direct comparison is allowed between this work's results and previous analytic [1, 2] and experimental results [2, 37]. Second, the availability of the test rig allows for comparison to future experimental results.

The single rotor (lumped mass) shown in Fig. 3.1 is modeled as having finite mass and rotational inertia. The shaft's mass is assumed to be negligible in comparison to the rotor's mass m. The XYZ reference frame is fixed to a hypothetical undeflected rotating shaft (see Appendix A for details). The relationship between the rotating

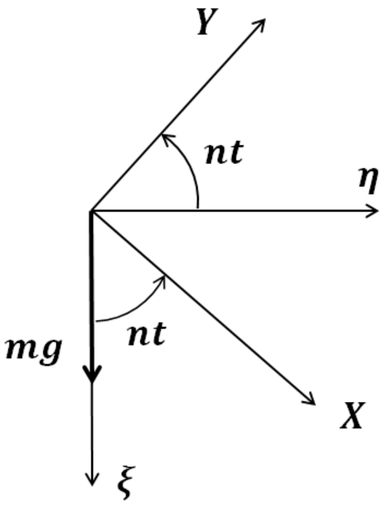

Figure 3.2: Relation between inertial and rotating reference frames, with gravity shown

frame XYZ and the inertial frame $\xi\eta\zeta$ is shown in Fig. 3.2. The use of a rotating reference frame is advantageous, as the gaping crack's stiffness is constant relative to the rotating XYZ frame. The frequency of shaft rotation n is assumed constant, and the length of the shaft is L.

Whirl is a bulk precession of the shaft axis about its undeflected position. As the shaft whirls, the rotor deflects. Two degrees of freedom, u_X and u_Y, capture the deflection of the rotor's center of mass, while two orthogonal tilts, γ_X and γ_Y, provide the total angular motion of the rotor. Axial deflection along Z is neglected, as well as torsional deformation of the shaft.

The rotor plane is shown in Fig. 3.3 to illustrate the degrees of freedom. The $x'y'$ axes, while not the axes used in the analysis, are shown for clarity in presenting the angular degrees of freedom. In the absence of imbalance, the rotor center of mass and geometric center coincide at point C. The undeflected shaft center is located at point O, which is the undeflected position of point C. The reference frame is affixed at O, and rotates at the shaft speed n.

The rotating-frame degrees of freedom u_X, u_Y, γ_X and γ_Y are used to formulate

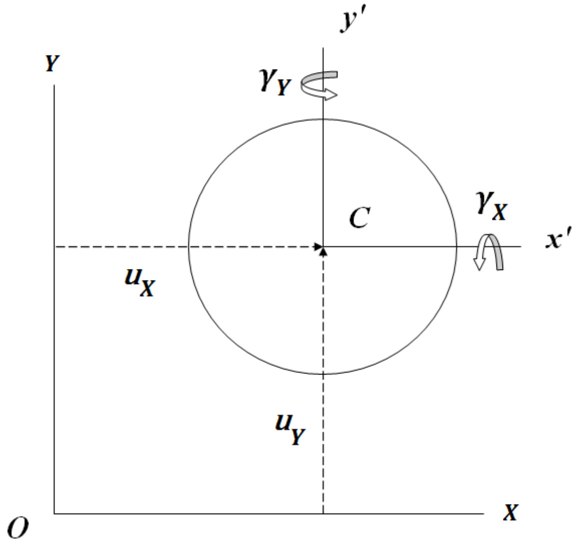

Figure 3.3: Rotor degrees of freedom

the equations of motion. The vector $\{q\}$ is composed of the rotor degrees of freedom:

$$\{q\} = \{\ u_X \quad u_Y \quad \gamma_X \quad \gamma_Y\ \}^T. \tag{3.1}$$

The general linear equations of motion, as provided shortly, are

$$[M]\{\ddot{q}\} + ([D] + [G])\{\dot{q}\} + \left([C]^{-1} - [E]\right)\{q\} = \{F\}, \tag{3.2}$$

where $[M]$ is the mass matrix, $[D]$ is the damping matrix, $[G]$ is a matrix containing gyroscopic and Coriolis terms, $[C]$ is the compliance matrix, and $[E]$ is a matrix containing centripetal terms arising from rotating frame analysis. A general set of external forces $\{F\}$ is applied to the system.

The mass matrix $[M]$, gyroscopic matrix $[G]$, and centripetal matrix $[E]$ are found using Newton-Euler mechanics. To accomplish this, Appendix A provides the acceleration of the rotor's center of mass and the angular momentum. The compliance matrix $[C]$ is found later for an undamaged system, a notched system, and a system displaying a gaping fatigue crack (the damping matrix $[D]$ is proportional to the inverse of the compliance matrix). The four degree-of-freedom linear coupled equations of motion become

$$\begin{bmatrix} m & 0 & 0 & 0 \\ 0 & m & 0 & 0 \\ 0 & 0 & I_t & 0 \\ 0 & 0 & 0 & I_t \end{bmatrix} \begin{Bmatrix} \ddot{u}_X \\ \ddot{u}_Y \\ \ddot{\gamma}_X \\ \ddot{\gamma}_Y \end{Bmatrix}$$
$$+ \left(\begin{bmatrix} 0 & -2mn & 0 & 0 \\ 2mn & 0 & 0 & 0 \\ 0 & 0 & 0 & n(I_p - 2I_t) \\ 0 & 0 & -n(I_p - 2I_t) & 0 \end{bmatrix} + [D] \right) \begin{Bmatrix} \dot{u}_X \\ \dot{u}_Y \\ \dot{\gamma}_X \\ \dot{\gamma}_Y \end{Bmatrix} \tag{3.3}$$
$$+ \left([C]^{-1} - \begin{bmatrix} mn^2 & 0 & 0 & 0 \\ 0 & mn^2 & 0 & 0 \\ 0 & 0 & -n^2(I_p - I_t) & 0 \\ 0 & 0 & 0 & -n^2(I_p - I_t) \end{bmatrix} \right) \begin{Bmatrix} u_X \\ u_Y \\ \gamma_X \\ \gamma_Y \end{Bmatrix} = \{F\}$$

for a general damping matrix $[D]$ and compliance matrix $[C]$. It is convenient to obtain the compliance matrix prior to the stiffness matrix. The stiffness matrix $[K]$ and compliance matrix $[C]$ are related by

$$[K] = [C]^{-1}. \tag{3.4}$$

The stiffness matrix of the undamaged overhung shaft is obtained from Euler-Bernoulli beam theory, as discussed by Shigley [60]:

$$[K] = \begin{bmatrix} \frac{12EI}{L^3} & 0 & 0 & -\frac{6EI}{L^2} \\ 0 & \frac{12EI}{L^3} & \frac{6EI}{L^2} & 0 \\ 0 & \frac{6EI}{L^2} & \frac{4EI}{L} & 0 \\ -\frac{6EI}{L^2} & 0 & 0 & \frac{4EI}{L} \end{bmatrix}, \tag{3.5}$$

where the elastic modulus of the shaft is E, the length of the shaft is L, and the area moment of inertia of the symmetric shaft is I. It is assumed that the crack does not introduce additional damping into the system. As discussed in Section 3.4.1, and originally implemented in [1], the damping is assumed to be proportional to the undamaged shaft's stiffness by the coefficient β:

$$[D] = \frac{1}{2n}\beta[K]_{Undamaged}, \tag{3.6}$$

where n is the shaft speed of the system. Keep in mind that $[M]$, $[G]$, $[E]$,and $[D]$ are unaffected by the presence of a crack.

The dynamic model of the undamaged system establishes a framework on which to formulate the cracked system model. To establish these models, the compliance matrices of the cracked systems are obtained. Two crack models are discussed: a notch and a gaping fatigue crack.

3.2 The Notch Model

3.2.1 Overview

The similarity between manufactured notches and true fatigue cracks allows a notch model to be used as a development tool to establish crack detection and diagnosis principles. Guidelines can be established using a notch model prior to the complicated manufacture and characterization of a true fatigue crack. Finite-width notches are manufactured for many experimental crack detection and diagnosis investigations [2, 20, 21, 38]. A commonly employed technique for notch manufacture is electric discharge machining (EDM). The finite diameter of the EDM wire generates a rectangular-profiled notch, where the interior corners possess a radius commensurate to the wire diameter. Herein, the corner radius is neglected in comparison to the crack's width and the depth.

A notched rotordynamic system is shown in Fig. 3.4, where the notch's width is L_C. The length of the shaft from the support to the left end of the notch is L_1, while the length of the shaft from the right end of the notch to the free end is L_2. The axes in Fig. 3.4 are commensurate with those in Fig. 3.1. Figure 3.6 provides a

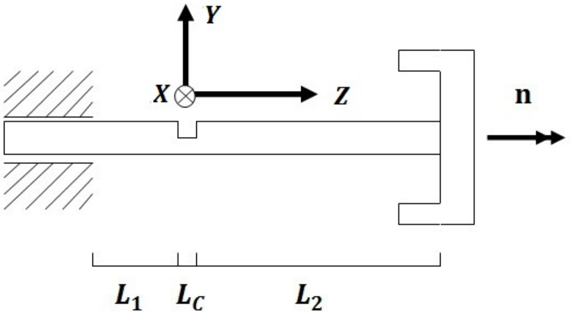

Figure 3.4: Overhung rotordynamic system displaying notch of width L_C

cross-sectional view of the notch. Appendix B provides the area moments of inertia of the rectangular notch.

3.2.2 Notch Stiffness

The stiffness matrix of the notched shaft is central to the dynamics of the system. Castigliano's Theorem is used in conjunction with Euler-Bernoulli beam theory to generate the compliance matrix, from which the stiffness matrix is obtained. Castigliano's Theorem employs strain energy expressions to determine the deflection caused by application of a load [60, 61]. The application of load P (where P is either a force or moment) induces an internal bending moment M; in the following, subscripts on these terms indicate the axis about which they act. In this case, the subscripts i and j can represent axes X or Y, as shown in Fig. 3.4. In general, for a beam of constant elastic modulus E, the linear deflection u_i (that is, the linear deflection parallel to axis i) caused by an internal bending moment generated by a force P_i (the force is entirely in the direction of axis i) is

$$u_i = \int_0^L \frac{M_j}{EI_j} \left(\frac{\partial M_j}{\partial P_i} \right) dz. \tag{3.7}$$

Note that the internal bending moment generated by a linear force occurs about an axis perpendicular to that force. Hence, though force P is applied in the direction i, the internal bending moment is generated about axis j. Similarly, the angular deflection γ_i generated by a moment P_i (note that both the moment and angular deflection occur about the same axis, i) is

$$\gamma_i = \int_0^L \frac{M_i}{EI_i} \left(\frac{\partial M_i}{\partial P_i} \right) dz, \tag{3.8}$$

where it is important to recognize that external bending moment P_i generates an internal bending moment about the same axis i. To account for the notch cross section, the integrations in Eqs. 3.7 and 3.8 are evaluated piece-wise. In this case, the external loads are applied at the rotor; hence, the deflections given in Eqs. 3.7 and 3.8 provide the deflections of the rotor.

An additional complexity to Castigliano's Theorem exists. Equations 3.7 and 3.8 can only be used when the deflection is in the same direction as the applied load, and of the same nature (i.e., linear deflections and forces, angular deflections and moments). To obtain the linear deflection caused by an applied moment, or the angular deflection induced by an applied force, a virtual load must be introduced. This concept is discussed in detail by Shigley [60] and Hibbeler [61]. Appendix C provides calculations of the compliance matrix terms. The appendix also explains the use of virtual loads to obtain deflections in a direction contrary to that of the applied load. The compliance matrix $[C]$ is found to be:

$$\begin{Bmatrix} u_X \\ u_Y \\ \gamma_X \\ \gamma_Y \end{Bmatrix} = \begin{bmatrix} C_{11_Y} & 0 & 0 & C_{12_Y} \\ 0 & C_{11_X} & -C_{12_X} & 0 \\ 0 & -C_{21_X} & C_{22_X} & 0 \\ C_{21_Y} & 0 & 0 & C_{22_Y} \end{bmatrix} \begin{Bmatrix} F_X \\ F_Y \\ M_X \\ M_Y \end{Bmatrix}, \tag{3.9}$$

where, with subscript j indicating either axis X or Y,

$$C_{11_j} = \frac{1}{3E} \left(\frac{L_2^3}{I_j} + \frac{(L_2 + L_C)^3 - L_2^3}{I_j^C} + \frac{(L_2 + L_C + L_1)^3 - (L_2 + L_C)^3}{I_j} \right) \tag{3.10}$$

$$C_{12_j} = C_{21_j} = \frac{1}{2E} \left(\frac{L_2^2}{I_j} + \frac{(L_2 + L_C)^2 - L_2^2}{I_j^C} + \frac{(L_2 + L_C + L_1)^2 - (L_2 + L_C)^2}{I_j} \right) \tag{3.11}$$

$$C_{22_j} = \frac{1}{E}\left(\frac{L_2}{I_j} + \frac{L_C}{I_j^C} + \frac{L_1}{I_j}\right). \tag{3.12}$$

As expected, the compliance matrix of the notch reduces to that of the undamaged system when the area moments of inertia are equivalent or the width of the notch is set to zero.

3.3 Gaping Fatigue Cracks

3.3.1 Overview

A gaping fatigue crack differs from a notch in that the crack's width is assumed to be negligible. As the name suggests, the mechanism driving the formation of gaping fatigue cracks is fatigue. Fatigue cracks terminate in a sharp edge and are capable of propagation.

Gaping fatigue crack models are often analytically employed but rarely experimentally tested, for two primary reasons. First, gaping fatigue cracks are difficult to manufacture. A stress concentration must be introduced on the shaft at the desired location of the crack. Then, the shaft must be subjected to prolonged cyclic bending fatigue to initiate and propagate the crack. Second, even if a crack forms at the desired location, the crack characteristics (depth, width, profile, etc.) are difficult to control and quantify.

An overhung shaft displaying a gaping fatigue crack is shown in Fig. 3.5. The length of the shaft from the support to the crack is L_1, while the length of the shaft from the crack to the free end is L_2. The rotating XYZ frame shown in the figure is the same as that shown in Figs. 3.1 and 3.3.

The crack cross section is shown in Fig. 3.6. The XY frame shown always maintains its orientation relative to the crack edge. The un-cracked section of the shaft of radius R is designated by hatching. The half-width of the crack is b, and the depth of the crack is a. The crack edge is defined as the edge of the crack which propagates into the shaft.

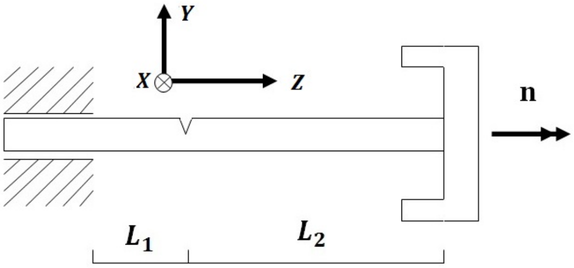

Figure 3.5: Overhung rotordynamic system displaying a gaping fatigue crack

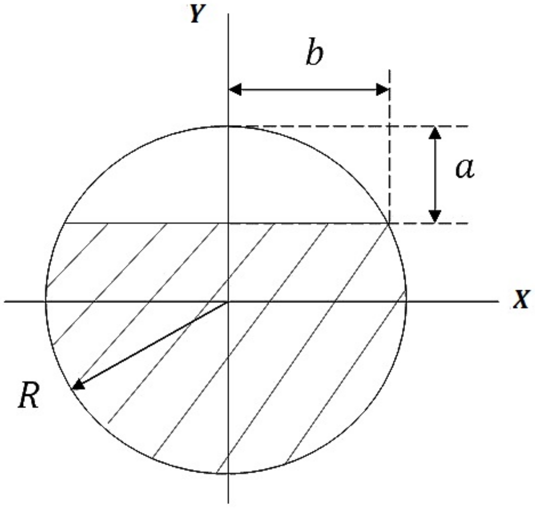

Figure 3.6: Cross-section of a gaping fatigue crack

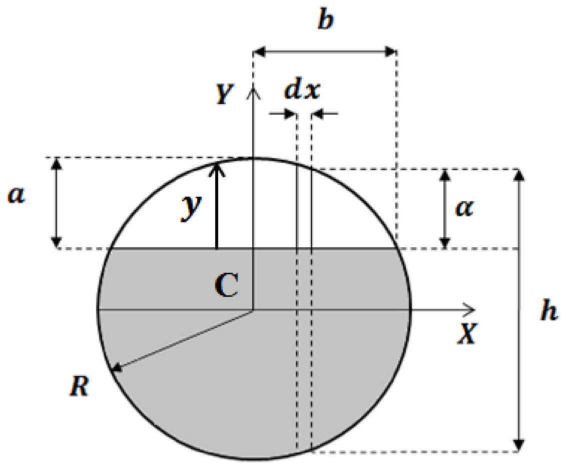

Figure 3.7: Crack cross-section showing terms for compliance calculations

3.3.2 Gaping Fatigue Crack Stiffness

The compliance of a cracked shaft is a function of the uncracked shaft compliance and the additional compliance induced by the crack [40]. The first step in determining the cracked shaft's compliance is to obtain the additional compliance introduced by the crack. Dimarogonas et al. [14, 15, 23] are instrumental in developing a fracture mechanics technique for estimating crack compliance. The technique employs the strain energy release rate (SERR), along with linear elastic fracture mechanics theory, to estimate the crack compliance.

The method was first proposed by Irwin [24] and subsequently extended to rotordynamic systems of six degrees of freedom [15]. The compliance ϵ_i induced by a transverse crack of depth a in the direction of load P_i is

$$\epsilon_i = \frac{\partial}{\partial P_i} \int_0^a J(y)dy, \tag{3.13}$$

where $J(y)$ is the strain energy release rate and y denotes a coordinate variable in the direction parallel to the crack depth, as shown in Fig. 3.6.

The SERR depends on several factors: the elastic modulus E and Poisson ratio v of the shaft, the stress intensity functions corresponding to the geometry of the cracked section, and the applied loads. Papadopoulos and Dimarogonas [14] give the stress intensity functions for a circular cross-section shaft. A general expression for the SERR is provided by Dimarogonas [23]:

$$J(y) = \frac{1-\nu^2}{E}\left[\left(\sum_{i=1}^{6} K_{Ii}\right)^2 + \left(\sum_{i=1}^{6} K_{IIi}\right)^2 + \left(\sum_{i=1}^{6} K_{IIIi}\right)^2\right], \tag{3.14}$$

where the K_{ni} terms denote the stress intensity factors. The stress intensity factors define the stress amplitude at the crack tip singularity [62]. The subscript i denotes the applied load, while the subscripts I, II, and III denote the respective modes of crack formation. In general, for mode n, the stress intensity factor is given by

$$K_{ni} = \sigma_i\sqrt{\pi\alpha}F_n\left(\frac{\alpha}{h}\right) \qquad n = I,\, II,\, or\, III, \tag{3.15}$$

where F_n is a general intensity function dependent on the mode of crack formation; σ_i represents the stress at the crack. The quantities α and h are shown in Fig. 3.7. Solutions for the intensity functions are only available for rectangular strips. The compliance introduced by a rectangular strip dx is

$$c_{ij}^{dx} = \frac{\partial^2}{\partial P_i \partial P_j}\int\limits_0^a J(y)dy. \tag{3.16}$$

To obtain the compliance in the i^{th} direction due to a force in the j^{th} direction, Eq. 3.16 must be integrated along the crack width:

$$c_{ij} = \frac{\partial^2}{\partial P_i \partial P_j}\int\limits_{-b}^{b}\int\limits_0^a J(y)dydx. \tag{3.17}$$

These terms are evaluated by Papadopoulos et al. [15] for various types of displacements and couplings. The crack compliances can be arranged into a local compliance matrix form, as shown by Dimarogonas [14]. Neglecting torsion and axial extensions reduces the size of the local crack compliance matrix from 6 × 6 to 4 × 4:

$$\left\{\begin{array}{c} u_X \\ u_Y \\ \gamma_Y \\ \gamma_X \end{array}\right\} = \left[\begin{array}{cccc} c_{22} & 0 & 0 & 0 \\ 0 & c_{33} & 0 & 0 \\ 0 & 0 & c_{44} & c_{45} \\ 0 & 0 & c_{54} & c_{55} \end{array}\right]\left\{\begin{array}{c} V_X \\ V_Y \\ M_Y \\ M_X \end{array}\right\}. \tag{3.18}$$

Papadopoulos [15] provides the following crack compliances:

$$c_{22} = \frac{2\left(1-\nu^2\right)}{\pi E R}\int_{-b}^{b}\int_{0}^{a} y F_{III}^2\left(\frac{y}{h}\right) dydx \tag{3.19}$$

$$c_{33} = \frac{2\left(1-\nu^2\right)}{\pi E R}\int_{-b}^{b}\int_{0}^{a} y F_{II}^2\left(\frac{y}{h}\right) dydx \tag{3.20}$$

$$c_{44} = \frac{16\left(1-\nu^2\right)}{\pi E R^3}\int_{-b}^{b}\int_{0}^{a} x^2 y F_{IY}^2\left(\frac{y}{h}\right) dydx \tag{3.21}$$

$$c_{45} = c_{54} = \frac{64\left(1-\nu^2\right)}{\pi E R^3}\int_{0}^{b}\int_{0}^{a} xy\sqrt{1-x^2} F_{IX}\left(\frac{y}{h}\right) F_{IY}\left(\frac{y}{h}\right) dydx \tag{3.22}$$

$$c_{55} = \frac{32\left(1-\nu^2\right)}{\pi E R^3}\int_{-b}^{b}\int_{0}^{a} y\left(1-x^2\right) F_{IX}^2\left(\frac{y}{h}\right) dydx, \tag{3.23}$$

which are non-dimensionalized according to

$$\bar{c}_{22} = \frac{\pi E R}{\left(1-\nu^2\right)} c_{22} \tag{3.24}$$

$$\bar{c}_{33} = \frac{\pi E R}{\left(1-\nu^2\right)} c_{33} \tag{3.25}$$

$$\bar{c}_{44} = \frac{\pi E R^3}{\left(1-\nu^2\right)} c_{44} \tag{3.26}$$

$$\bar{c}_{45} = \frac{\pi E R^3}{\left(1-\nu^2\right)} c_{45} \tag{3.27}$$

$$\bar{c}_{55} = \frac{\pi E R^3}{\left(1-\nu^2\right)} c_{55}. \tag{3.28}$$

The corresponding stress intensity functions, for a unit width rectangular strip, are

$$F_{IX}\left(\frac{y}{h}\right) = \left[\frac{\tan\beta_C}{\beta_C}\right]^{1/2}\left[0.932+0.199(1-\sin\beta_C)^4\right]/\cos\beta_C \tag{3.29}$$

$$\begin{aligned} F_{IY}\left(\frac{y}{h}\right) &= \left[\frac{\tan\beta_C}{\beta_C}\right]^{1/2}\left[0.752+2.02\left(\frac{y}{h}\right)\right. \\ &\quad \left.+0.37(1-\sin\beta_C)^3\right]/\cos\beta_C \end{aligned} \tag{3.30}$$

$$\begin{aligned} F_{II}\left(\frac{y}{h}\right) &= \left[1.122-0.561\left(\frac{y}{h}\right)+0.085\left(\frac{y}{h}\right)^2\right. \\ &\quad \left.+0.18\left(\frac{y}{h}\right)^3\right]/\left(1-\frac{y}{h}\right)^{1/2} \end{aligned} \tag{3.31}$$

$$F_{III}\left(\frac{y}{h}\right) = \left[\frac{\tan\beta_C}{\beta_C}\right]^{1/2} \tag{3.32}$$

where

$$\beta_C = \frac{\pi y}{2h}. \tag{3.33}$$

The non-dimensional crack compliances, Eqs. 3.24 - 3.28, are calculated via numeric integration and plotted in Fig. 3.8. The results are corroborated versus the representative values provided in reference [30], and found to be in agreement. Note that singularities are present in the stress intensity functions, Eqs. 3.29 - 3.32, as discussed by Papadopolous [30]. These singularities are avoided by ending the numeric integration just before the singularity is reached (the singularities occur when y is equal to h). For small integration widths, the error provided by avoiding the singularity is small.

The compliance matrix of the cracked shaft is obtained using the transfer matrix, as discussed in Chapter 4 and Appendix D. The compliance matrix terms are the following, where the c_{ij} terms are the crack compliances calculated in Eqs. 3.19 - 3.23:

$$[C] = \begin{bmatrix} C_{11} & -c_{45}L_2^2 & c_{45}L_2 & C_{14} \\ -c_{45}L_2^2 & C_{22} & C_{23} & -c_{45}L_2 \\ c_{45}L_2 & C_{32} & C_{33} & c_{45} \\ C_{41} & -c_{45}L_2 & c_{45} & C_{44} \end{bmatrix}, \tag{3.34}$$

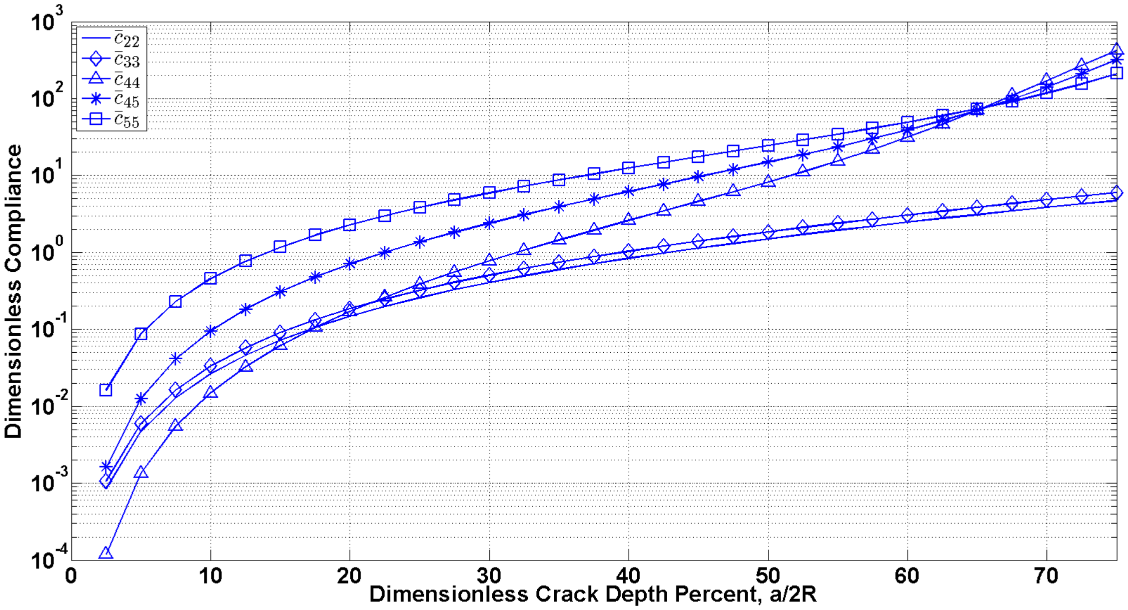

Figure 3.8: Non-dimensional crack compliances

where

$$C_{11} = c_{22} + c_{44}L_2^2 + \frac{(L_1+L_2)^3}{3EI} \tag{3.35}$$

$$C_{22} = c_{33} + c_{55}L_2^2 + \frac{(L_1+L_2)^3}{3EI} \tag{3.36}$$

$$C_{33} = c_{55} + \frac{(L_1+L_2)}{EI} \tag{3.37}$$

$$C_{44} = c_{44} + \frac{(L_1+L_2)}{EI} \tag{3.38}$$

and

$$C_{14} = C_{41} = c_{44}L_2 + \frac{(L_1+L_2)^2}{2EI} \tag{3.39}$$

$$C_{23} = C_{32} = -c_{55}L_2 - \frac{(L_1+L_2)^2}{2EI}. \tag{3.40}$$

When the additional compliances caused by the crack are negated, the compliance matrix reduces to that of an Euler-Bernoulli beam of length $L_1 + L_2$, as expected.

3.4 Test Rig Description

The overhung rotordynamic model presented earlier in the chapter is based upon the test rig discussed in Chapter 2. The overhung test rig was initially designed to monitor seal face dynamics [8, 9]. Following construction of the test rig, the coupled dynamic effects of the mechanical face seal and the shaft [7] were investigated. Finally, the feasibility of using the existing monitoring system to detect transverse shaft cracks was investigated by Green and Casey [1].

An overhung test rig was chosen for several reasons. First, an overhung shaft is considerably more flexible than a similar simply-supported shaft. The increased compliance allows for larger deflections at the rotor. Second, the overhung rotor prominently displays gyroscopic effects, which are important for the measured degrees of freedom γ_X and γ_Y. Finally, though not directly relevant to this work, the inclusion of a mechanical face seal is facilitated by the overhung nature of the shaft

The test rig is discussed herein for several reasons. First, the analytic results obtained in this work can be compared to the experimental results obtained previously using the test rig. Comparison to experimental results allows the shortcomings and advantages of the analytic models of this work to be discovered and discussed. Second, the damping approximation used in the analytic models is estimated from the test rig experimentally. Finally, the test rig can be used in the future to implement the diagnostic procedure provided by this work experimentally.

A schematic of the test rig modified for shaft crack detection is shown in Fig. 3.9. The rotordynamic test rig consists of an overhung shaft/rotor screwed into a precision spindle, which is in turn driven by an electric motor. The nature of the spindle mount is to provide cantilevered support to the shaft. For maintenance purposes, the test rig is constructed from three main parts. Further details on the test rig are provided by Varney and Green [2, 63], Casey [37], and Lee and Green [8].

A finite width rectangular notch was experimentally manufactured using electrical discharge machining at a single prescribed location along the shaft. Though the works by Varney and Green [2, 63, 64] and Green and Casey [1, 37] discuss the influence of crack depth, the effects of crack location are not discussed. A primary goal of this

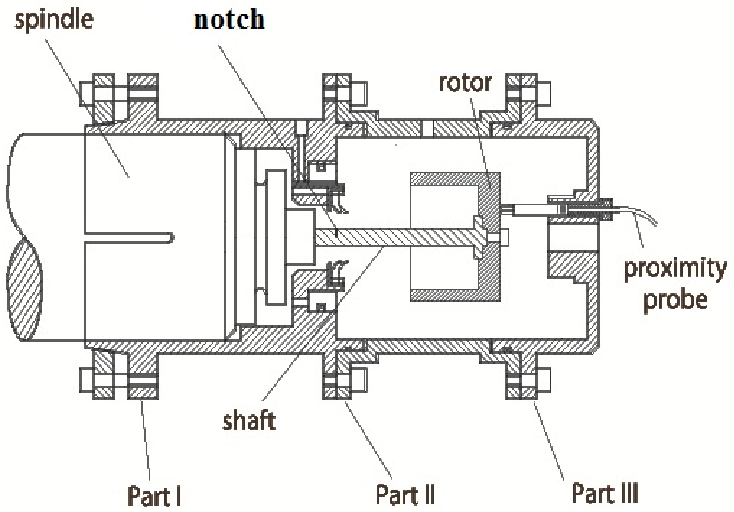

Figure 3.9: Overhung rotordynamic test rig modified for transverse crack detection

work is to investigate the effects of both crack location and depth on crack detection and diagnosis.

The test rig relies on three eddy-current proximity probes to measure the dynamic response of the rotor tilts, γ_X and γ_Y. A comprehensive discussion of the monitoring system and data analysis techniques employed on the test rig is found in the works by Varney and Green [2], Lee and Green [8], Dayan et al. [13], and Casey [37].

3.4.1 Shaft Damping

The system damping must be quantified to accurately capture the dynamic response of the rotor. Though only summarized here, additional details concerning the damping model and the procedure for experimentally measuring the damping parameters are found in references by Green and Casey [1], Varney and Green [2], and Casey [37].

A frequency-independent damping model is used to incorporate energy dissipation. Equivalent viscous damping constants for the system are then obtained. The energy dissipated per cycle via viscous damping is

$$E_{dis_v} = \pi \omega c_d |X|^2, \tag{3.41}$$

while the energy dissipated via structural damping per cycle is

$$E_{dis_s} = \pi \beta k |X|^2, \tag{3.42}$$

where ω is the response frequency, c_d is the equivalent viscous damping coefficient, k is the stiffness, β is the damping constant, and $|X|$ is the magnitude of the rotor's deflection (as measured following application of an impulse to the non-rotating cantilevered shaft). A value for an equivalent viscous damping coefficient c_{eq} is obtained by relating Eqs. 3.41 and 3.42 and solving for c_d (which is now the equivalent viscous damping coefficient, c_{eq}):

$$c_{eq} = \frac{\beta k}{\omega}. \tag{3.43}$$

Casey [37] describes a log decrement experimental procedure using the shaft from the test rig to obtain an estimate for β of approximately 0.01. This estimate is employed herein in Eq. 3.6.

3.4.2 Test Rig Parameters

The test rig parameters employed in this work's analytic models are provided. Once again, a detailed description is found in references [2, 8, 37].

The 10.2 mm diameter shaft is composed of AISI 4140 steel, and its length is 88.9 mm (as measured from the cantilevered base). The elastic modulus of the shaft is assumed to be 207 GPa, with a Poisson's Ratio of 0.33. The width of the experimentally manufactured notch is approximately 1.0 mm.

The rotor is composed of 440C stainless steel, and its mass is 0.573 kg. The polar mass moment of inertia is 3.85×10^{-4} kg m^2, and the transverse mass moment of inertia is 2.37×10^{-4} kg m^2. Furthermore, the rotor center of mass is offset axially from the end of the shaft by approximately 10.4 mm. The parallel axis theorem is used to obtain the rotor's rotational inertia properties at the end of the shaft.

The parameters of the overhung rotordynamic system are summarized in Table

Table 3.1: Test rig parameters

m	0.573 kg
I_t	2.37×10^{-4} kg · m^2
I_p	3.85×10^{-4} kg · m^2
E	207 GPa
L	88.9 mm
d	10.2 mm
ν	0.33

3.1. Experimental results obtained by Casey [37] and presented by Varney and Green [2] are discussed in Chapters 5 and 6.

3.5 Conclusions

An overhung model of an undamaged rotordynamic system is presented. Four degree of freedom linear equations of motion are developed using Newton-Euler mechanics in a rotating reference frame. Two gaping crack models are discussed, with emphasis placed on the respective compliance of each. The first model, the notch model, is a finite-width rectangular notch whose global reduction in stiffness arises from reduced area moments of inertia. The second crack model, the gaping fatigue crack, employs linear elastic fracture mechanics theory to estimate the crack compliance.

The mathematical models presented are used to obtain the dynamic response of the cracked system. Several mathematical tools are employed, one of which has been alluded to: the transfer matrix. Before discussing the dynamic response of each crack model, the transfer matrix method is discussed in greater detail.

CHAPTER IV

THE TRANSFER MATRIX METHOD: A NUMERICAL TECHNIQUE

The transfer matrix method is a discretization technique adept at quickly and accurately analyzing complex rotordynamic systems. The method seamlessly accounts for various rotordynamic properties and phenomena such as differing boundary conditions, support reactions (e.g., bearing stiffness and damping), external forcing (e.g., gravity, imbalance, etc.), and complicated geometry. The transfer matrix method condenses the steady-state equations of motion of an element into a single matrix relating the forces and displacements on one end of the element to those on the other.

The transfer matrix techniques employed herein assume lumped parameter systems. Inertial effects are incorporated into a point matrix, and elastic effects are encapsulated into a field matrix. The point and field matrices use continuity and force-moment balances to update a state vector across an element. By propagating a state vector through the elements of a system, an overall transfer matrix is obtained relating the boundary conditions of the system. The transfer matrix method is capable of providing both the free and forced system response.

Transfer matrix methods and finite element techniques share several concepts. Genta [35] proves that the two methods are equivalent, given the same discretization. Furthermore, both methods rely on discretizing the system into a series of elemental components. The transfer matrix is chosen over finite element analysis because of the following:

1. Simplicity: sequential multiplication of transfer matrices is natural to rotordynamic systems.

Table 4.1: Summary of transfer matrix methods

Technique	Primary Purpose
RTM	Inclusion of stiffness asymmetry
CTM	Separation of forward and backward whirl
CETM	Inclusion of external forcing

2. The ease of symbolic manipulations.
3. Expedience in extracting the system's steady state response.

However, finite element analysis does have several advantages over the transfer matrix method. First, finite element analysis allows for the incorporation of non-linear effects. The non-linear nature of a breathing crack would necessitate the use finite element methods. Second, the method's robustness allows for analysis of many varieties of rotordynamic systems (whereas the transfer matrix method is suitable only for sequential, in-line systems).

This work provides several transfer matrix techniques to obtain the free and forced system response. The Real Transfer Matrix (RTM) employs real-valued coordinates to analyze orthotropic rotordynamic systems, such as a rotating cracked shaft. A novel transfer matrix technique, the Complex Transfer Matrix (CTM), is provided to distinguish forward and backward whirl. The Complex Extended Transfer Matrix (CETM) is discussed in relation to its ability to incorporate external forcing [1, 7]. These transfer matrix techniques are summarized with their primary purposes in Table 4.1. Prior to presenting the aforementioned transfer matrices, a brief discussion of rotordynamic analysis in a rotating reference frame is given.

4.1 Rotordynamic Analysis in a Rotating Reference Frame

While the analysis of cracked rotating systems is conveniently performed in a rotating reference frame, diagnostics typically rely on inertial frame measurements. Thus, understanding the relation between a rotating and inertial frame analysis is crucial in developing the diagnostic routines suggested in this work.

Several aspects of rotating frame rotordynamic analysis must be discussed to elucidate meaningful interpretation of later results. The eigenvalues of a rotordynamic system represent the whirl speeds; whirl occurs when the shaft precesses about the undeflected shaft axis. Whirl frequencies are synchronous or non-synchronous; synchronous whirl occurs when the whirl frequency coincides with the frequency of shaft rotation. Furthermore, whirl is characterized by its direction relative to the shaft rotation. Forward whirl occurs in the direction of shaft rotation, while backward whirl occurs opposite the direction of shaft rotation.

It is well known [1, 19, 41, 65] that rotating-frame eigenvalues are shifted from the absolute eigenvalues by the shaft speed of the system according to

$$p = p_r + n, \tag{4.1}$$

where p is the absolute eigenvalue, p_r is the relative eigenvalue, and n is the shaft speed.

A useful visualization tool for rotordynamic analysis is the Campbell diagram. The Campbell diagram is a locus of whirl frequencies plotted versus shaft speed. On the Campbell diagram, the inertial synchronous whirl frequencies are found by locating the intersections between lines $p = \pm n$ and the locus of eigenvalues. Equivalent intersection lines for a rotating frame analysis are obtained by solving Eq. 4.1 for the relative eigenvalue p_r:

$$p_r = p - n. \tag{4.2}$$

To obtain forward synchronous whirl frequencies in a rotating frame, it is clear that p_r

Table 4.2: Campbell diagram intersection lines

	Forward Whirl	Backward Whirl
Inertial Frame	$p = n$	$p = -n$
Rotating Frame	$p_r = 0$	$p_r = -2n$

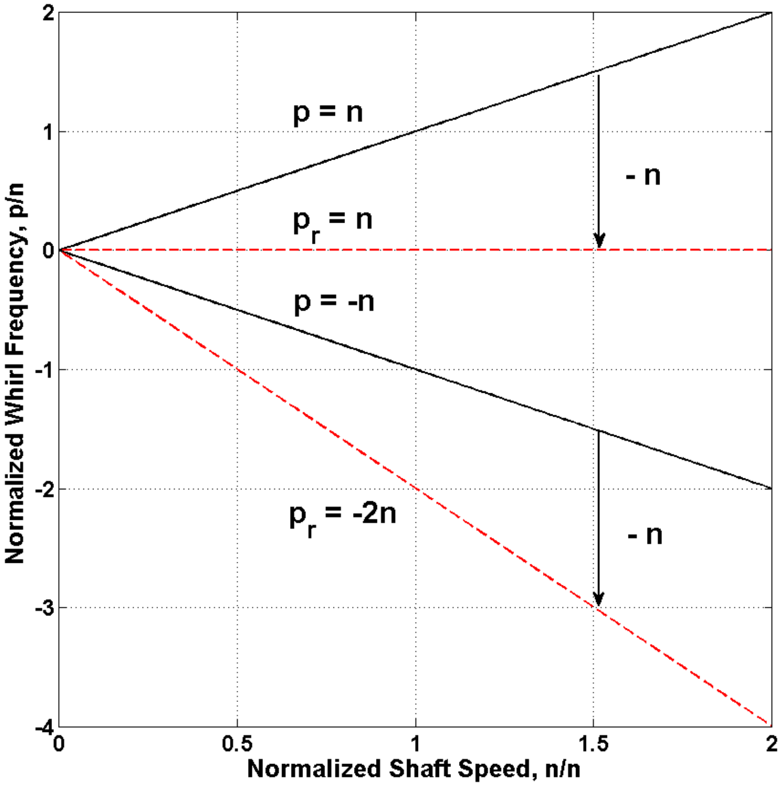

Figure 4.1: Relative whirl on the Campbell diagram

must be set to zero in the characteristic equation (found from a transfer matrix analysis). Likewise, to obtain backward synchronous whirl, n must be set to $-\frac{1}{2}p_r$. The inertial intersection lines $p = \pm n$ are shifted down by the shaft speed n to obtain the corresponding rotating frame intersection lines, as shown in Fig. 4.1. The quantities in the figure are shown normalized by the shaft speed. The normalization procedure is performed to emphasize the slopes of the intersection lines. The intersection lines highlighting synchronous whirl on the Campbell diagram are summarized in Table 4.2 for inertial and rotating reference frames. An intuitive explanation for these results is provided by Varney and Green [36].

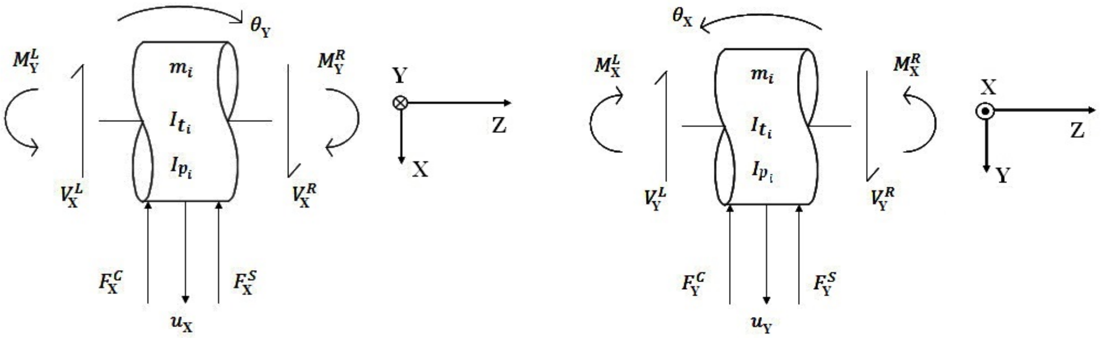

(a) Bending in the XZ plane (b) Bending in the YZ plane

Figure 4.2: Point element formulation

4.2 The Real Transfer Matrix

The Real Transfer Matrix (RTM) uses real-valued coordinates to model rotordynamic systems where the properties of the system can be different in orthogonal planes. The RTM is therefore capable of analyzing cracked rotordynamic systems where the stiffness of the shaft is asymmetric.

The RTM suffers from several shortcomings. The principle shortcoming is the method's inability to distinguish forward and backward whirl (as will be seen, this shortcoming leads to the development of the Complex Transfer Matrix). The RTM state vector contains eight quantities; therefore, eight eigenvalues are expected per discretized mass. The redundancy in eigenvalues leads to a duplication of each whirl speed, concealing the direction of each. Also, the typical transfer matrix can result in prohibitively large characteristic equations for systems with a relatively small number of point masses. The high order of the characteristic equation results in loss of computation speed and accuracy. The Complex Transfer Matrix remedies these issues, as discussed shortly.

4.2.1 Inertial Effects: The Point Matrix

A general free-body diagram of a rigid element with finite inertia is provided in Fig. 4.2, where the relevant degrees of freedom are shown (though coordinates X and

Y are shown, the figure is equally valid for inertial coordinates ξ and η). The faces of the point element are designated by the superscripts R and L, which refer to the right and left faces of the point element, respectively. The face designation of any element is maintained relative to the face of the point element which it contacts [19]; this concept is further discussed in the derivation of the field matrix.

Following the procedure dictated by Lee and Green [7], the 8×1 state vector at the j^{th} node in the rotating frame XYZ is

$$\{S\}_j = \{\ u_X \quad \gamma_Y \quad M_Y \quad -V_X \quad -u_Y \quad \gamma_X \quad M_X \quad V_Y\}^T \ , \tag{4.3}$$

where u, γ, M, and V denote linear displacement, angular displacement, bending moment, and shear in the direction specified by the subscript X or Y. These terms are shown in Figure 4.2. The corresponding inertial frame state vector is

$$\{S\}_j = \{\ u_\xi \quad \gamma_\eta \quad M_\eta \quad -V_\xi \quad -u_\eta \quad \gamma_\xi \quad M_\xi \quad V_\eta\}^T \ , \tag{4.4}$$

where once again the subscript indicates the corresponding direction. The point matrix $[P_j]$ updates the state vector from the left to the right end of element j according to

$$\{S\}_j^R = [P_j]\,\{S\}_j^L \ . \tag{4.5}$$

It is often convenient to express the stiffness of a cracked rotordynamic system in a rotating frame. However, condition monitoring systems typically measure an inertial frame response. For this reason, point matrices are provided in both inertial and rotating reference frames.

4.2.1.1 Inertial Reference Frame

The derivation of the point matrix in an inertial reference frame is provided in Appendix E. The inertial point matrix $[P_j]$ for the j^{th} mass m (where the system is composed of $j = 1, 2, ..., N$ lumped masses) is the following:

$$[P_j]^I_{8\times8} = \begin{bmatrix} 1 & 0 & 0 & 0 & 0 & 0 & 0 & 0 \\ 0 & 1 & 0 & 0 & 0 & 0 & 0 & 0 \\ 0 & -I_t p^2 & 1 & 0 & 0 & -iI_p np & 0 & 0 \\ mp^2 - id_{\xi\xi}p - k_{\xi\xi} & 0 & 0 & 1 & id_{\xi\eta}p + k_{\xi\eta} & 0 & 0 & 0 \\ 0 & 0 & 0 & 0 & 1 & 0 & 0 & 0 \\ 0 & 0 & 0 & 0 & 0 & 1 & 0 & 0 \\ 0 & iI_p np & 0 & 0 & 0 & -I_t p^2 & 1 & 0 \\ id_{\eta\xi}p + k_{\eta\xi} & 0 & 0 & 0 & mp^2 - id_{\eta\eta}p - k_{\eta\eta} & 0 & 0 & 1 \end{bmatrix}, \tag{4.6}$$

where p is the inertial whirl frequency, n is the shaft speed, and the polar and transverse mass moments of inertia are I_t and I_p, respectively. The superscript I indicates that the matrix is defined in an inertial reference frame (thus, the state vector given in Eq. 4.4 is employed). External stiffness and damping forces, such as those arising due to a bearing or seal, are incorporated through the stiffness and damping coefficients k_{ij} and d_{ij}, respectively.

4.2.1.2 Rotating Reference Frame

The rotating-frame point matrix (designated by superscript RF) is found from the rotating frame angular momentum and acceleration (derived in Appendix A) to be

$$[P_j]^{RF}_{8\times8} = \begin{bmatrix} [D]_{4\times4} & -[G]_{4\times4} \\ [G]_{4\times4} & [D]_{4\times4} \end{bmatrix}, \tag{4.7}$$

where

$$[D]_{4\times4} = \begin{bmatrix} 1 & 0 & 0 & 0 \\ 0 & 1 & 0 & 0 \\ 0 & (I_p - I_t)\, n^2 - I_t\, p_r^2 & 1 & 0 \\ m\,(p_r^2 + n^2) & 0 & 0 & 1 \end{bmatrix} \tag{4.8}$$

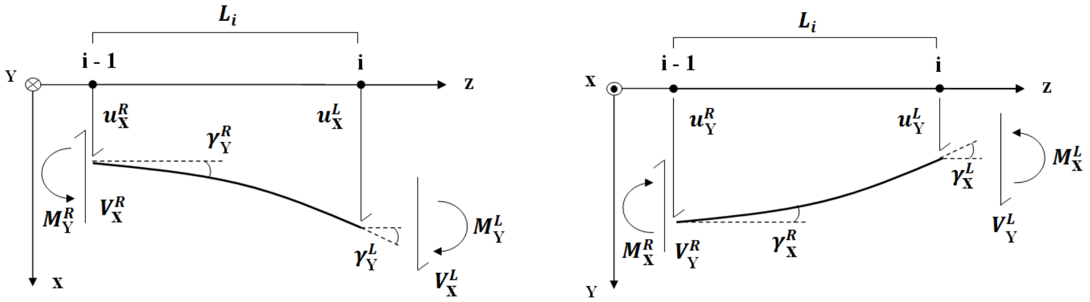

(a) Bending in the xz plane

(b) Bending in the yz plane

Figure 4.3: Field element formulation

and

$$[G]_{4\times 4} = \begin{bmatrix} 0 & 0 & 0 & 0 \\ 0 & 0 & 0 & 0 \\ 0 & -i(2I_t - I_p)np_r & 0 & 0 \\ 2i\,m\,n\,p_r & 0 & 0 & 0 \end{bmatrix}. \tag{4.9}$$

In this case the rotating frame state vector, Eq. 4.3, is used. It is important to recognize that the response occurs at the relative whirl frequency p_r. Also, note that external stiffness and damping forces have been excluded for the rotating frame analysis, as these forces would appear as forcing vectors rotating counter to the direction of shaft rotation. In this case, application of the Complex Extended Transfer Matrix would be required.

4.2.2 Elastic Effects: The Field Matrix

The field matrix for a massless beam segment is obtained from Euler-Bernoulli beam theory. Figures 4.3a and 4.3b show a beam element undergoing two-plane bending; the face designations are defined relative to the adjacent point element. The field matrix updates the state vector from the right face of element $j-1$ to the left face of element j according to

$$\{S\}_j^L = [F_j]\{S\}_{j-1}^R, \tag{4.10}$$

which is valid for both rotating and inertial reference frames. Lee and Green [7] develop the field matrix for a beam segment displaying a constant cross-section:

$$[F_j] = \begin{bmatrix} 1 & L & \dfrac{L^2}{2EI} & \dfrac{L^3}{6EI} & 0 & 0 & 0 & 0 \\ 0 & 1 & \dfrac{L}{EI} & \dfrac{L^2}{2EI} & 0 & 0 & 0 & 0 \\ 0 & 0 & 1 & L & 0 & 0 & 0 & 0 \\ 0 & 0 & 0 & 1 & 0 & 0 & 0 & 0 \\ 0 & 0 & 0 & 0 & 1 & L & \dfrac{L^2}{2EI} & \dfrac{L^3}{6EI} \\ 0 & 0 & 0 & 0 & 0 & 1 & \dfrac{L}{EI} & \dfrac{L^2}{2EI} \\ 0 & 0 & 0 & 0 & 0 & 0 & 1 & L \\ 0 & 0 & 0 & 0 & 0 & 0 & 0 & 1 \end{bmatrix}. \tag{4.11}$$

The length of beam segment j is L, the elastic modulus is E, and the area moment of inertia about a transverse axis is I.

Varney and Green [2] employ a similar technique to develop a field matrix for a beam segment with an asymmetric cross-section. The only stipulation for the geometry of the cross-section is that either the XZ or YZ plane must be a plane of symmetry. The asymmetric field matrix is

$$[F]_{asym} = \begin{bmatrix} [F_X]_{4\times4} & [0]_{4\times4} \\ [0]_{4\times4} & [F_Y]_{4\times4} \end{bmatrix}, \tag{4.12}$$

where

$$[F_X]_{4\times4} = \begin{bmatrix} 1 & L_c & \dfrac{L_c^2}{2EI_{\bar{y}}} & \dfrac{L_c^3}{6EI_{\bar{y}}} \\ 0 & 1 & \dfrac{L_c}{EI_{\bar{y}}} & \dfrac{L_c^2}{2EI_{\bar{y}}} \\ 0 & 0 & 1 & L_c \\ 0 & 0 & 0 & 1 \end{bmatrix} \tag{4.13}$$

and

$$[F_Y]_{4\times 4} = \begin{bmatrix} 1 & L_c & \dfrac{L_c^2}{2EI_{\bar{x}}} & \dfrac{L_c^3}{6EI_{\bar{x}}} \\ 0 & 1 & \dfrac{L_c}{EI_{\bar{x}}} & \dfrac{L_c^2}{2EI_{\bar{x}}} \\ 0 & 0 & 1 & L_c \\ 0 & 0 & 0 & 1 \end{bmatrix}. \tag{4.14}$$

The subscript on the area moment of inertia indicates the axis about which it is computed. The asymmetric field matrix is valid only for a rotating frame analysis.

A transfer matrix corresponding to a gaping fatigue crack is provided by Green and Casey [1]. The compliance matrix of the gaping fatigue crack, Eq. 3.18, is rearranged into a transfer matrix form:

$$[F_{crack}]_{8\times 8} = \begin{bmatrix} 1 & 0 & 0 & -c_{22} & 0 & 0 & 0 & 0 \\ 0 & 1 & c_{44} & 0 & 0 & 0 & c_{45} & 0 \\ 0 & 0 & 1 & 0 & 0 & 0 & 0 & 0 \\ 0 & 0 & 0 & 1 & 0 & 0 & 0 & 0 \\ 0 & 0 & 0 & 0 & 1 & 0 & 0 & -c_{33} \\ 0 & 0 & c_{54} & 0 & 0 & 1 & c_{55} & 0 \\ 0 & 0 & 0 & 0 & 0 & 0 & 1 & 0 \\ 0 & 0 & 0 & 0 & 0 & 0 & 0 & 1 \end{bmatrix}, \tag{4.15}$$

where the c_{ij} terms are given in Eqs. 3.19 - 3.23.

4.2.3 The Overall Transfer Matrix: Assembling System Elements

Discrete system elements are related through the equivalence of coincident state vectors. By propagating the state vector through the system, a single matrix is found to associate the boundary conditions. A detailed explanation of the process is given by Pestel and Leckie [34], Lee and Green [7], and Rao [19].

The transfer matrix technique is demonstrated using the simple system shown in Fig. 4.4. The overhung system consists of three shaft segments of varying cross-section, and a lumped mass on the free end. The shaft segments are numbered as

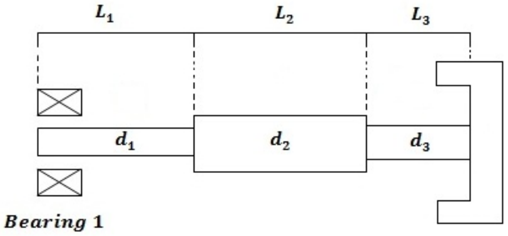

Figure 4.4: General overhung rotordynamic system

indicated by the subscripts in the figure. Though an inertial frame is employed in this example, the method is identical for a rotating frame analysis (except for the form of the elemental matrices). The cantilevered boundary conditions for the overhung shaft are captured by the state vector at the support:

$$\{S\}^{SU} = \{\ 0 \quad 0 \quad M_\eta \quad -V_\xi \quad 0 \quad 0 \quad M_\xi \quad V_\eta\}^T\ , \tag{4.16}$$

where SU designates the support boundary conditions. At the free end, no shear or moment exists:

$$\{S\}^{FE} = \{\ u_\xi \quad \gamma_\eta \quad 0 \quad 0 \quad -u_\eta \quad \gamma_\xi \quad 0 \quad 0\}^T \tag{4.17}$$

where the superscript FE signifies the free end. The cantilever boundary conditions are chosen for this example because they are identical to those of the overhung rotor modeled elsewhere in this work. Beginning with the support, the state vector on the right of shaft element one is

$$\{S\}_1^R = [F_1]\{S\}^{SU}, \tag{4.18}$$

where $[F_1]$ is the field matrix for shaft segment one. Enforcement of continuity necessitates the following:

$$\{S\}_2^R = [F_2][F_1]\{S\}^{SU}. \tag{4.19}$$

It is important to recognize that the designation of right and left for a field element is opposite that of a point element. Continuing in a similar fashion provides the following relationship between the boundary conditions:

$$\{S\}^{FE} = [P_1][F_3][F_2][F_1]\{S\}^{SU}, \tag{4.20}$$

where $[P_1]$ is the point matrix for the lumped rotor. The overall transfer matrix $[U]$ results from multiplication of the individual element matrices:

$$[U] = [P_1][F_3][F_2][F_1]. \tag{4.21}$$

Application of the specific boundary conditions (Eqs. 4.16 and 4.17) gives the following:

$$\begin{Bmatrix} u_\xi \\ \gamma_\eta \\ 0 \\ 0 \\ -u_\eta \\ \gamma_\xi \\ 0 \\ 0 \end{Bmatrix} = \begin{bmatrix} U_{11} & U_{12} & U_{13} & U_{14} & U_{15} & U_{16} & U_{17} & U_{18} \\ U_{21} & U_{22} & U_{23} & U_{24} & U_{25} & U_{26} & U_{27} & U_{28} \\ U_{31} & U_{32} & U_{33} & U_{34} & U_{35} & U_{36} & U_{37} & U_{38} \\ U_{41} & U_{42} & U_{43} & U_{44} & U_{45} & U_{46} & U_{47} & U_{48} \\ U_{51} & U_{52} & U_{53} & U_{54} & U_{55} & U_{56} & U_{57} & U_{58} \\ U_{61} & U_{62} & U_{63} & U_{64} & U_{65} & U_{66} & U_{67} & U_{68} \\ U_{71} & U_{72} & U_{73} & U_{74} & U_{75} & U_{76} & U_{77} & U_{78} \\ U_{81} & U_{82} & U_{83} & U_{84} & U_{85} & U_{86} & U_{87} & U_{88} \end{bmatrix} \begin{Bmatrix} 0 \\ 0 \\ M_\eta \\ -V_\xi \\ 0 \\ 0 \\ M_\xi \\ V_\eta \end{Bmatrix}, \tag{4.22}$$

where the entries of the overall transfer matrix $[U]$ are found from Eq. 4.21. Extracting the eigenvalue problem gives a reduced overall transfer matrix:

$$\begin{Bmatrix} 0 \\ 0 \\ 0 \\ 0 \end{Bmatrix} = \begin{bmatrix} U_{33} & U_{34} & U_{37} & U_{38} \\ U_{43} & U_{44} & U_{47} & U_{48} \\ U_{73} & U_{74} & U_{77} & U_{78} \\ U_{83} & U_{84} & U_{87} & U_{88} \end{bmatrix} \begin{Bmatrix} M_\eta \\ -V_\xi \\ M_\xi \\ V_\eta \end{Bmatrix}. \tag{4.23}$$

The determinant of this matrix is a polynomial characteristic equation in p, the roots of which are the eigenvalues of the system (see Rao [19] for more detail).

4.3 The Complex Transfer Matrix

A shortcoming of the RTM method is the inability to distinguish forward and backward whirl directions. A novel complex redefinition of the state vector quantities is proposed to reduce the 8×8 transfer matrix to a 4×4 form, and is deemed the

Complex Transfer Matrix (see Varney and Green [36] for additional detail). The new formulation results in several advantages: increased computational efficiency, improved accuracy, and separation of forward and backward whirl.

The basis of the Complex Transfer Matrix is a complex coordinate redefinition of the state vector elements, which is valid for both the inertial and rotating reference frames (though rotating frame coordinates are shown below):

$$\begin{aligned} u &= u_X + i\,u_Y \\ \gamma &= \gamma_X + i\,\gamma_Y \\ M &= M_X + i\,M_Y \\ V &= V_X + i\,V_Y. \end{aligned} \tag{4.24}$$

This coordinate redefinition reduces the state vector from the form in Eq. 4.3 to

$$\{S\}_j = \{\ -u \quad \gamma \quad M \quad V\ \}^T. \tag{4.25}$$

The point and field matrices are reformulated using this complex coordinate redefinition, for both an inertial and rotating reference frame.

4.3.1 Development in an Inertial Reference Frame

Application of the complex coordinate redefinition in Eq. 4.24 condenses the inertial frame point matrix, Eq. 4.6, into

$$[P_j]^I_{4\times 4} = \begin{bmatrix} 1 & 0 & 0 & 0 \\ 0 & 1 & 0 & 0 \\ 0 & -I_t\,p^2 + I_p\,n\,p & 1 & 0 \\ m\,p^2 + W_{ext} & 0 & 0 & 1 \end{bmatrix}, \tag{4.26}$$

where W_{ext} includes the effects of external stiffness and damping:

$$W_{ext} = -(d_{\xi\xi} + i\,d_{\xi\eta})\,p - (k_{\xi\xi} - i\,k_{\xi\eta}). \tag{4.27}$$

It is imperative to note that the reduction of external stiffness and damping depends on the following assumptions: $k_{\xi\xi} = k_{\eta\eta}$, $k_{\eta\xi} = -k_{\xi\eta}$, $d_{\xi\xi} = d_{\eta\eta}$, and $d_{\eta\xi} = -d_{\xi\eta}$. These limitations on the stiffness and damping coefficients should pose no problem considering the stiffness and damping in the ξ and η directions are typically close in magnitude. In the rare case when they are not, the values can be averaged to obtain an approximate value.

The complex coordinate redefinition results in the following 4×4 complex field matrix for symmetric beam element j:

$$[F_j]_{4\times4} = \begin{bmatrix} 1 & iL & i\frac{L^2}{2EI} & \frac{L^3}{6EI} \\ 0 & 1 & \frac{L}{EI} & -i\frac{L^2}{2EI} \\ 0 & 0 & 1 & -iL \\ 0 & 0 & 0 & 1 \end{bmatrix}, \tag{4.28}$$

which is valid only for beams with a symmetric cross-section.

This method is designated the Complex Transfer Matrix due to the nature of the transformation and the nature of the matrix elements themselves. The 4×4 field matrix in Eq. 4.28 is inherently complex, and the 4×4 point matrix in Eq. 4.26 contains complex terms if $d_{\xi\eta}$ and $k_{\xi\eta}$ are non-zero.

4.3.2 Development in a Rotating Reference Frame

Application of Eq. 4.24 to the steady-state rotating frame equations of motion results in the following 4×4 point matrix for mass j:

$$[P_j]^{RF}_{4\times4} = \begin{bmatrix} 1 & 0 & 0 & 0 \\ 0 & 1 & 0 & 0 \\ 0 & I_p n(p_r + n) - I_t(p_r + n)^2 & 1 & 0 \\ m(p_r + n)^2 & 0 & 0 & 1 \end{bmatrix}. \tag{4.29}$$

The absolute eigenvalue p is related to the relative eigenvalue p_r by Eq. 4.2. When p is replaced by $p_r + n$, Eq. 4.29 reduces to Eq. 4.26. The rotating frame, complex field matrix $[F]$ is identical to Eq. 4.28. Appendix F discusses why the CTM separates forward and backward whirl and provides a simple example demonstrating the separation.

4.4 Incorporation of Excitation: The Complex Extended Transfer Matrix

The transfer matrix techniques discussed thus far are valid only for free response analysis. However, understanding the forced response is crucial for vibration monitoring diagnostics. Adapting the transfer matrix to allow the inclusion of forcing is imperative. One such adaptation is the Complex Extended Transfer Matrix (CETM). The CETM is developed by Lee and Green [7] to systematically incorporate forcing into the transfer matrix. The premise underlying the CETM method is an expansion of the field matrices from 8×8 to 9×9. As is demonstrated, this dimension expansion allows for the inclusion of forcing. An expansion of the transfer matrices requires a corresponding expansion of the state vector, where an entry of unity is concatenated unto Eq. 4.3:

$$\{S\}_j = \{\; u_X \quad \gamma_Y \quad M_Y \quad -V_X \quad -u_Y \quad \gamma_X \quad M_X \quad V_Y \quad 1\}^T \;. \tag{4.30}$$

Though the rotating frame state vector is used here as an example, the technique is equally applicable to analysis in an inertial frame. Damping is introduced into the system to calculate the forced response. Following the procedure of Green and Casey [1], the point matrix for rotor j accounting for external excitation and damping is

$$[P_j]_{9\times 9} = \begin{bmatrix} [P_j]_{8\times 8} & \{0\} \\ \{0\} & 1 \end{bmatrix} + \left[\hat{P}_j\right]_{9\times 9}, \tag{4.31}$$

where $[\hat{P}_j]_{9\times 9}$ is a matrix incorporating excitation and damping effects, as derived below. The material damping forces on the rotor are the following:

$$\begin{Bmatrix} F_X^D \\ F_Y^D \\ M_X^D \\ M_Y^D \end{Bmatrix} = \begin{bmatrix} d_{11_Y} & 0 & 0 & -d_{12_Y} \\ 0 & d_{11_X} & d_{12_X} & 0 \\ 0 & d_{21_X} & d_{22_X} & 0 \\ -d_{21_Y} & 0 & 0 & d_{22_Y} \end{bmatrix} \begin{Bmatrix} \dot{u}_X \\ \dot{u}_Y \\ \dot{\gamma}_X \\ \dot{\gamma}_Y \end{Bmatrix}, \tag{4.32}$$

where the damping coefficients are provided in Eq. 3.6. Forcing due to gravity is a constant radial force in the inertial frame. Thus, in the rotating frame, gravity is modeled as a vector rotating counter to the shaft speed (see Fig. 3.2):

$$F_g = mge^{-int} \tag{4.33}$$

or, in vector notation:

$$\begin{Bmatrix} F_X^g \\ F_Y^g \\ M_X^g \\ M_Y^g \end{Bmatrix} = \begin{Bmatrix} mg\,\cos(nt) \\ -mg\,\sin(nt) \\ 0 \\ 0 \end{Bmatrix}, \tag{4.34}$$

where the gravitational constant is g and t is time. The total forcing due to gravity and damping is the sum of the contribution from both:

$$\begin{Bmatrix} F_X^g + F_X^D \\ F_Y^g + F_Y^D \\ M_X^g + M_X^D \\ M_Y^g + M_Y^D \end{Bmatrix} = \begin{Bmatrix} mg\,\cos(nt) + d_{11_Y}\dot{u}_X - d_{12_Y}\dot{\gamma}_Y \\ -mg\,\sin(nt) + d_{11_X}\dot{u}_Y + d_{12_X}\dot{\gamma}_X \\ d_{21_X}\dot{u}_Y + d_{22_X}\dot{\gamma}_X \\ -d_{21_Y}\dot{u}_X + d_{22_Y}\dot{\gamma}_Y \end{Bmatrix}. \tag{4.35}$$

The steady-state response of the system is found by assuming a solution in the same form of the excitation. In complex notation, $\cos(nt)$ becomes the real part of e^{int}, while $\sin(nt)$ become the real part of $-ie^{-int}$. As forcing occurs at frequency n, the response of the system is synchronous at n. The solution to each state vector quantity is then of the general form

$$q_j = Q_j e^{int}. \tag{4.36}$$

Adopting complex notation for the sinusoidal terms and assuming solutions for the state variables gives the external forcing on rotor j:

$$\left\{ \begin{array}{c} F_X^g + F_X^D \\ F_Y^g + F_Y^D \\ M_X^g + M_X^D \\ M_Y^g + M_Y^D \end{array} \right\}_j = \left\{ \begin{array}{c} m_j g \, + i\, n\, d_{11_Y} u_X - i\, n\, d_{12_Y} \gamma_Y \\ i\, m_j g \, + i\, n\, d_{11_X} u_Y + i\, n\, d_{12_X} \gamma_X \\ i\, n\, d_{21_X} u_Y + i\, n\, d_{22_X} \gamma_X \\ -i\, n\, d_{21_Y} u_X + i\, n\, d_{22_Y} \gamma_Y \end{array} \right\}_j . \tag{4.37}$$

Rearranging Eq. 4.37 into transfer matrix form provides the damped forced response matrix $[\hat{P}_j]_{9\times 9}$ for rotor j in the rotating frame:

$$\left[\hat{P}_j\right]_{9\times 9}^{RF} = \begin{bmatrix} 0 & 0 & 0 & 0 & 0 & 0 & 0 & 0 & 0 \\ 0 & 0 & 0 & 0 & 0 & 0 & 0 & 0 & 0 \\ ind_{21_Y} & -ind_{22_Y} & 0 & 0 & 0 & 0 & 0 & 0 & 0 \\ ind_{11_Y} & -ind_{12_Y} & 0 & 0 & 0 & 0 & 0 & 0 & mg \\ 0 & 0 & 0 & 0 & 0 & 0 & 0 & 0 & 0 \\ 0 & 0 & 0 & 0 & 0 & 0 & 0 & 0 & 0 \\ 0 & 0 & 0 & 0 & ind_{21_X} & -ind_{22_X} & 0 & 0 & 0 \\ 0 & 0 & 0 & 0 & ind_{11_X} & -ind_{12_X} & 0 & 0 & -img \\ 0 & 0 & 0 & 0 & 0 & 0 & 0 & 0 & 0 \end{bmatrix} . \tag{4.38}$$

A similar procedure could be followed for an inertial reference frame. The CETM field matrix remains similar to Eq. 4.11, though expanded to maintain consistency:

$$[F_j]_{9\times 9} = \begin{bmatrix} [F_j]_{8\times 8} & \{0\} \\ \{0\} & 1 \end{bmatrix} . \tag{4.39}$$

A concept central to the CETM is synchronous whirl. Since forcing is applied to the system at a known frequency, the response of the system occurs at that frequency. In the common case that the excitation frequency is the shaft speed, the whirl becomes synchronous. Also, recognize that though the Real Transfer Matrix is employed to motivate the CETM method, the procedure is equally applicable to the Complex Transfer Matrix. However, the benefit of using the Complex Transfer Matrix arises when solving the associated eigenvalue problem, as the order of the characteristic equation is reduced. For a forced response analysis, the Complex Transfer Matrix provides no practical reduction in computation time. It is also important to solve separately for forward and backward whirl components when using the CETM. The sign of the shaft speed in the gyroscopic effect should be taken as positive for forward whirl, and negative for backward whirl.

4.5 Conclusions

To summarize, the transfer matrix method is a numerical discretization technique relying on elemental transfer matrices. These matrices are used to propagate a state vector through a rotordynamic system. Two transfer matrix techniques are developed: the Real Transfer Matrix and the Complex Transfer Matrix. The RTM is suited for analysis of orthotropic systems, such as cracked shafts. However, the method can be computationally inefficient or even inaccurate for systems with many point elements. Furthermore, the RTM does not distinguish between forward and backward whirl.

The Complex Transfer Matrix employs a complex coordinate redefinition to condense the state vector employed in the RTM into a reduced form. This coordinate redefinition decreases the state vector from 8×1 to 4×1. The resulting Complex Transfer Matrix has increased computational efficiency and naturally distinguishes whirl direction. Also, a method for incorporating external excitation and damping effects is discussed. Incorporating these effects is important, as vibration monitoring transducers observe the system forced response. Two analytical techniques are now available to analyze the cracked rotordynamic system: the equations of motion and the transfer matrix.

CHAPTER V

ANALYTIC RESULTS: FREE RESPONSE

The 2X resonance frequency is a valuable diagnostic tool for cracked rotordynamic systems. The 2X resonance occurs when the shaft speed equals half of a natural frequency. To obtain the 2X resonance frequency, a free response analysis must be performed.

The free response of the cracked rotordynamic system is obtained for both crack models (the notch crack and gaping fatigue crack) using the equations of motion derived in Chapter 3. For each crack model, the results presented are as follows. First, the free response is obtained for a system displaying a fixed-location crack with variable depth. These results are presented to compare with the analytic and experimental results obtained by Green and Casey [1] and Varney and Green [2]. Next, variations in both crack depth and location are investigated for diagnostic purposes. The 2X resonance frequencies are given for many pairs of feasible crack depths and locations. A state space form of the equations of motion is presented to facilitate the analysis.

Only the results of the free response analysis are presented in this chapter. These results are interpreted in Chapter 7 in relation to the detection and diagnosis of transverse shaft cracks.

5.1 State Space Representation of Equations of Motion

Recall the four degree-of-freedom coupled equations of motion for the cracked rotordynamic system:

$$[M]\{\ddot{q}\} + ([D] + [G])\{\dot{q}\} + \left([C]^{-1} - [E]\right)\{q\} = \{F\}, \tag{5.1}$$

where the vector of generalized coordinates $\{q\}$ is

$$\{q\} = \{u_X \;\; u_Y \;\; \gamma_X \;\; \gamma_Y\}^T . \tag{5.2}$$

The equations of motion are solved using a state space formulation of Eq. 5.1. The following state vector representation is employed:

$$\{x\} = \left\{ \begin{array}{c} \{q\} \\ \{\dot{q}\} \end{array} \right\} . \tag{5.3}$$

Following the procedure outlined by Ginsberg [65] provides the state space equations of motion:

$$[S]\{\dot{x}\} - [R]\{x\} = \left\{ \begin{array}{c} \{0\} \\ \{F\} \end{array} \right\} , \tag{5.4}$$

where the state matrices are

$$[S] = \left[\begin{array}{cc} -([C]^{-1} - [E]) & [0] \\ [0] & [M] \end{array} \right] \tag{5.5}$$

and

$$[R] = \left[\begin{array}{cc} [0] & -([C]^{-1} - [E]) \\ -([C]^{-1} - [E]) & -([D] + [G]) \end{array} \right] . \tag{5.6}$$

The state space equations of motion are used to perform both free and forced response analyses.

The equations of motion provide an expedient mechanism for performing a free response analysis of the system. A free response analysis provides the natural frequencies of the system, which are directly related to the 2X resonance frequency. However, general symmetric eigenvalue techniques are not applicable to the problem at hand, as the matrix $[R]$ is asymmetric. An adjoint (i.e., right and left) eigenvalue problem is applied to obtain the natural frequencies of the system. Ginsberg [65] defines the right and left eigenvalue problems as

$$[[R] - \lambda_j [S]]\{\psi_j\} = \{0\} \tag{5.7}$$

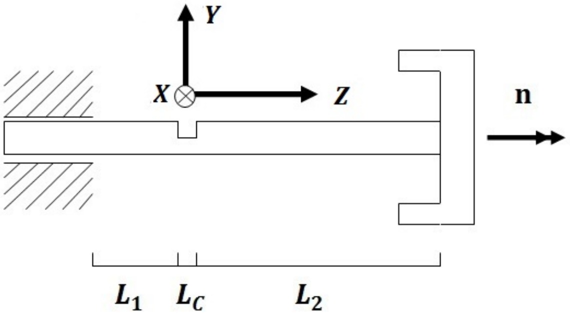

Figure 5.1: Overhung rotordynamic system displaying a notch crack

and

$$\left[[R]^T - \lambda_n [S]\right] \left\{\tilde{\psi}_n\right\} = \{0\}, \tag{5.8}$$

where ψ_j and $\tilde{\psi}_n$ are the right and left eigenvectors, respectively, and the eigenvalues obey $\lambda_j = \lambda_n$. Note that the damping matrix $[D]$ is neglected for the free response analysis, as the system damping is small. Solving either eigenvalue problem provides the full set of eigenvalues, which appear as complex conjugate pairs. Furthermore, the eigenvalues obtained from Eqs. 5.7 and 5.8 are the relative (rotating frame) eigenvalues of the system, and must be transformed to an inertial frame using Eq. 4.2.

5.2 Free Response: Notch Crack

An overhung rotordynamic system displaying a notch crack of width L_C is shown in Fig. 5.1. Reference frame XYZ is attached to a hypothetical undeflected shaft and rotates at shaft speed n. The response of the notched system depends on the stiffness reduction induced by the notch, which in turn depends on the notch's area moments of inertia. Closed-form expressions of the notch area moments of inertia are given in Appendix B as a function of crack depth.

Two scenarios are investigated; the first analyzes a system in which the notch's location is fixed, while the second investigates the influence of both notch location and depth. A fixed-location notch situation is assessed for two reasons. First, the results allow direct comparison to analytical and experimental results given by Green

Table 5.1: Test rig parameters

m	0.573 kg
I_t	2.37×10^{-4} kg $\cdot$ m^2
I_p	3.85×10^{-4} kg $\cdot$ m^2
E	207 GPa
L	88.9 mm
d	10.2 mm
ν	0.33

and Casey [1] and Varney and Green [2]. Second, the influence of notch depth can be examined independently from notch location.

5.2.1 Fixed-Location Notch

A notch 6.35 mm (0.25 inches) from the support is investigated to facilitate comparison to earlier work by Green and Casey, [1]. Parameters of the rotordynamic test rig discussed in Section 3.4 are employed in the analysis; these parameters are summarized in Table 5.1. To compensate for experimental uncertainty, the nominal length of the shaft is adjusted to equate the experimental [2, 37] and analytical first natural frequency of the undamaged shaft. The adjusted length of the shaft is found to be 86.4 mm (3.403 inches), which is less than a mere 2% of the actual shaft length.

Equation 5.7 is solved to find the eigenvalues of the notched system for a range of shaft speeds, whereas the Complex Transfer Matrix is used to provide the Campbell diagram (i.e., locus of inertial eigenvalues versus shaft speed) of the undamaged system. The 2X resonance frequency is extracted by locating the intersection between the locus of eigenvalues and a line of slope two, as shown in Figs5.2 - 5.5. Figure 5.2 provides the Campbell diagram of the undamaged rotordynamic system, while Figs. 5.3 - 5.5 give the Campbell diagram for notches of 20%, 40% and 60% depth, respectively. Regions of instability are indicated on the figures, along with the 1X excitation line (i.e., synchronous response). Instability occurs when the eigenvalue's real part is positive. As the notch depth is increased, it is clear that the width of the

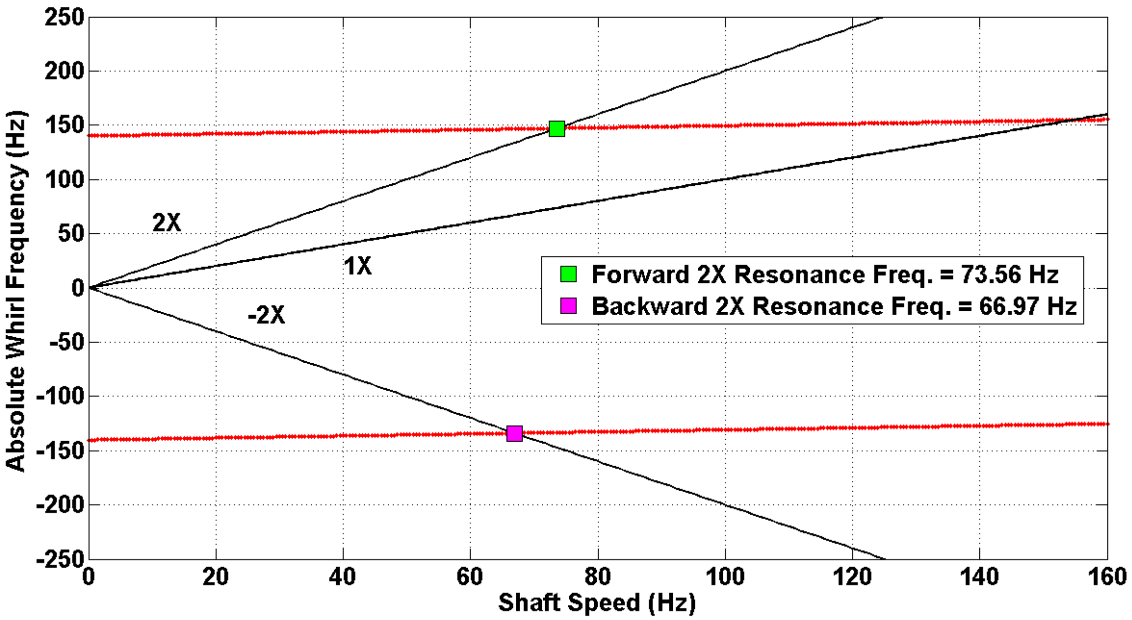

Figure 5.2: Campbell Diagram: Undamaged system (generated using Complex Transfer Matrix)

instability region increases.

The 2X resonance frequencies from a gaping fatigue crack model and a notch model are compared in Fig. 5.6 and Table 5.2. Figure 5.6 plots the 2X resonance frequency versus notch depth, and compares to experimental results (the experimental results are discussed shortly). Table 5.2 compares the analytic 2X resonance frequency for a range of notch depths to those found experimentally by Casey [37] and presented by Varney and Green [2]. As expected [1, 2], the 2X resonance frequency decreases with increasing notch depth, though the decrease is marginal until approximately 40% depth. Green and Casey [1] employ a gaping fatigue crack in their analytic work, though they experimentally manufacture a notch.

As expected, the results in Table 5.2 and Fig. 5.6 indicate that the experimental results align closer to the notch crack than the gaping fatigue crack (discussed in Section 5.3). From Fig. 5.6, it is also evident that the two models provide virtually identical results until approximately 20% depth. The models remain similar from

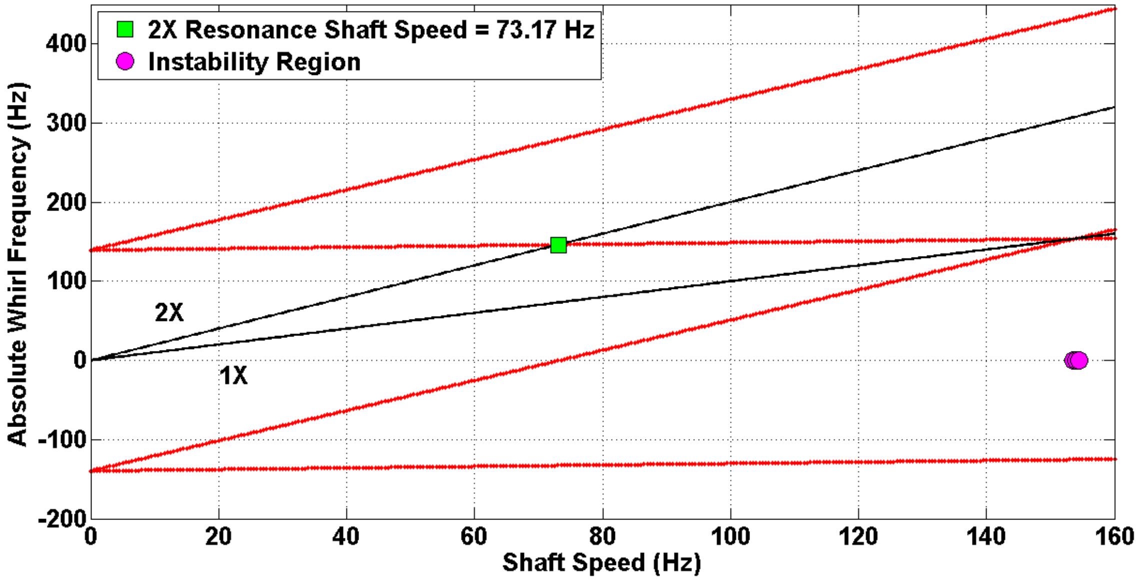

Figure 5.3: Campbell Diagram: Notch, 20% depth

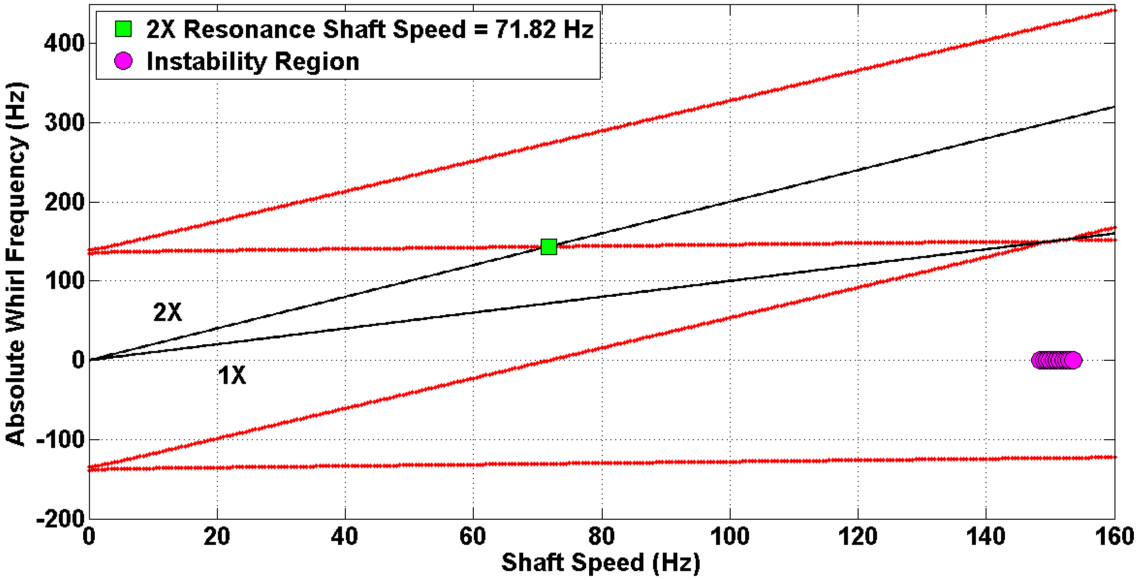

Figure 5.4: Campbell Diagram: Notch, 40% depth

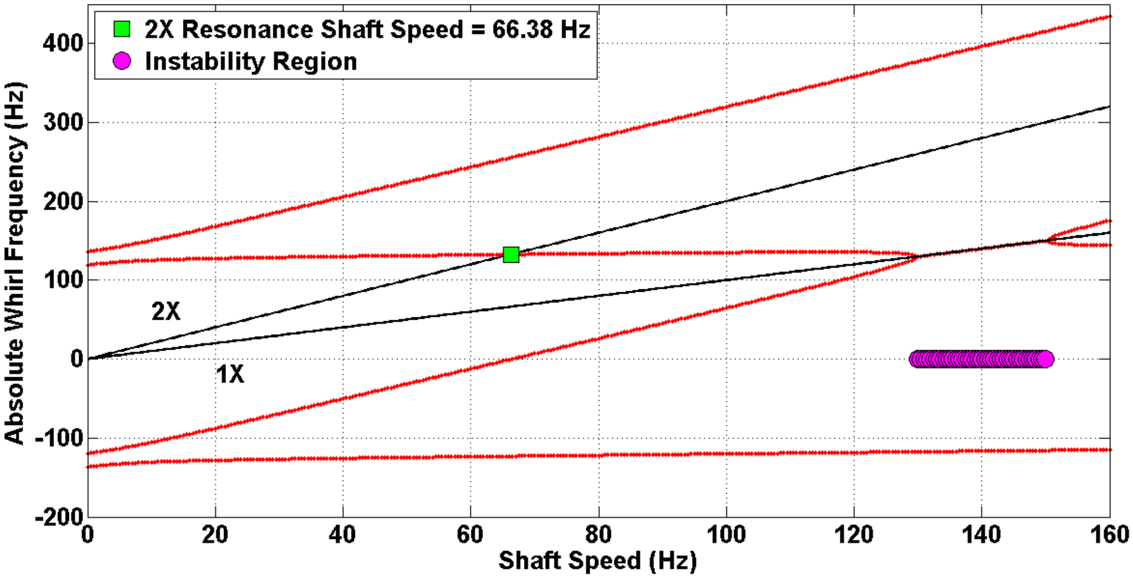

Figure 5.5: Campbell Diagram: Notch, 60% depth

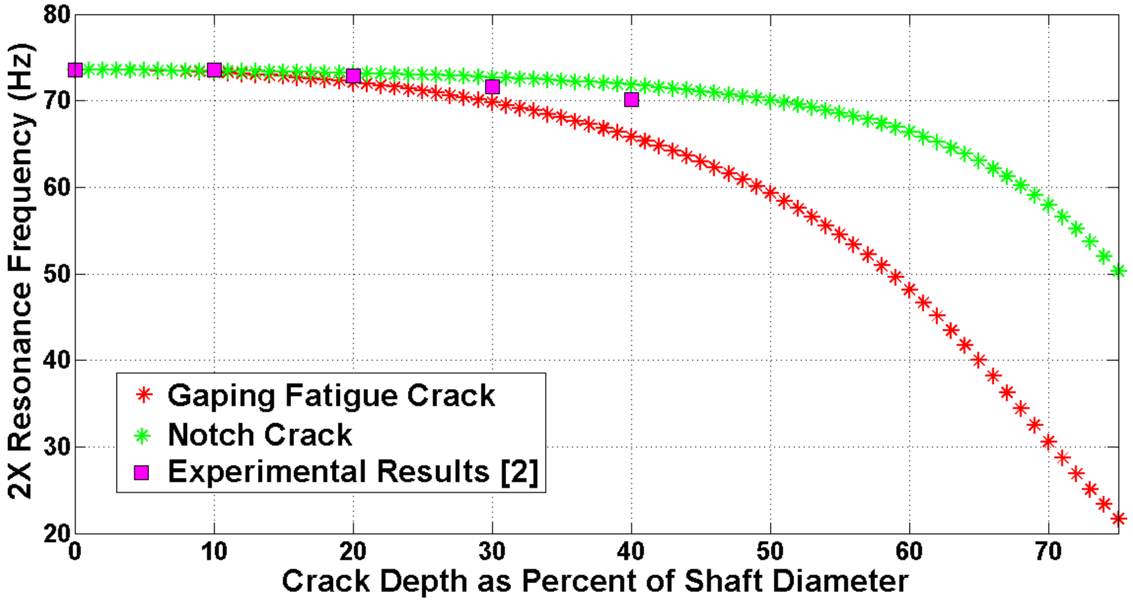

Figure 5.6: 2X resonance frequency versus crack depth for a fixed-location crack

Table 5.2: Analytic and experimental 2X resonance frequencies, along with percent difference from experimental results

% Crack Depth	Shaft Speed (Hz): Experimental [2, 37]	 Notch Crack	 Gaping Fatigue Crack
0	73.56	73.56 (0%)	73.56 (0%)
10	73.50	73.45 (-0.07%)	73.28 (-0.3%)
20	72.92	73.18 (0.4%)	72.12 (-1.1%)
30	71.67	72.70 (1.4%)	69.80 (-2.6%)
40	70.09	71.81 (2.5%)	65.83 (-6.1%)
50	–	70.07	59.29
60	–	66.37	48.18
70	–	57.91	30.68
75	–	50.30	21.75

20% to 40% depth, though the 2X resonance frequency for the gaping fatigue crack begins to decrease more pronouncedly. Beyond 40% depth, the models diverge significantly. The experimental results fall between those predicted by the two crack models, though significantly closer to the predicted notch results. The deviation indicates that the experimental crack contains an additional compliance not captured by the notch model. It is hypothesized that the additional compliance arises due to stress concentrations at the base of the notch.

5.2.2 Variable Notch Location

Investigating the influence of crack location on system response is a primary goal of this work. The 2X resonance frequency is found for a range of notch locations and depths by solving Eq. 5.7. Figures 5.7 and 5.8 provide the 2X resonance frequency versus notch depth and location. Figures 5.7b and 5.8b demonstrate the small variation in the 2X resonance frequency for cracks less than 35% of the shaft diameter. It is crucially important to recognize that different combinations of notch depth and location can result in the same 2X resonance frequency. Measurement of only the 2X resonance frequency is inadequate for diagnosing the notch parameters.

It is obvious from the flat regions of Figs. 5.7 and 5.8 that the limited variation

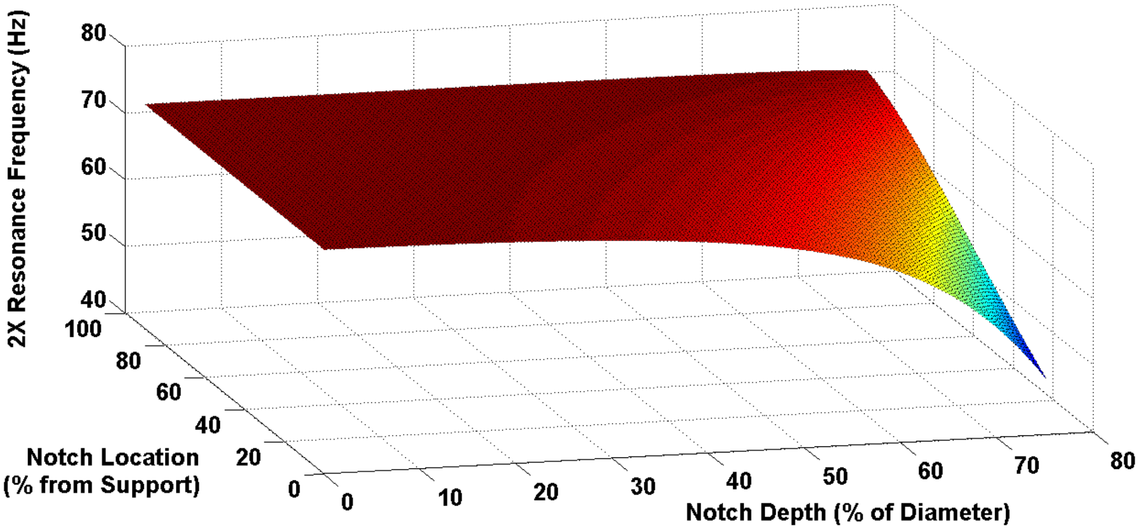

(a) Extended crack depth range: 0 - 80%

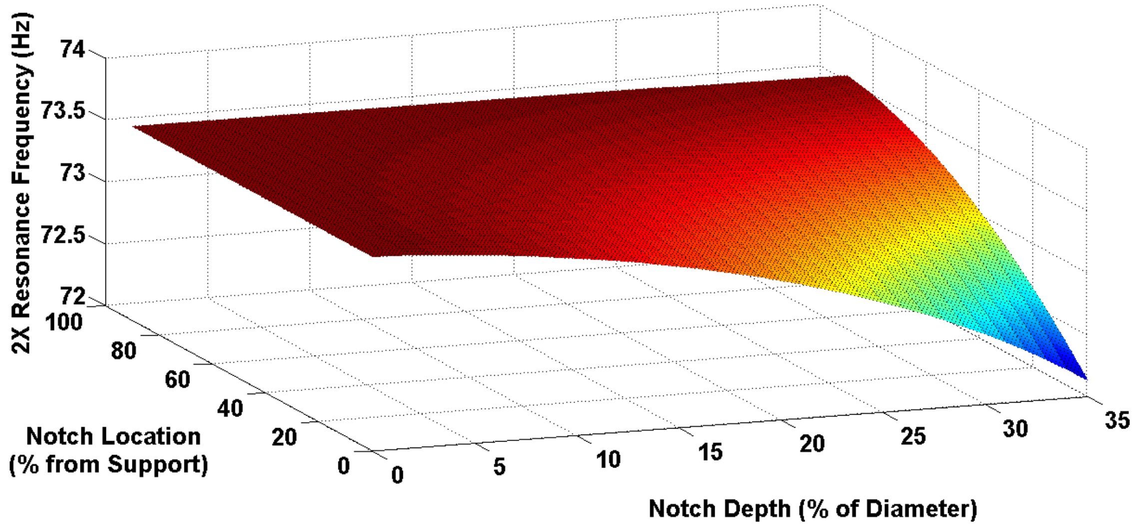

(b) Limited crack depth range: 0 - 35%

Figure 5.7: Notch Model: 2X resonance frequency versus notch depth and location

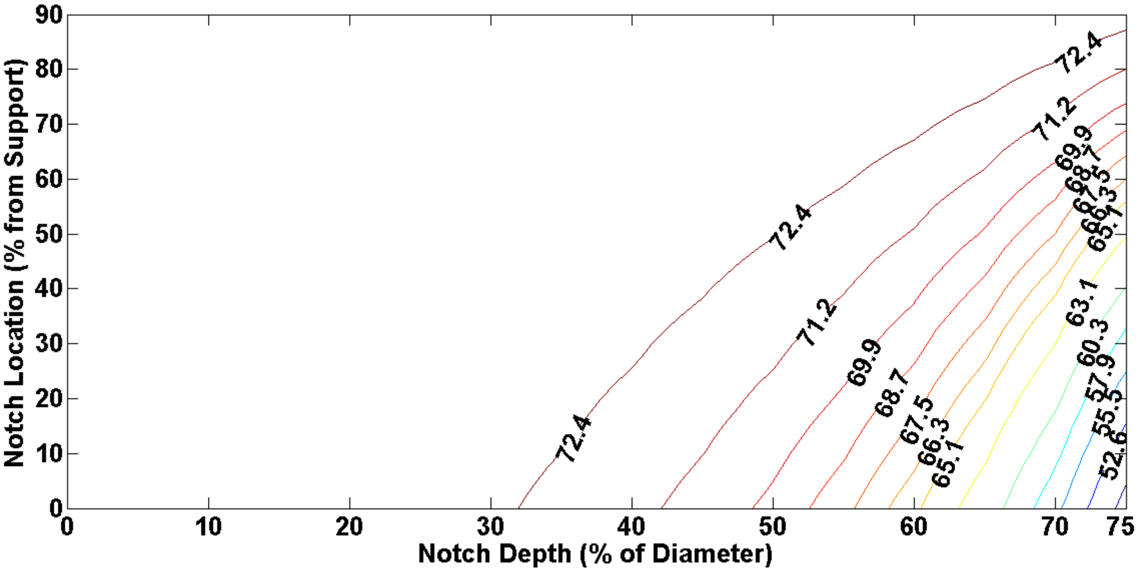

(a) Extended crack depth range: 0 - 75%

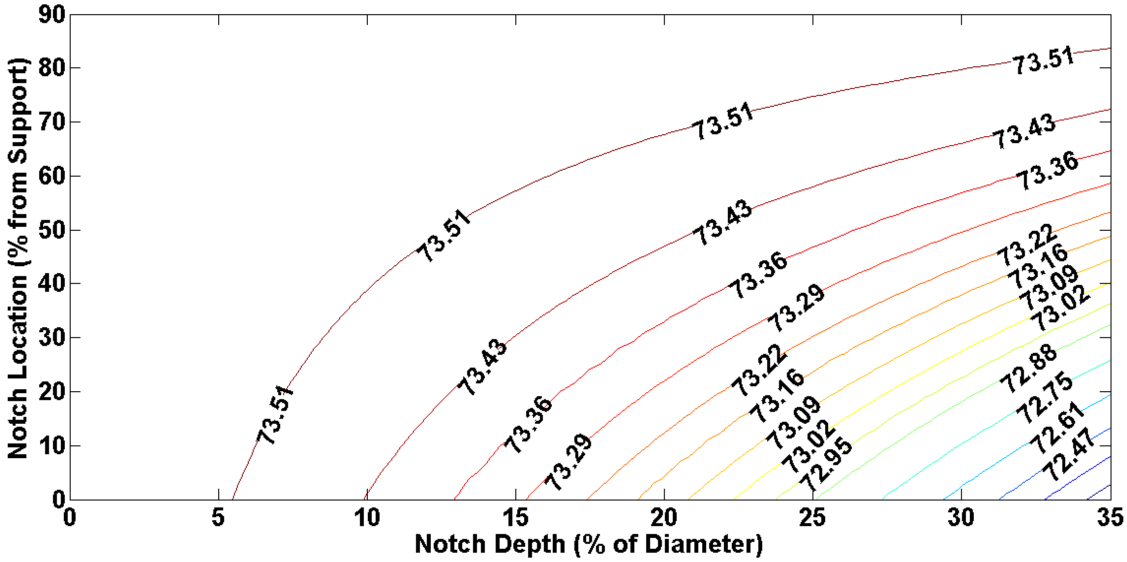

(b) Limited crack depth range: 0 - 35%

Figure 5.8: Notch Model: Contour plot of 2X resonance frequency versus notch depth and location (given in Hz)

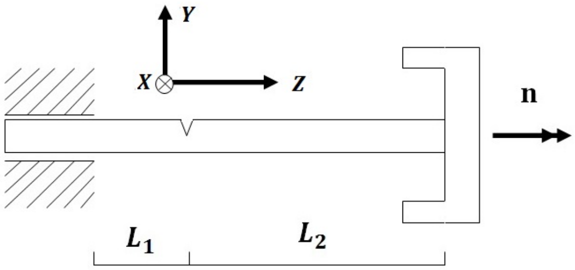

Figure 5.9: Overhung rotordynamic system displaying a gaping fatigue crack

in the 2X resonance frequency precludes crack detection for certain regions of notch depth and location (higher resolution is required to distinguish contours in these regions of Fig. 5.8a). Furthermore, even relatively deep notches (such as 40% of the diameter) can remain undetected if the notch is located far from the support. Additional aspects of the results relevant to condition monitoring are interpreted in detail in Chapter 7.

5.3 Free Response: Gaping Fatigue Crack

Recall that the gaping fatigue crack is a negligible-width crack terminating in a sharp edge. An overhung rotordynamic system displaying a gaping fatigue crack is shown in Fig. 5.9 with reference frame XYZ attached to a hypothetical undeflected shaft and rotating at the shaft speed n.

Results comparable to those provided for the notch crack are given for a gaping fatigue crack. First, a fixed-location gaping fatigue crack is investigated to isolate the effect of crack depth. Following presentation of these results, variations in both crack location and depth are investigated.

5.3.1 Fixed Location Gaping Fatigue Crack

The results for a fixed-location gaping fatigue crack 6.35 mm (0.25 inches) from the support are provided. Figures 5.10 - 5.12 give the Campbell diagrams for systems

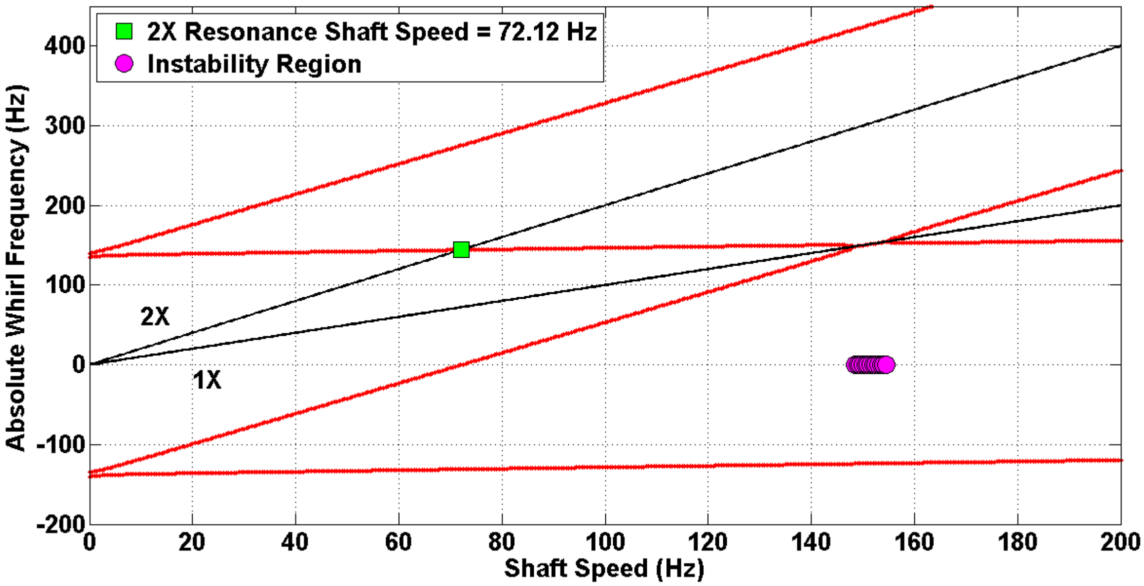

Figure 5.10: Gaping Fatigue Crack: 20% depth

displaying gaping fatigue cracks of 20%, 40%, and 60% depth, respectively. Intersection lines corresponding to 1X and 2X excitation are indicated in the figures, along with regions of instability. Just as with the notch, it is clear that the instability region widens as the crack depth increases. Additionally, a gaping fatigue crack results in an increased range of instability for commensurate crack depths, as evidenced by comparing Figs. 5.10 - 5.12 to Figs. 5.3 - 5.5.

The 2X resonance frequencies for crack depths of zero percent to 75% are plotted in Fig. 5.6 and provided in Table 5.2. It is obvious that the 2X resonance frequency for the gaping fatigue crack is more sensitive to changes in crack depth than the notch, as the 2X resonance frequency declines at a greater rate with increasing crack depth. The results indicate that a gaping fatigue crack results in a greater loss of stiffness than a notch crack of commensurate depth. In practice, a notch would therefore be more difficult to detect than a gaping fatigue crack of equal depth.

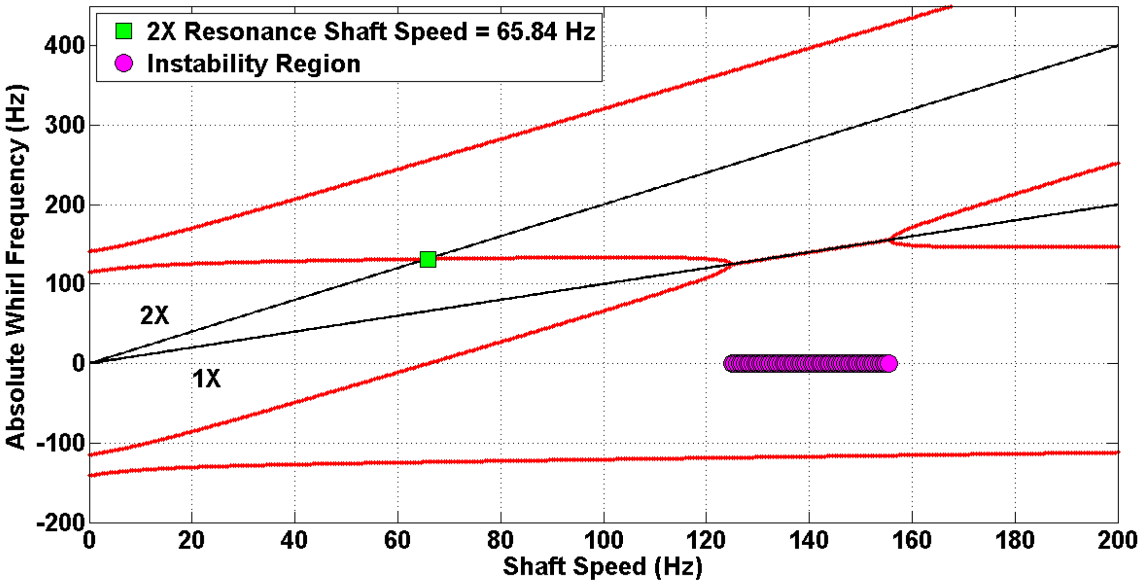

Figure 5.11: Gaping Fatigue Crack: 40% depth

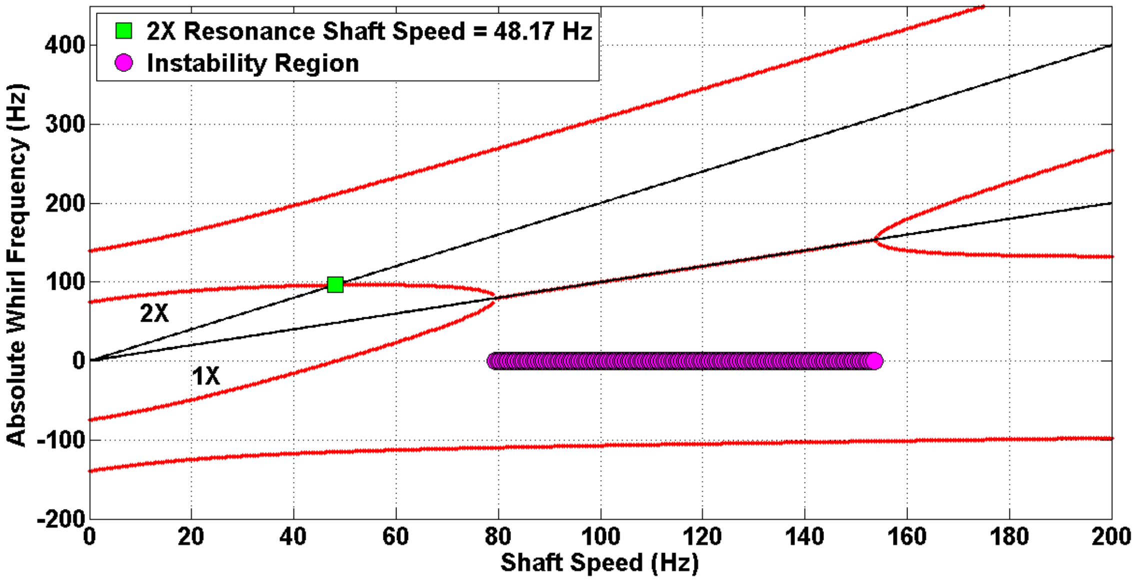

Figure 5.12: Gaping Fatigue Crack: 60% depth

5.3.2 Variable Gaping Fatigue Crack Location

The 2X resonance frequency is provided versus crack depth and location. Figures 5.13 and 5.14 give the 2X resonance frequency versus crack location and depth. Comparing Fig. 5.8 to Fig. 5.14 indicates that the 2X resonance frequency declines faster for a gaping fatigue crack than a notch. It is vital to note that different combinations of crack depth and location can result in the same 2X resonance frequency. Just as with the notch, knowledge of the 2X resonance frequency by itself is insufficient to diagnose the crack parameters. The 2X resonance frequency for the gaping fatigue crack is shown in Figs. 5.13b and 5.14b over a limited crack depth to show additional detail for shallow cracks. Just as with the notch, shallow cracks and cracks far from the support result in very little change in the 2X resonance frequency. The resolution of frequency measurements dictate the condition monitoring system's ability to detect small cracks.

5.4 Summary of Free Response Results

A free response analysis of the state space equations of motion is presented. Two cases are investigated for both crack models: varying the crack depth while fixing the crack location, and varying both the crack depth and location.

The free response techniques are applied to the fixed crack location system discussed by Green and Casey [1]. For the fixed crack location investigation, the Campbell diagrams of the system are obtained through solution of the eigenvalue problem. The 2X resonance frequencies are extracted and subsequently compared to those found analytically and experimentally by Casey [37] and Varney and Green [2]. The notch crack model better approximates the experimental results, which is unsurprising considering the manufactured crack resembles a notch crack more so than a gaping fatigue crack. It is hypothesized that additional unmodeled stress concentrations within the experimental notch result in slightly lower measured 2X resonance frequencies,

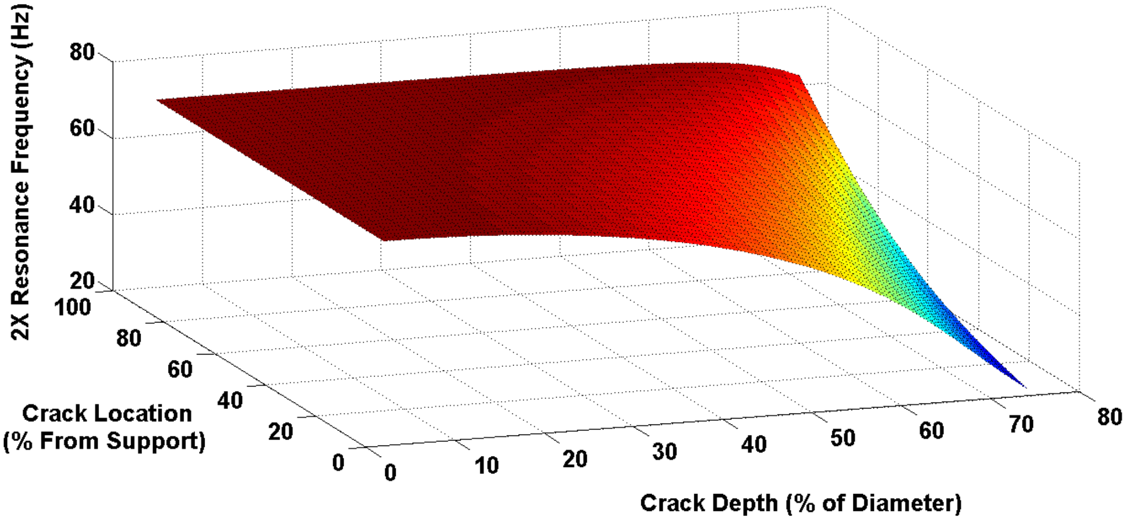

(a) Extended crack depth range: 0 - 80%

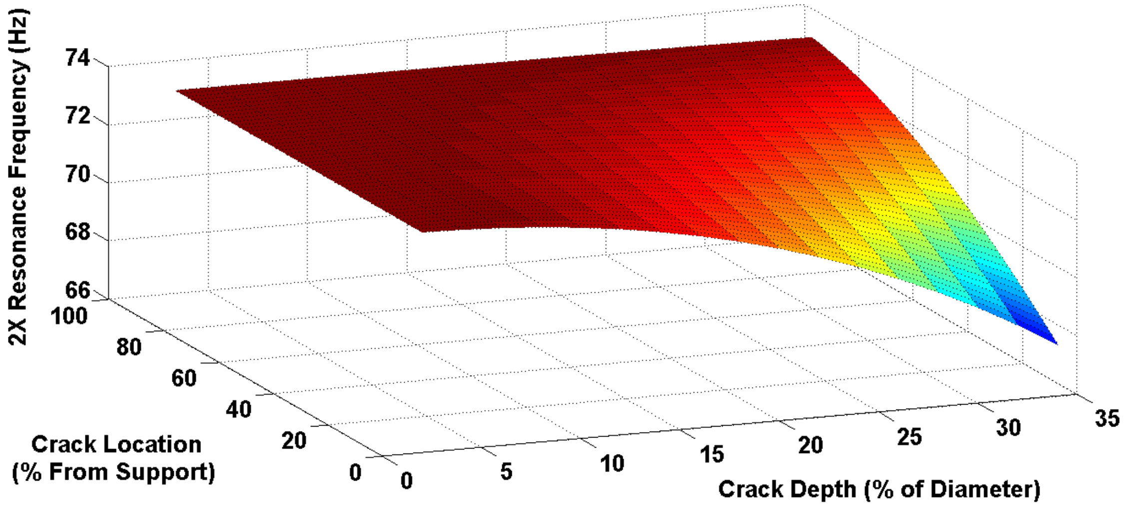

(b) Limited crack depth range: 0 - 35%

Figure 5.13: Gaping Fatigue Crack: 2X resonance frequency versus crack depth and location

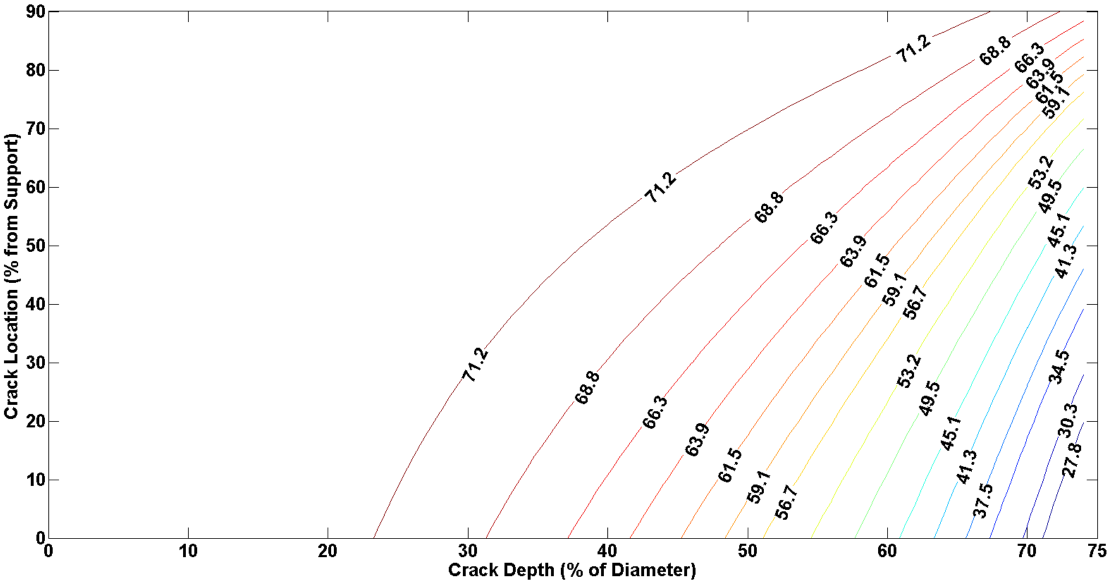

(a) Extended crack depth range: 0 - 75%

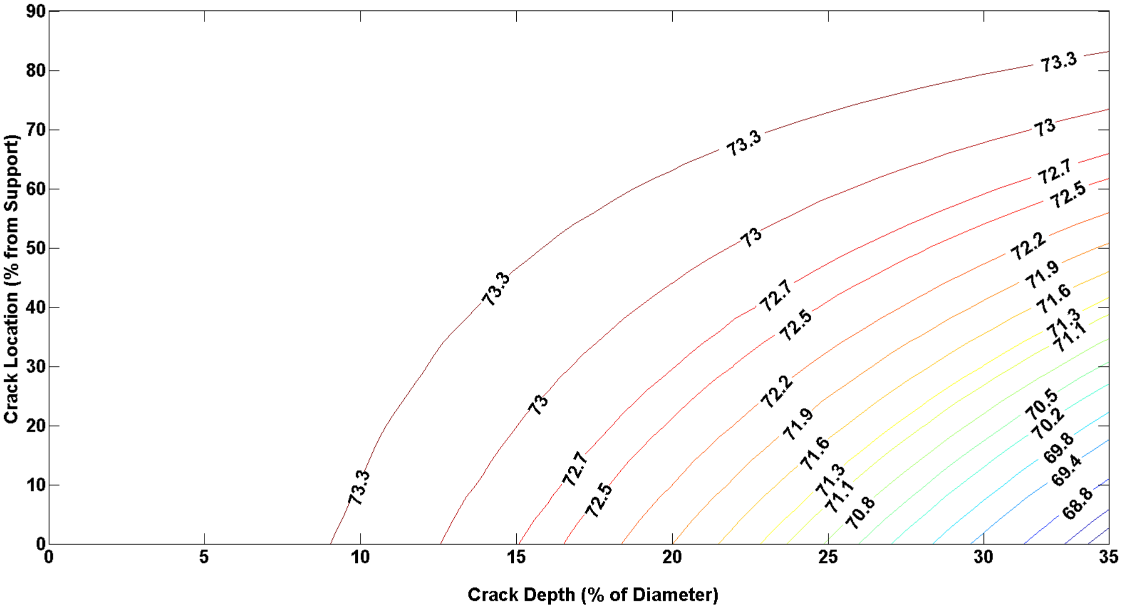

(b) Limited crack depth range: 0 - 35%

Figure 5.14: Gaping Fatigue Crack: Contour plot of 2X resonance frequency versus crack depth and location (given in Hz)

compared to those predicted by the notch model. The 2X resonance frequency is observed to decrease as crack depth increases for both models, which is reasonable considering deeper cracks result in a greater decrease in stiffness.

A free response analysis is performed in which both the crack depth and location are permitted to vary. The 2X resonance frequency is provided for both models as a function of crack location and depth. The results indicate that different combinations of crack depth and location can provide the same 2X resonance frequency. In comparing the crack models, it is once again found that the gaping fatigue crack model results in a more pronounced decrease in the 2X resonance frequency for increasing crack depth and locations nearer to the support.

CHAPTER VI

ANALYTIC RESULTS: FORCED RESPONSE

Vibration monitoring based diagnostics rely on measurement of the system's forced response. The forced response is particularly important for cracked rotordynamic systems, as the 2X harmonic appears only in the presence of forcing due to gravity (or any other constant radial load). Just as in Chapter 5, the forced response of both crack models is investigated for two scenarios. The first scenario involves a crack with fixed location, while the second allows the depth and location of the crack to vary.

A forcing function is developed including gravity and imbalance. The forced equations of motion are integrated numerically, and the frequency spectra of the transient and steady-state response is shown. The influence of imbalance on the cracked system response is investigated. The Complex Extended Transfer Matrix (CETM) is employed to extract the 2X component of the rotor's angular response. Specifically, the CETM is used to give three types of steady-state results: (1) the magnitude of the 2X resonant response versus crack depth and location, (2) orbital plots of the rotor's lateral and angular displacement, and (3) orbital mode shapes of the shaft's lateral and angular response.

Before results are presented, a method for decoupling the state space equations of motion is discussed. A transformation is given to relate the inertial frame response to the rotating frame response.

6.1 Obtaining the Forced Response

6.1.1 Decoupling the State Space Equations of Motion

The equations of motion are solved using the state space formulation in Section 5.1. Before the solution is given, the equations of motion are reduced to a system of eight decoupled single-degree-of-freedom equations. First, the eigenvalues and eigenvectors are found using the procedure in Section 5.1. The eigenvectors are normalized using the bi-orthogonality relations provided by Ginsberg [65]:

$$\{\Psi_j\} = \frac{\{\psi_j\}}{\left[\left\{\tilde{\psi}_j\right\}^T [S] \{\psi_j\}\right]^{1/2}} \tag{6.1}$$

$$\left\{\tilde{\Psi}_j\right\} = \frac{\left\{\tilde{\psi}_j\right\}}{\left[\left\{\tilde{\psi}_j\right\}^T [S] \{\psi_j\}\right]^{1/2}}. \tag{6.2}$$

The normalized left and right eigenvectors are then used to generate the following identities:

$$\left[\tilde{\Psi}\right]^T [S] [\Psi] = [I] \tag{6.3}$$

$$\left[\tilde{\Psi}\right]^T [R] [\Psi] = [\lambda], \tag{6.4}$$

where the modal matrices $[\Psi]$ and $[\tilde{\Psi}]$ decouple $[S]$ and $[R]$ into the identity matrix $[I]$ and a diagonal matrix of eigenvalues $[\lambda]$. Application of the coordinate transformation

$$\{x\} = [\Psi] \{\xi\} \tag{6.5}$$

to Eq. 5.4 results in a system of decoupled single degree of freedom equations of motion:

$$\left\{\ddot{\xi}\right\} - [\lambda] \{\xi\} = \left[\tilde{\Psi}\right]^T \left\{ \begin{array}{c} \{0\} \\ \{F\} \end{array} \right\}. \tag{6.6}$$

The elements of $\{\xi\}$ are the modal coordinates of the decoupled system, and $\{F\}$ is a vector of forcing functions. Upon solution of Eq. 6.6, the results are transformed back into the physical coordinate domain through application of Eq. 6.5.

6.1.2 Transformation from Rotating Frame to Inertial Frame

Equation 6.6 represents the single degree of freedom, decoupled equations of motion expressed in a rotating reference frame. A rotating reference frame is judicious for

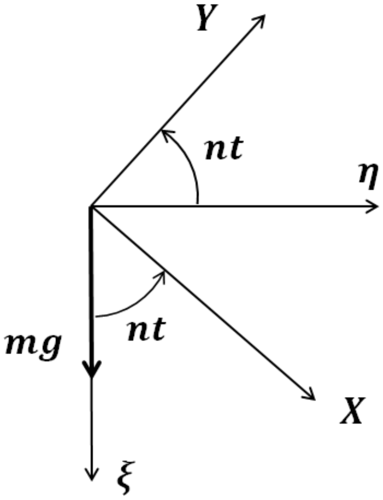

Figure 6.1: Relation between inertial and rotating reference frames, with gravity shown

the analysis, as the stiffness of the cracked shaft is constant in a rotating frame. However, most condition monitoring systems measure the inertial forced response of the system. Figure 6.1 shows the relationship between the inertial ($\xi\eta\zeta$) and rotating (XYZ) reference frames. To obtain the inertial response, the rotating frame coordinates are transformed into the inertial frame according to

$$\begin{Bmatrix} u_\xi \\ u_\eta \\ \gamma_\xi \\ \gamma_\eta \end{Bmatrix} = \begin{bmatrix} \cos(nt) & -\sin(nt) & 0 & 0 \\ \sin(nt) & \cos(nt) & 0 & 0 \\ 0 & 0 & \cos(nt) & -\sin(nt) \\ 0 & 0 & \sin(nt) & \cos(nt) \end{bmatrix} \begin{Bmatrix} u_X \\ u_Y \\ \gamma_X \\ \gamma_Y \end{Bmatrix}, \tag{6.7}$$

where the subscript on the generalized coordinates indicates the corresponding axis.

6.1.3 Forcing Functions

Forcing due to gravity in a rotating frame can be modeled as a complex exponential rotating in a direction counter to the shaft speed n:

$$F_g = mg\, e^{-int}, \tag{6.8}$$

where m is the mass of the rotor and g is the acceleration due to gravity. Expanding Eq. 6.8 into components in the rotating XYZ frame gives

$$\{F_g\} = \left\{ \begin{array}{c} mg\,\cos{(nt)} \\ -mg\,\sin{(nt)} \\ 0 \\ 0 \end{array} \right\}. \tag{6.9}$$

These terms can be visualized intuitively through examination of Fig. 6.1.

An additional source of excitation common in most rotordynamic systems is rotating imbalance. Figure 6.2 demonstrates an imbalance of mass m_e on the rotor, which is oriented a constant angle θ from the body-fixed x axis. The imbalance mass lies a constant radial distance ϵ from the rotor's geometric center, C. Fully accounting for the dynamic effects of the rotating imbalance requires recalculating the acceleration of the rotor's center of mass (see Appendix A for details). In addition, the angular momentum of the rotor is found by assuming that the vector $\bar{r}_{G/C}$, which locates the rotor's center of mass, is zero. For the purposes of this work, the influence of imbalance is qualitatively accounted for through the following forcing function:

$$\{F_I\} = \left\{ \begin{array}{c} m_e \epsilon n^2 \cos\theta \\ m_e \epsilon n^2 \sin\theta \\ 0 \\ 0 \end{array} \right\}. \tag{6.10}$$

In fact, it can be shown that the terms in Eq. 6.10 constitute a major component of the actual imbalance excitation. The imbalance influences the angular degrees of freedom by coupling the tilt of the rotor to the acceleration of its center of mass. However, as Lee and Green [8] demonstrate, these nonlinear coupling effects are of second order and can be neglected. As will be seen, the primary effect of the rotating imbalance is to introduce a 1X shaft speed harmonic into the inertial frame response.

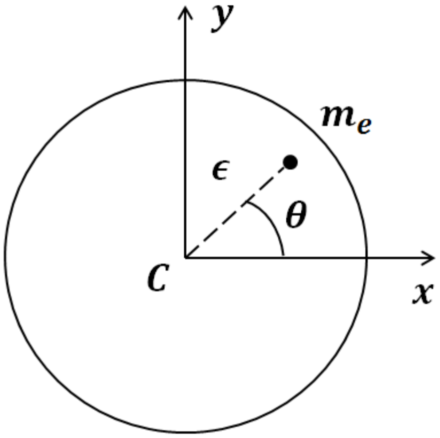

Figure 6.2: Rotating imbalance on the rotor

The total forcing $\{F\}$ is then a sum of the contributions from gravity and imbalance:

$$\{F\} = \begin{Bmatrix} mg\,\cos(nt) + m_e \epsilon n^2 \cos\theta \\ mg\,\sin(nt) + m_e \epsilon n^2 \sin\theta \\ 0 \\ 0 \end{Bmatrix}. \tag{6.11}$$

Since the system is linear, the solution to the problem is a superposition of the response to imbalance and the response to gravity. As the gaping crack under the influence of gravity solely generates a 2X harmonic in steady-state, while imbalance generates only a 1X harmonic, it is hypothesized that the presence of imbalance does not influence the 2X harmonic. This hypothesis is investigated in the following analysis.

The solution to the forced equations of motion for both crack models is presented herein. The state space equations of motion in Eq. 6.6 are solved numerically using a 4th order Runge-Kutta routine. Numerical solution of the equations is sought for two primary reasons: (1) the complexity of the equations, and (2) the robustness of the method to quickly account for varying initial conditions and compliance matrices. A time step is chosen in the solution such that sufficient resolution is achieved in the

2X component of the steady-state response. The Complex Extended Transfer Matrix is then employed to expediently extract the steady-state 2X component of the rotor's response.

Once again, two scenarios are investigated: the first provides the response of a rotordynamic system with a fixed crack location at 6.35 mm (0.25 inches) from the support, and the second investigates the interplay between crack location and depth.

6.2 Notch Crack

6.2.1 Fixed Notch Location

The forced equations of motion (see Eqs. 3.3 and 3.9) with a notch located 6.35 mm (0.25 inches) from the support are solved for several notch depths. Additional model parameters are found in Section 3.4. Results are presented in the rotating and inertial reference frames. Small initial conditions (10^{-4} m for u_X and u_Y, and 10^{-4} rad for γ_X and γ_X) are provided such that the transient response of the rotor exposes free response characteristics. The steady-state response is found by allowing the transient component of the response to decay. The steady-state response is therefore uninfluenced by the specific choice of initial conditions. However, different initial conditions would result in different magnitudes of transient components.

First, the frequency spectra of the gravity-forced response of γ_X is provided for an undamaged system. Only the response of γ_X and γ_ξ is shown, though the other degrees of freedom exhibit similar behavior. Figure 6.3a displays the response spectra of γ_Y in a rotating reference frame, while Fig. 6.3b provides the response spectra of γ_ξ in the inertial frame. Peaks located at the eigenvalues of the system are seen in the figures, along with the appearance (or lack thereof) of 1X and 2X harmonic components. Inclusion of the transient response exposes the appearance of response peaks at the system eigenvalues.

A 1X harmonic response component exists in the rotating frame frequency spectra

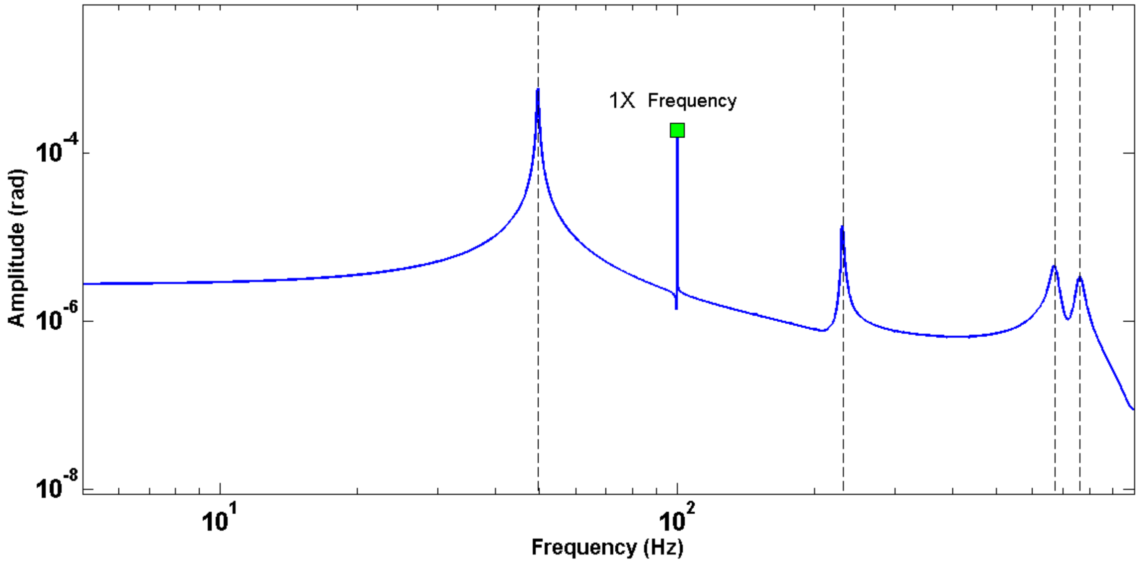

(a) Rotating frame: γ_X

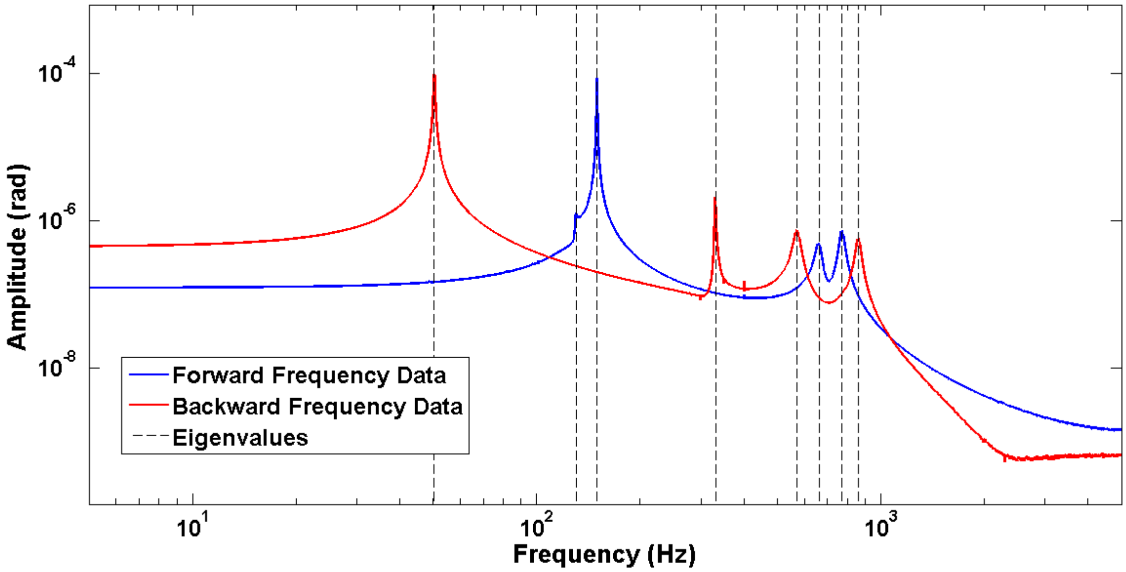

(b) Inertial frame: γ_ξ

Figure 6.3: Transient gravity-forced response of γ_X and γ_ξ for an undamaged system with a shaft speed of 100 Hz

for the undamaged system. Rotating frame analysis gives a frequency spectra which is relative to the shaft speed, according to Eq. 4.2. Therefore, the 2X frequency appears as a 1X frequency in the rotating frame frequency domain. Intuition would suggest that this 1X frequency should vanish in an undamaged system. However, static deflection due to gravity in the inertial frame response appears as a 1X frequency component in the rotating frame, just as forcing due to gravity is a vector rotating at the shaft speed in a rotating reference frame. A 1X harmonic frequency is thus present in the rotating frame response even in the absence of a crack. Removal of gravity results in a disappearance of the rotating frame 1X component. As expected, transformation of the response from a rotating to inertial frame does not result in a 2X frequency for an undamaged system.

A notch of depth 40% of the diameter and located 6.35 mm from the support is investigated next. The frequency spectra of the transient response of γ_X is provided in Fig. 6.4a, while Fig. 6.4b gives the same for the inertial response γ_ξ. The shaft speed is chosen to be 100 Hz so that it is sufficiently removed from resonance. Rotating imbalance of magnitude $m_e\epsilon = 5(10)^{-6}$ kg m is included at an orientation of $\theta = 0$ rad. The eigenvalues are indicated in the figure by vertical lines, along with the 1X and 2X shaft speed harmonics. As expected, the rotating frame response displays only a 1X harmonic, while the inertial response prominently contains both 1X and 2X harmonics. For verification, in the absence of either a notch or gravity, the 2X harmonic component fails to appear. Likewise, the magnitude of the 2X harmonic is not influenced by imbalance; this result is expected due to the linearity of the system. Comparing Figs. 6.4 and 6.3 shows that the crack excited both forward and backward frequency components. Additionally, the inertial frame response possesses an increased richness of the response as compared to the undamaged system, though a discussion of such characteristics is not relevant to this work.

The steady-state response is obtained by extracting the response following the

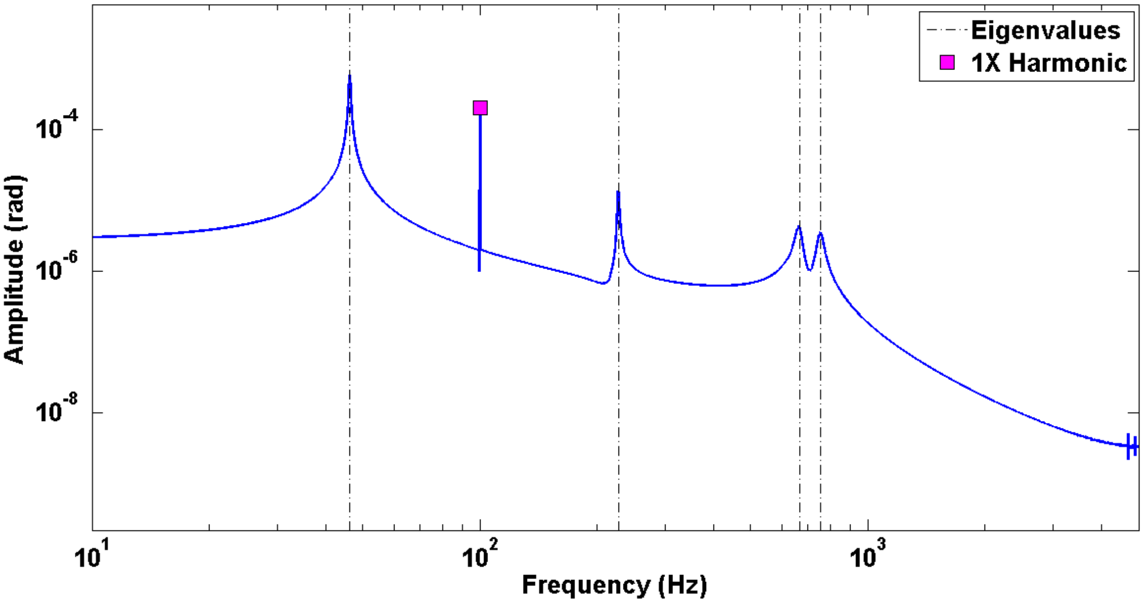

(a) Rotating frame: γ_X

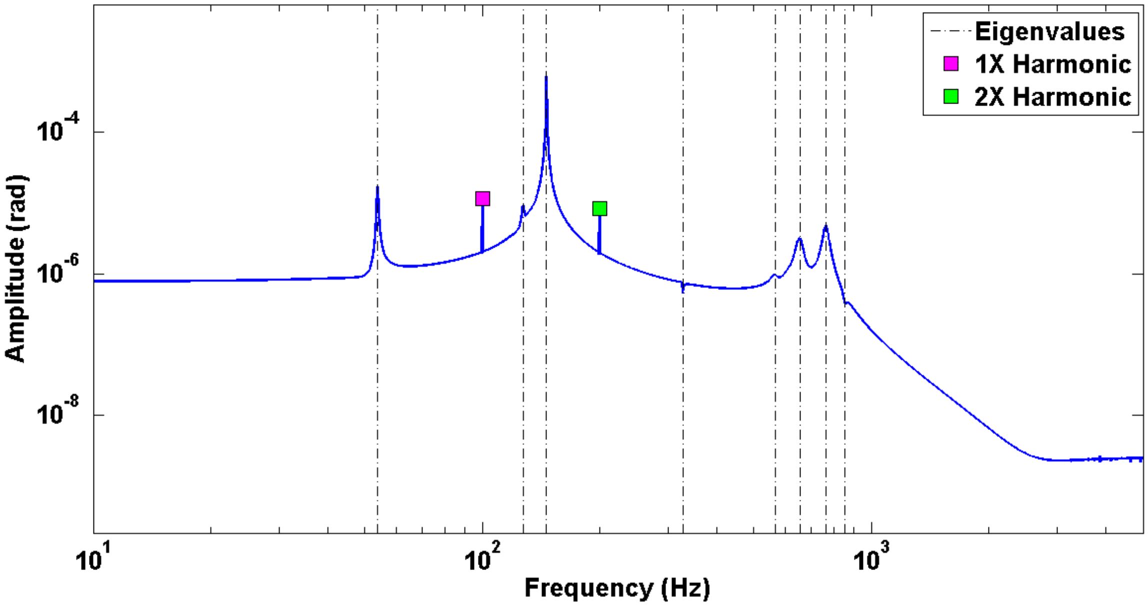

(b) Inertial frame: γ_ξ

Figure 6.4: Notch Crack: Transient response of γ_X and γ_ξ for a fixed location notch of 40% depth: n = 100 Hz, $m_e\epsilon = 5(10)^{-6}$ kg m

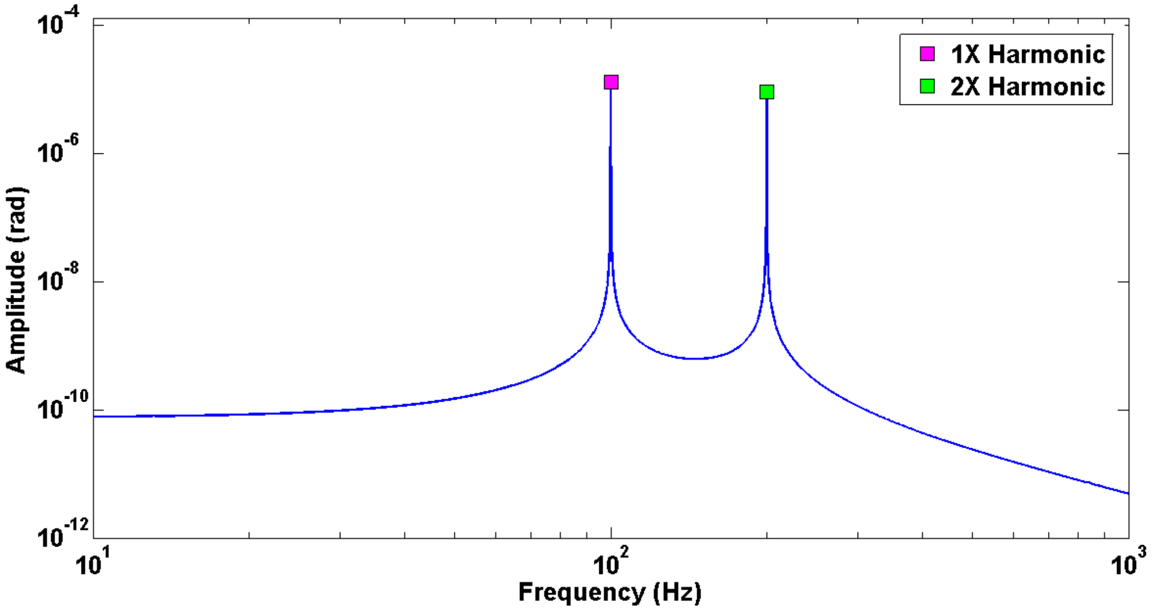

Figure 6.5: Notch Crack: Steady-state response of γ_ξ for a fixed location notch of depth 40%

decay of the transients. Figure 6.5 demonstrates the steady-state response of the inertial coordinate γ_ξ for the notch system discussed above. The steady-state response clearly contains two components: a 1X harmonic due to imbalance, and a 2X harmonic generated by a combination of the notch and forcing due to gravity. The presence of imbalance does not influence the magnitude of the 2X harmonic, as seen by the linearity of the system. Therefore, in the analyses that follow, imbalance is omitted for clarity in presenting the 2X harmonic.

Figures 6.6a and 6.6b provide the inertial gravity-forced transient response for a range of shaft speeds. Once again, a notch of 40% depth located 6.35 mm (0.25 inches) from the support is investigated. The transient response is displayed to emphasize that the 2X resonance occurs when the 2X harmonic coincides with a natural frequency of the system. Figure 6.6a presents a shaft speed range of 95 to 105 Hz, thus placing the 2X harmonic above the 2X resonant shaft speed of 71.81 Hz (see Table 5.2). The magnitude of the 2X harmonic is relatively small when the shaft

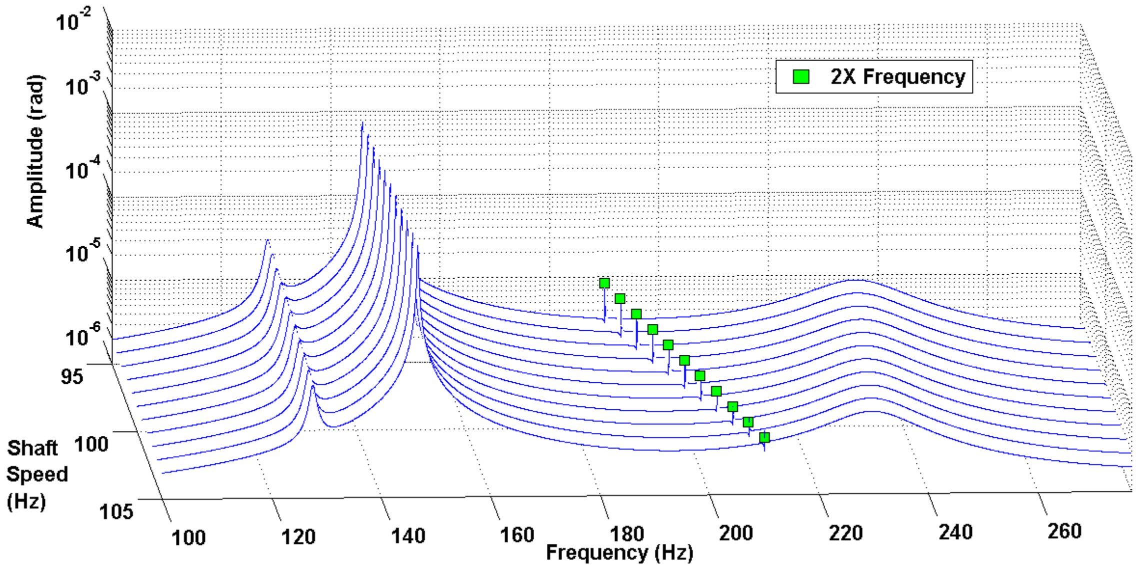

(a) Shaft speed above the 2X resonant shaft speed

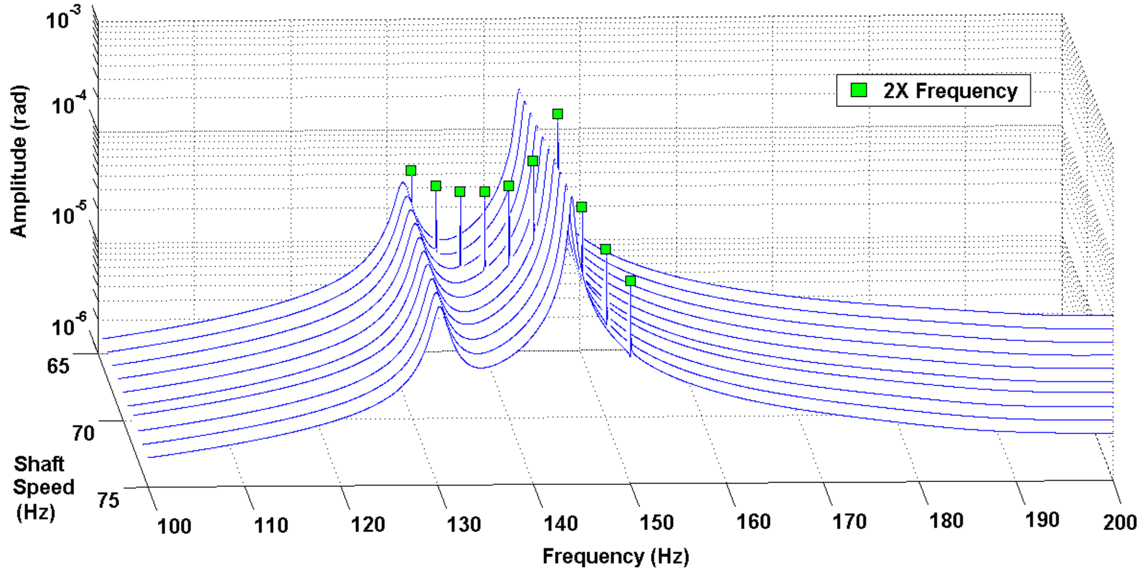

(b) Shaft speed near the 2X resonant shaft speed

Figure 6.6: Notch Crack: Inertial frame gravity-forced response of γ_ξ for a notch of 40% depth, located 6.35 mm from the support

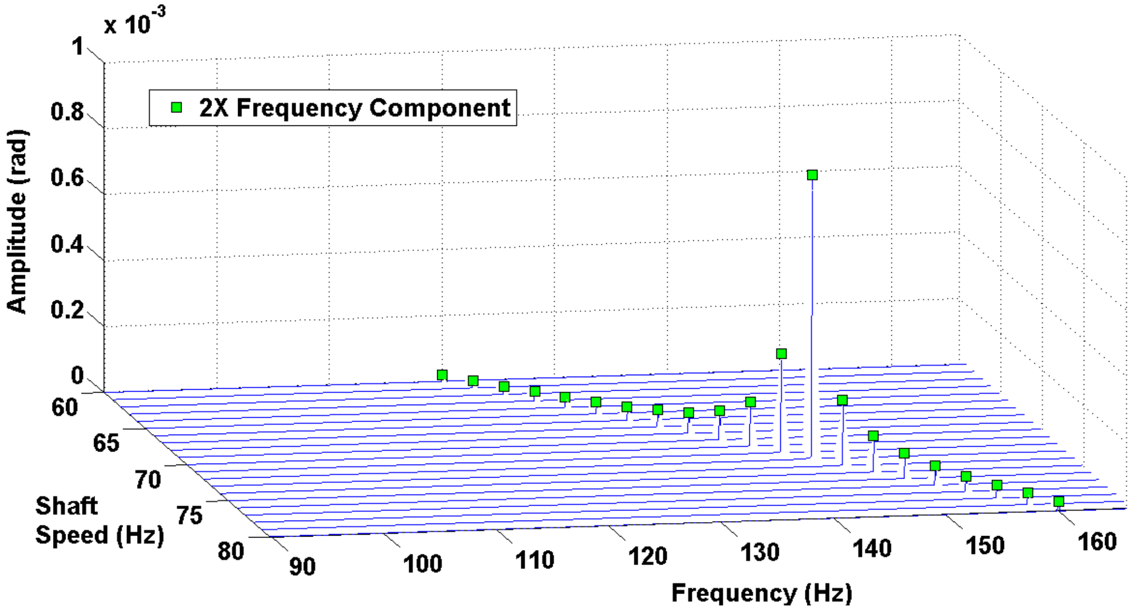

Figure 6.7: Notch Crack: Steady-state response of γ_ξ for a shaft speed range encompassing resonance

speed is far from the 2X resonant shaft speed. Figure 6.6b presents a shaft speed range of 66 to 75 Hz, which encompasses the 2X resonant shaft speed. As the shaft speed nears the 2X resonant frequency, the magnitude of the 2X harmonic increases considerably. The magnitude of the 2X harmonic near resonance and far from resonance is important for crack detection and diagnosis, as will be discussed in Chapter 7.

The steady-state response of a fixed-location notch of 40% depth is found over a range of shaft speeds. A shaft speed range encompassing resonance is investigated. Just as in Fig. 6.7, the magnitude of the 2X harmonic increases considerably as the shaft speed nears the 2X resonant frequency. Away from resonance, the magnitude of the 2X harmonic pronouncedly decreases. Interestingly, the same resonance peak is observed even when backward whirl is investigated (i.e., switching the sign of the gyroscopic terms in matrix $[G]$).

The steady-state response can be directly extracted using the 9×9 Complex Extended Transfer Matrix technique discussed in Section 4.4. The advantage of the CETM method over the equations of motion is that the steady state response is calculated directly, thus allowing for significantly decreased computational effort. Green and Casey [1] provide an expression for extracting the 2X harmonic component of the total angular response γ of the rotor (i.e., the rotor tilt) in an inertial frame:

$$\gamma = \frac{1}{2}\left[(\gamma_{X_r} - i\gamma_{X_i} + i\gamma_{Y_r} + \gamma_{Y_i}) + (\gamma_{X_r} + i\gamma_{X_i} + i\gamma_{Y_r} - \gamma_{Y_i})\, e^{i\,2nt}\right], \tag{6.12}$$

where the subscript indicates the direction of the quantity and whether the quantity is real ('r') or imaginary ('i'). The rotor tilt γ thus executes a circular orbit of radius $\frac{1}{2}|\gamma_{X_r} + i\gamma_{X_i} + i\gamma_{Y_r} - \gamma_{Y_i}|$, offset by the vector quantity $\frac{1}{2}(\gamma_{X_r} - i\gamma_{X_i} + i\gamma_{Y_r} + \gamma_{Y_i})$. The magnitude of the 2X harmonic component (i.e., the radius of the 2X orbit) of the angular response of the rotor is found as a function of shaft speed and notch depth. An analogous procedure gives the the lateral displacement of the rotor:

$$u = \frac{1}{2}\left[(u_{X_r} - iu_{X_i} + iu_{Y_r} + u_{Y_i}) + (u_{X_r} + iu_{X_i} + iu_{Y_r} - u_{Y_i})\, e^{i\,2nt}\right]. \tag{6.13}$$

Figures 6.8 and 6.9 display the 2X angular response of the rotor versus shaft speed and notch depth. Figure 6.9 provides a color-map visualization for clarity, where the warmer colors represent a larger angular resonant magnitude. The color-map is provided to better demonstrate qualitative trends in the profile of the 2X harmonic: as notch depth increases, the 2X resonance frequency decreases while the magnitude of the rotor's resonant 2X angular response increases. The 2X harmonic reaches resonance as the shaft speed nears one-half of the first natural frequency. The magnitude of the 2X resonant peak of the angular response increases as notch depth increases, accompanied by a decrease in the 2X resonant frequency.

Several trends are evident in the forced response of the fixed-location notch. First, as intuition suggests, the 2X resonant response of the rotor tilt increases as notch depth increases. Second, as indicated by the previous free response analysis and the

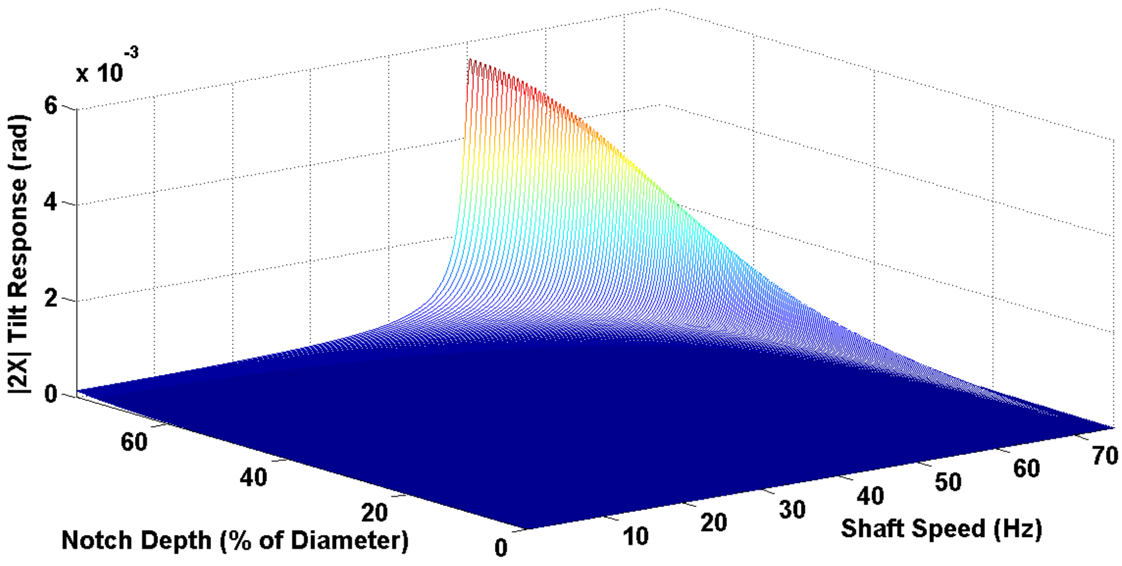

Figure 6.8: Notch Crack: Magnitude of 2X tilt response for a notch 6.35 mm from the support

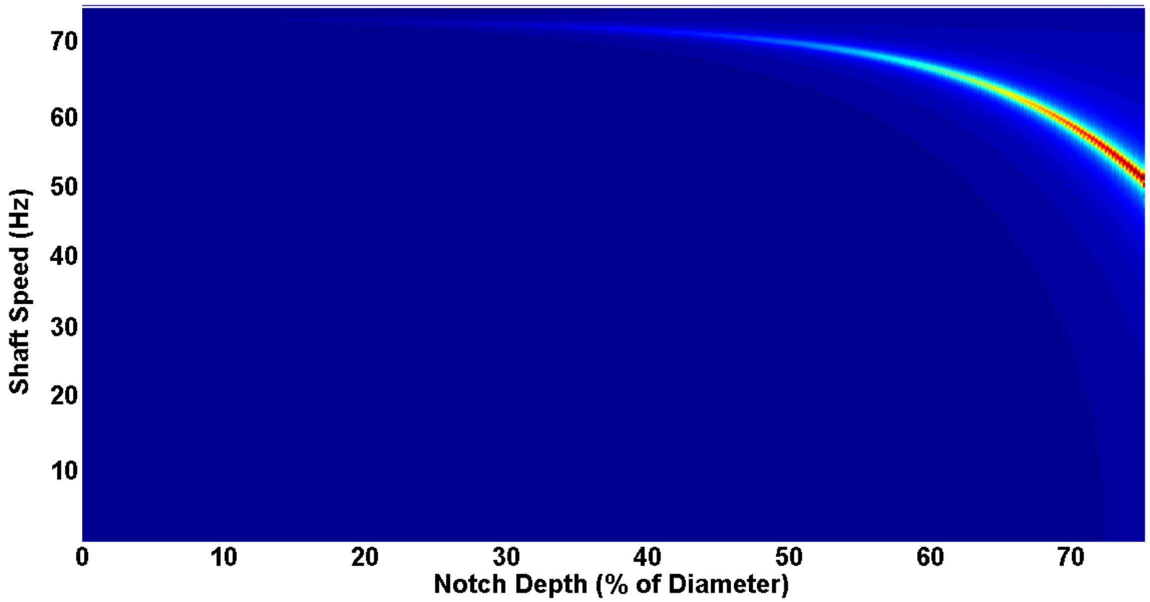

Figure 6.9: Notch Crack: Color-map representation of 2X tilt response for a notch 6.35 mm from the support

current analysis, the 2X resonant frequency decreases as the notch increases in depth. These results are interpreted further in Chapter 7 in relation to crack detection and diagnostics.

6.2.2 Variable Notch Location

The Complex Extended Transfer Matrix technique is used to investigate the 2X component of the rotor's response for a range of notch depths and locations. Specifically, Eq. 6.12 gives an expedient method for providing the steady-state magnitude of the rotor's angular and lateral response. The magnitude of the angular 2X resonant peak is investigated versus notch depth and location. Orbits of the rotor's center are given for several notch depth and location pairs yielding the same 2X resonant frequency. Lastly, orbital profiles of the shaft response are provided for these same notch depth and location pairs.

The magnitude of the 2X resonance of the rotor's angular response is given in radians versus notch depth and location in Fig. 6.10. Figure 6.10 demonstrates that as notch depth increases and location decreases, the magnitude of the 2X resonance increases. This result is expected, considering Fig. 6.8, where for a single notch location the resonance frequency decreases with increasing magnitude as the stiffness of the system decreases. The leftmost region of the figure has a low density of contours, indicating that notch detection and diagnosis in this regime is dictated by model accuracy and monitoring equipment resolution.

The steady-state inertial angular orbit of the rotor is found by plotting γ_ξ versus γ_η. Likewise, the lateral displacement orbit is obtained by plotting u_ξ versus u_η. At steady-state, in the absence of imbalance, the response consists only of the 2X harmonic component. The orbit's shape, as well as the offset and radius, can serve as important detection and diagnostic tools [2, 10, 13, 37]. Figures 6.11, 6.12, and 6.13 give the rotor's angular and lateral orbits for shaft speeds below resonance (50 Hz), at

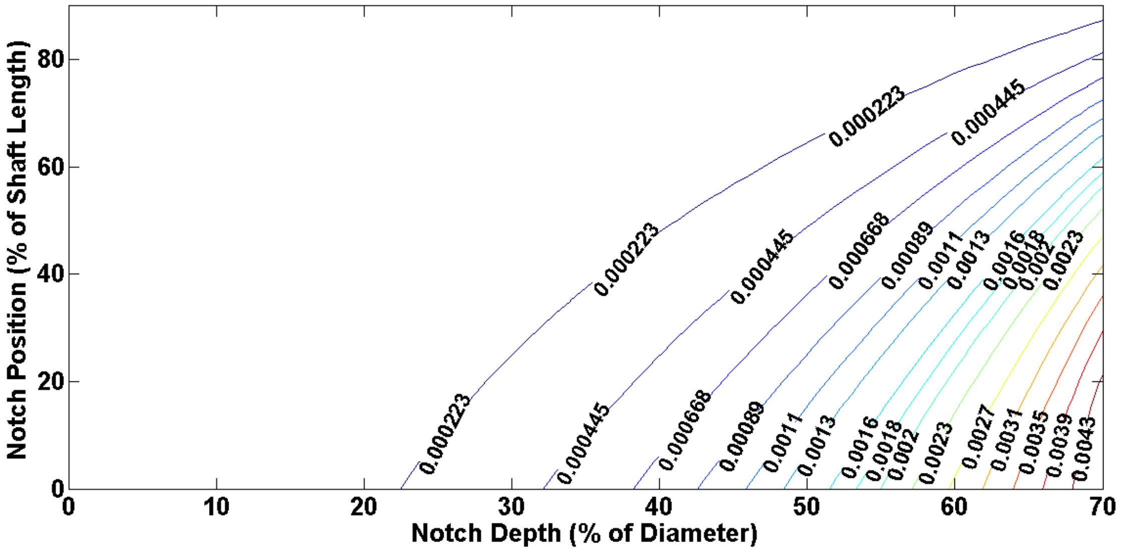

Figure 6.10: Notch Crack: Magnitude (in radians) of 2X component of resonant angular response versus notch location and depth

resonance (72 Hz), and above resonance (100 Hz), respectively. Three combinations of notch depth and location are shown in each figure; these pairs of notch depth and location yield the same 2X resonant frequency (72 Hz).

Prior to discussing the orbits, it is imperative to note that the orbital shapes depend entirely on the unique system at hand. Few trends can be extrapolated to have meaning for different rotordynamic systems (such as a simply supported Jeffcott rotor, for example). However, observing the orbital shapes for a system in which a specific model is known can provide meaningful and conclusive diagnostic information.

The 2X orbits shown in the figures are circular, as corroborated by Rao [19], Bachschmid [51], and Papadopoulos [15]. The circular shape arises because in the inertial response, for example, the coordinate γ_ξ is phase shifted from γ_η by $\pi/2$, while having the same peak-to peak amplitude. Additionally, averaging the inertial frame stiffness matrix over one revolution of the shaft results in the following averaged stiffness matrix:

$$[K]_{avg} = \begin{bmatrix} k_{11_y} & 0 & 0 & k_{12_y} \\ 0 & k_{11_x} & k_{12_x} & 0 \\ 0 & k_{21_x} & k_{22_x} & 0 \\ k_{21_y} & 0 & 0 & k_{22_y} \end{bmatrix}, \tag{6.14}$$

where $k_{11_y} = k_{11_x}$, $k_{22_y} = k_{22_x}$, and so forth. Hence, the coordinates u_ξ and u_η, for example, realize the same peak-to-peak value in the inertial frame over one revolution, thus resulting in a circular steady state orbit in the inertial frame. However, Casey [37] experimentally measures 2X orbits which are decidedly asymmetric. In Casey's experimental work, a small 2X resonant peak is observed even in the absence of a crack; therefore, an additional phenomena must be present to generate this harmonic. The zero crack depth 2X harmonic could be attributed to the presence of nonlinearities in the experimental system, or additional aspects of the real test rig, such as shaft misalignment or bow.

Interestingly, the figures indicate that the rotor's angular response is more sensitive to changes in notch depth and location than the lateral response. This conclusion is not surprising, considering the crack essentially acts as a joint where the angular stiffness is significantly less than the lateral stiffness (see Eq. 3.9). The offset of the orbit indicates the static deflection of the system. Intuitively, forcing due to gravity in the ξ direction should generate a positive u_ξ and γ_η, as evidenced in Figs. 6.11 and 6.13. At resonance, dynamic effects dominate the static displacements due to gravity, and the rotor orbit is mostly centered at the origin.

Examination of only the rotor's orbit fails to elucidate the difference in angular orbits for different notch depth/location pairs (seen in Figs. 6.11 and 6.13). The phenomena is examined further by plotting the orbital mode of the shaft deflection. Figures 6.14, 6.15, and 6.16 provide the lateral and angular modes of the orbit at shaft speeds of 50 Hz, 72 Hz, and 100 Hz, respectively. The orbits are obtained

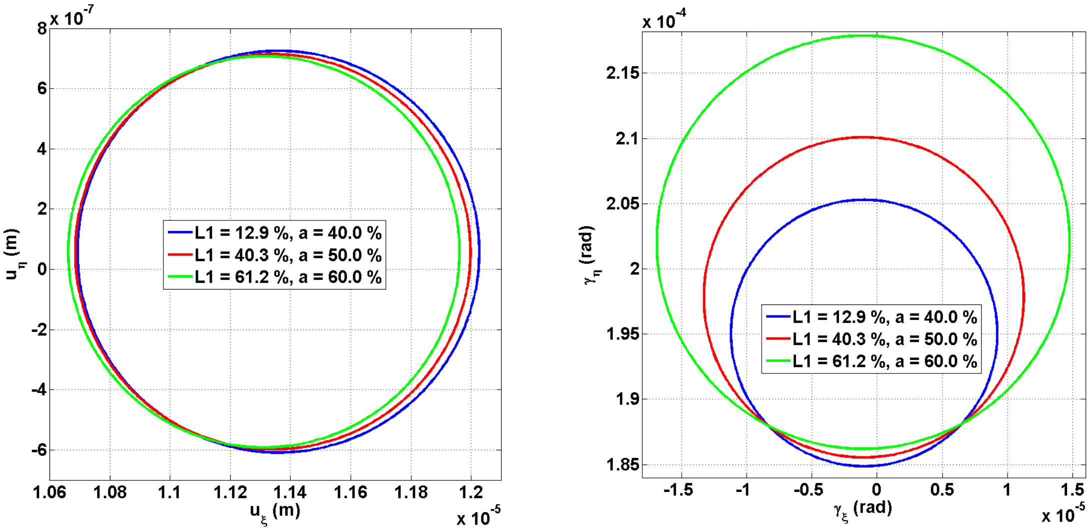

(a) Lateral response orbit

(b) Angular response orbit

Figure 6.11: Notch Crack: Steady-state rotor orbits for several equal 2X resonance frequency pairs at resonance (n = 50 Hz)

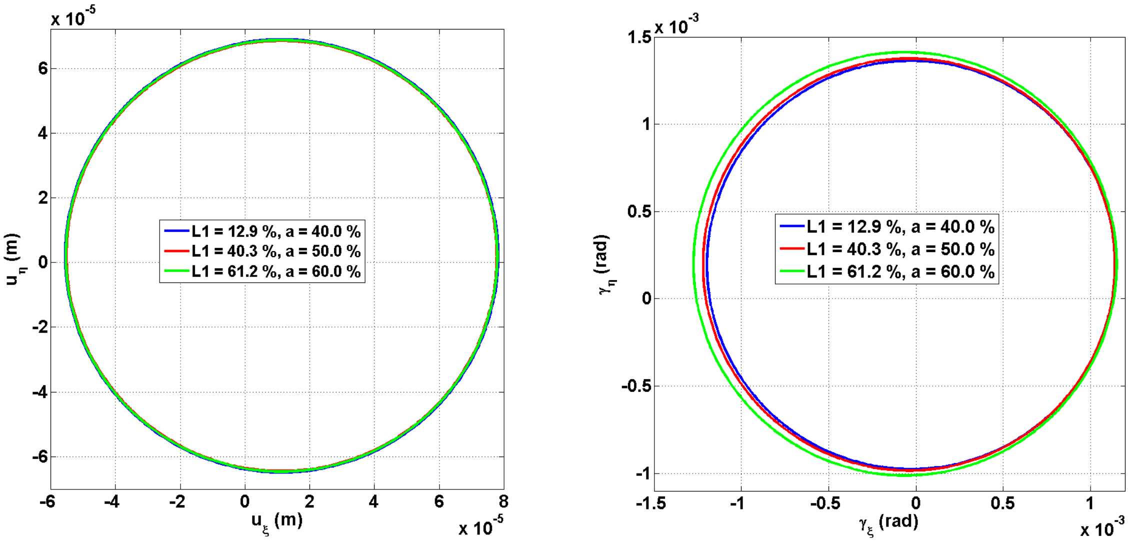

(a) Lateral response orbit

(b) Angular response orbit

Figure 6.12: Notch Crack: Steady-state rotor orbits for several equal 2X resonance frequency pairs at resonance (n = 72 Hz)

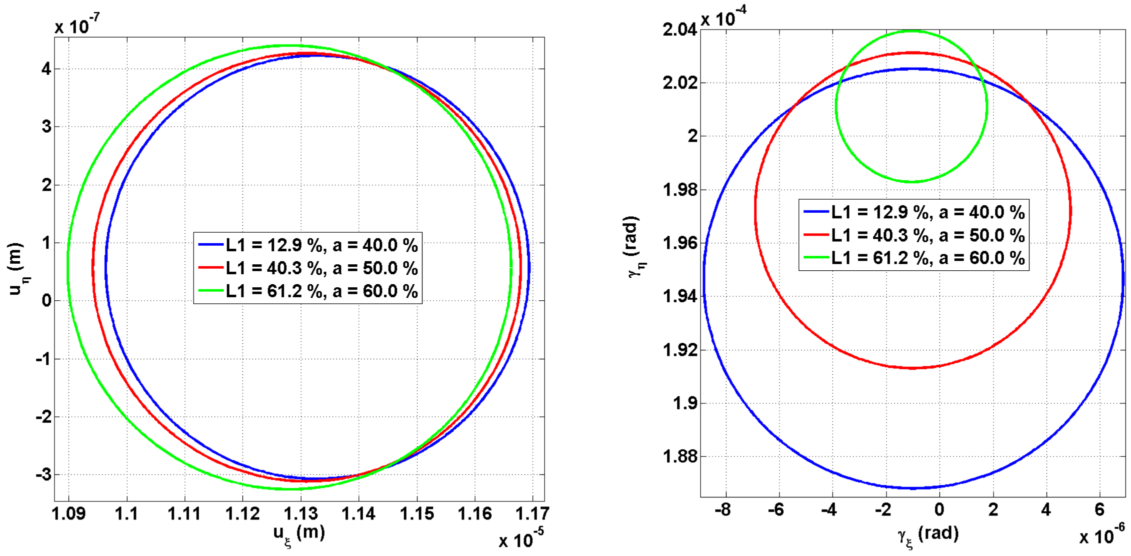

(a) Lateral response orbit

(b) Angular response orbit

Figure 6.13: Notch Crack: Steady-state rotor orbits for several equal 2X resonance frequency pairs above resonance (n = 100 Hz)

using several field matrices in the transfer matrix analysis and subsequently applying Eqs. 6.12 and 6.13 to each nodal state vector. Just as before, the orbits at each point along the shaft are circular, though the aspect ratio of the plots may indicate otherwise. To best visualize the results, the degrees of freedom are plotted such that the coordinate displaying static deflection is along the vertical axis. Static deflection is indicated in the figures.

The notch depth and location pair of $L_1 = 40.3\%$ and $a = 50\%$ is investigated. Once again, the figures indicate that the notch influences the angular response of the rotor more drastically than the lateral response. Figure 6.14 shows that at shaft speeds below the 2X resonance frequency, the system is dominated by stiffness effects. The notch acts as a joint, and gravity exacerbates the shaft deflections following the notch location. At the 2X resonance shaft speed, the angular and lateral responses increase monotonically along the shaft length. Above the 2X resonance shaft speed, inertial effects dominate the response; the rotor's center of mass attempts to return to its equilibrium, and the notch assists by introducing additional compliance. Hence, the orbits beyond the crack decrease in magnitude.

6.3 Gaping Fatigue Crack

The forced response results for the gaping fatigue crack are obtained in a manner analogous to that of the notch crack results discussed previously. The qualitative interpretation of the results is mostly identical to that of the notch results. Comparison is made between the notch and gaping fatigue crack results.

6.3.1 Fixed Gaping Fatigue Crack Location

Figure 6.17 shows the frequency spectra of the gravity-forced response of γ_ξ for a system displaying a crack of 40% depth located 6.35 mm (0.25 inches) from the support. It is clear upon comparison to the notch model (Fig. 6.4b) that a gaping fatigue crack results in a larger 2X magnitude response than a notch of equal depth and location. Eight inertial eigenvalues are present because the crack excites both forward and backward response components.

Figure 6.18 gives the inertial steady-state gravity-forced response for a range of shaft speeds. The shaft speed range encompasses the 2X resonance shaft speed for both crack depths investigated (20% and 40%). Two crack depths are investigated; Figs. 6.18a and 6.18b give the response for cracks of depth 20% and 40%, respectively. Figure 6.18 shows that far from resonance, the 2X harmonic component of the response is significantly diminished. The 2X harmonic component of the response passes through resonance in both figures, as evident by the sudden increase in magnitude. Also note that the magnitude of the 2X harmonic is significantly greater in Fig. 6.18b than in Fig. 6.18a.

Just as with the notch, the Complex Extended Transfer Matrix is used to extract only the steady-state 2X component of the rotor's angular response. Figure 6.19 provides the 2X angular response as a function of crack depth and shaft speed, while Fig. 6.20 shows a color-map representation of Fig. 6.19 for clarity.

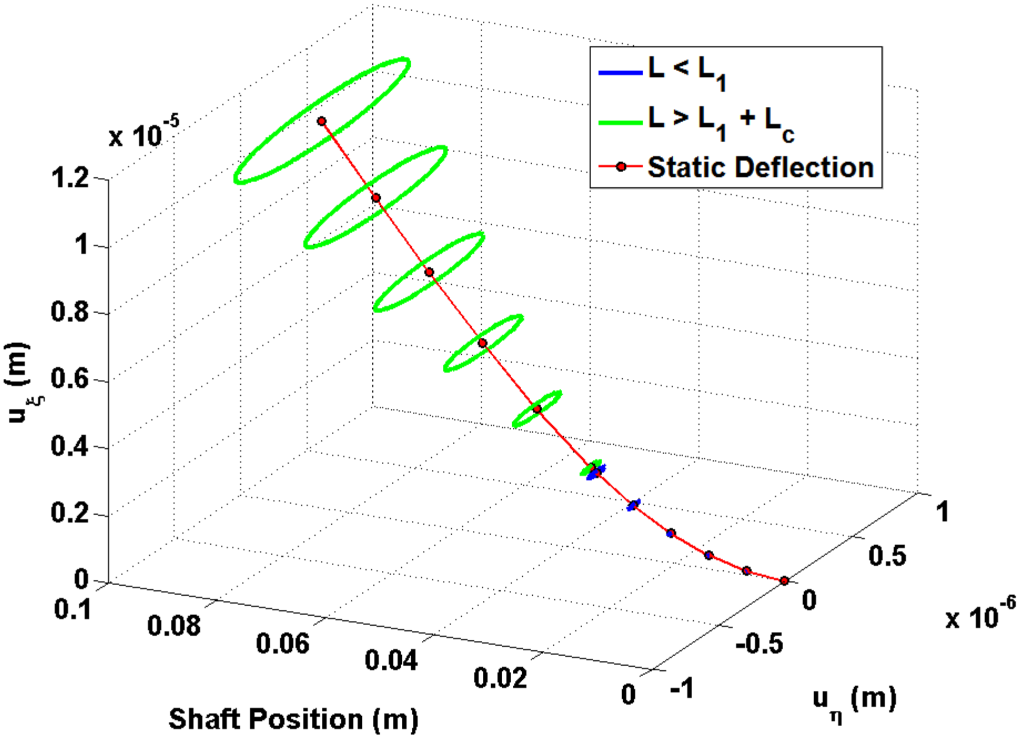

(a) Lateral response orbit

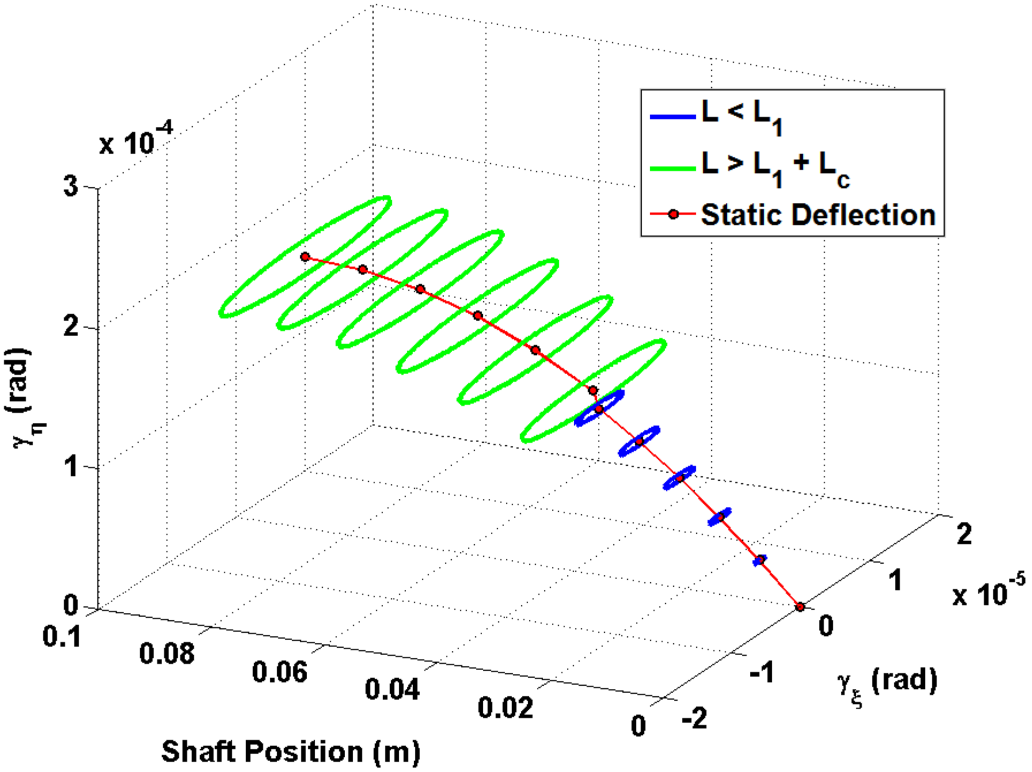

(b) Angular response orbit

Figure 6.14: Notch Crack: Steady-state orbital modes for $L_1 = 40.3\%$, $a = 50\%$ at a shaft speed of 50 Hz

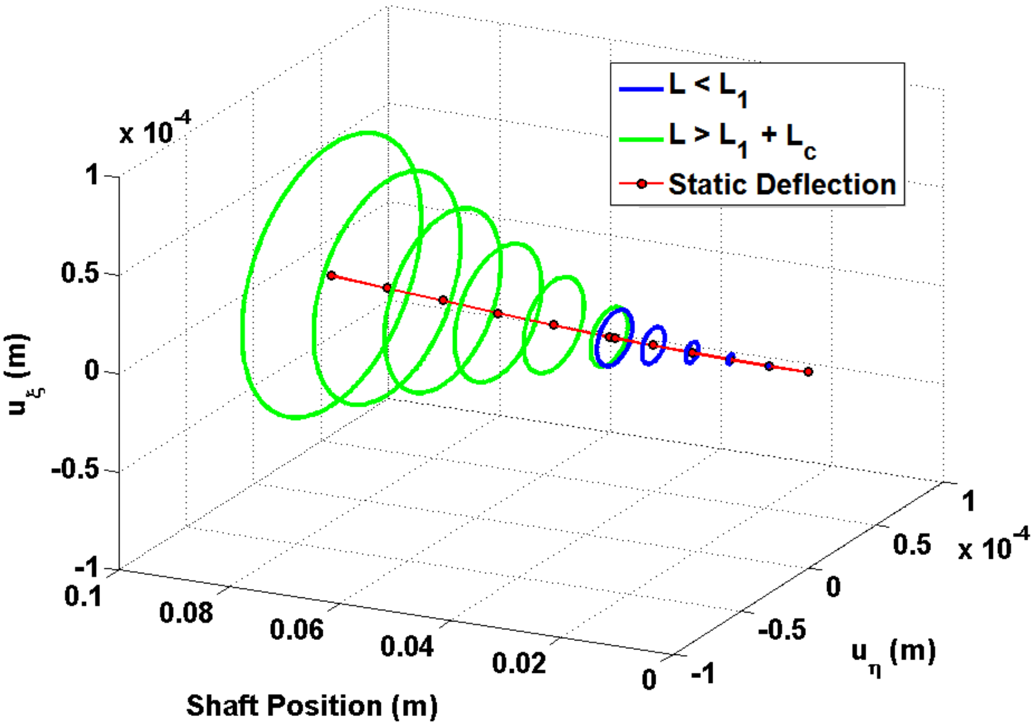

(a) Lateral response orbit

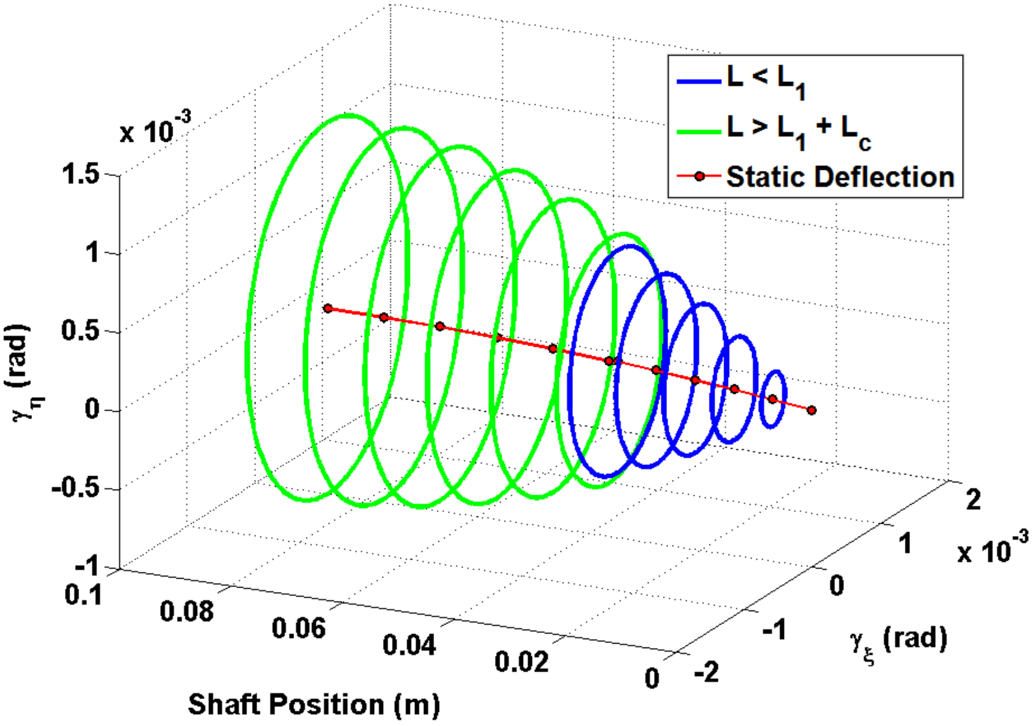

(b) Angular response orbit

Figure 6.15: Notch Crack: Steady-state orbital modes for $L_1 = 40.3\%$, a = 50% at a shaft speed of 72 Hz

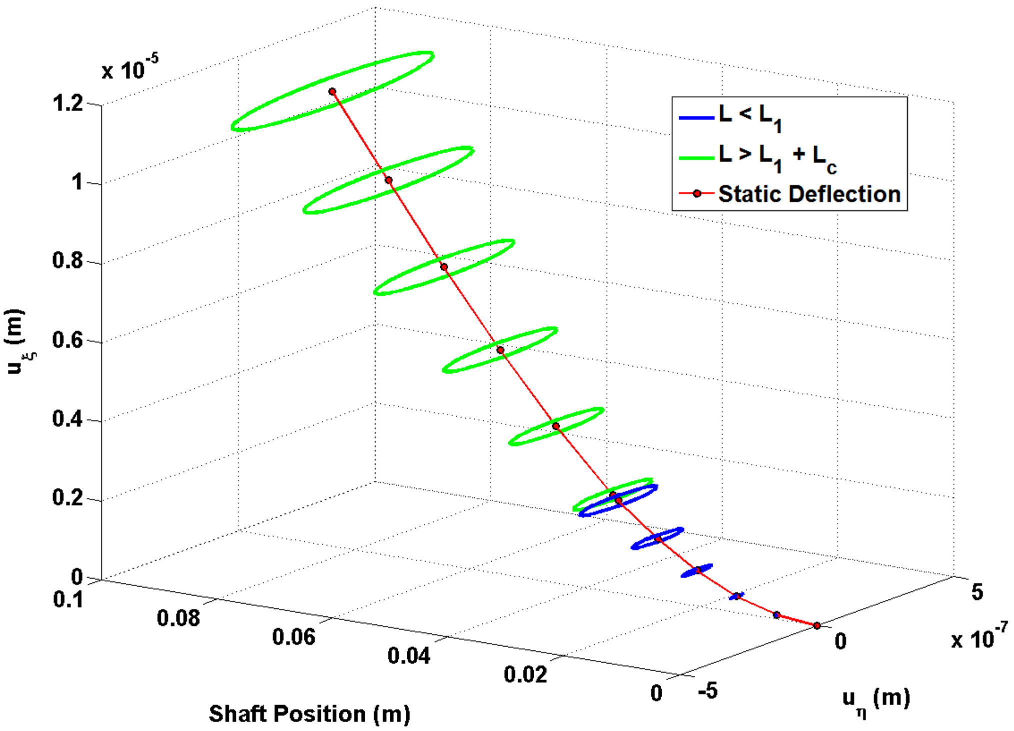

(a) Lateral response orbit

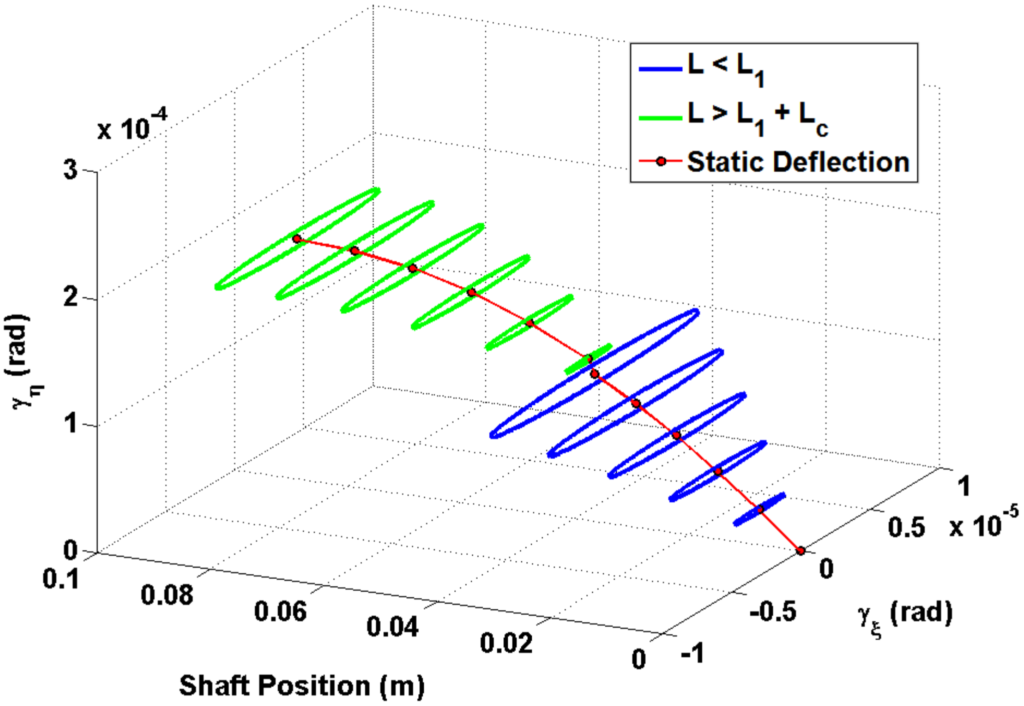

(b) Angular response orbit

Figure 6.16: Notch Crack: Steady-state orbital modes for $L_1 = 40.3\%$, $a = 50\%$ at a shaft speed of 100 Hz

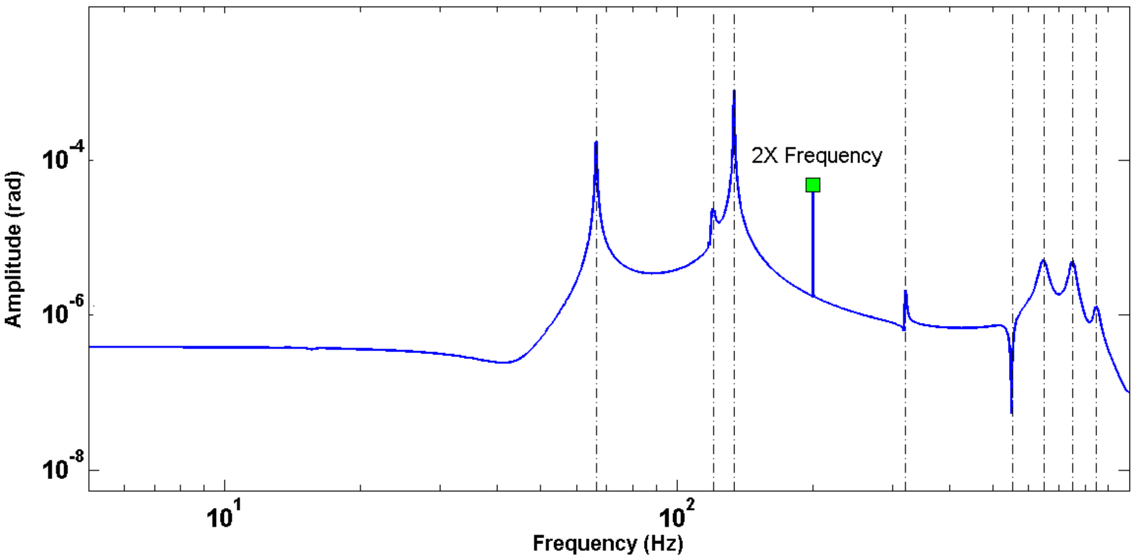

Figure 6.17: Gaping Fatigue Crack: Gravity-forced response of γ_ξ for a system displaying a 40% depth crack located 6.35 mm from the support

An interesting phenomenon is observed in Figs. 6.19 and 6.20: the 2X magnitude of the resonant tilt response reaches a constant value for cracks of approximately 60% and greater. Fig. 3.8 demonstrates that the relationship between the crack compliance coefficients (i.e., the c_{ij} values) qualitatively changes at approximately 60% crack depth. At this point, the coupling term c_{45} draws very close in magnitude to c_{44} and c_{55}. The compliance matrix of the cracked system (Eq. 3.34) demonstrates that this coupling term can have a pronounced effect on the system response, given that its magnitude is significant compared to that of the other terms. It is hypothesized that the leveling of the 2X resonant tilt magnitude is strongly influenced by the fundamentally changed nature of the crack compliance coefficient c_{45}.

It is important to recognize the fundamental limitations of the gaping fatigue crack model. The compliance of the gaping crack is determined by examining the stress intensity factor along the crack edge. For deep cracks, a majority of the crack surfaces are located far from the stress intensity factor. It is possible that for deep cracks, such as those generating the constant region of the 2X response, the method

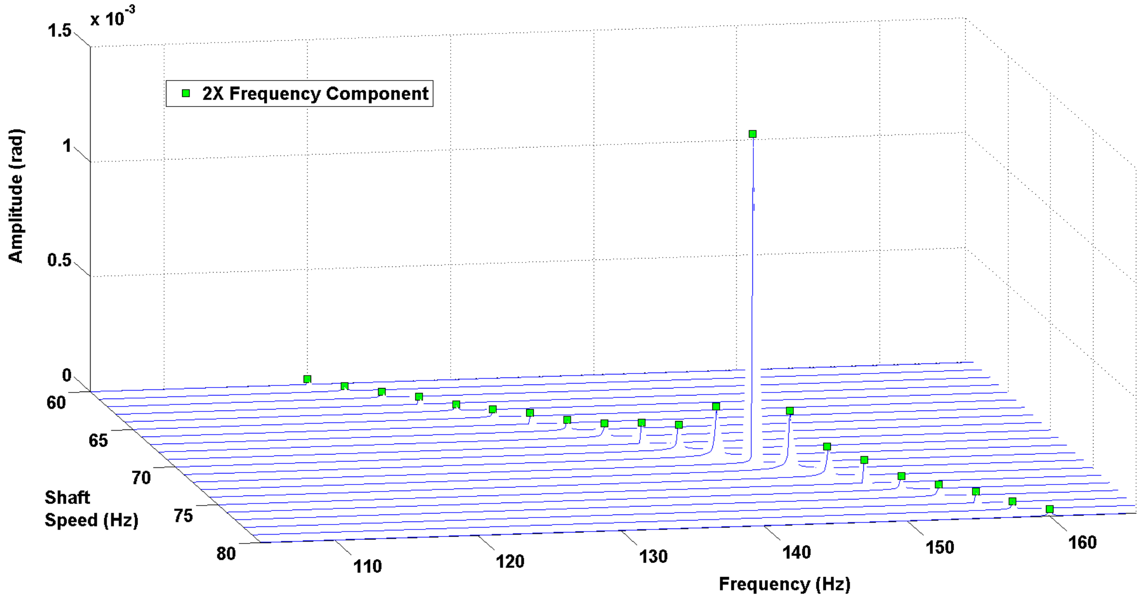

(a) Crack depth: 20%

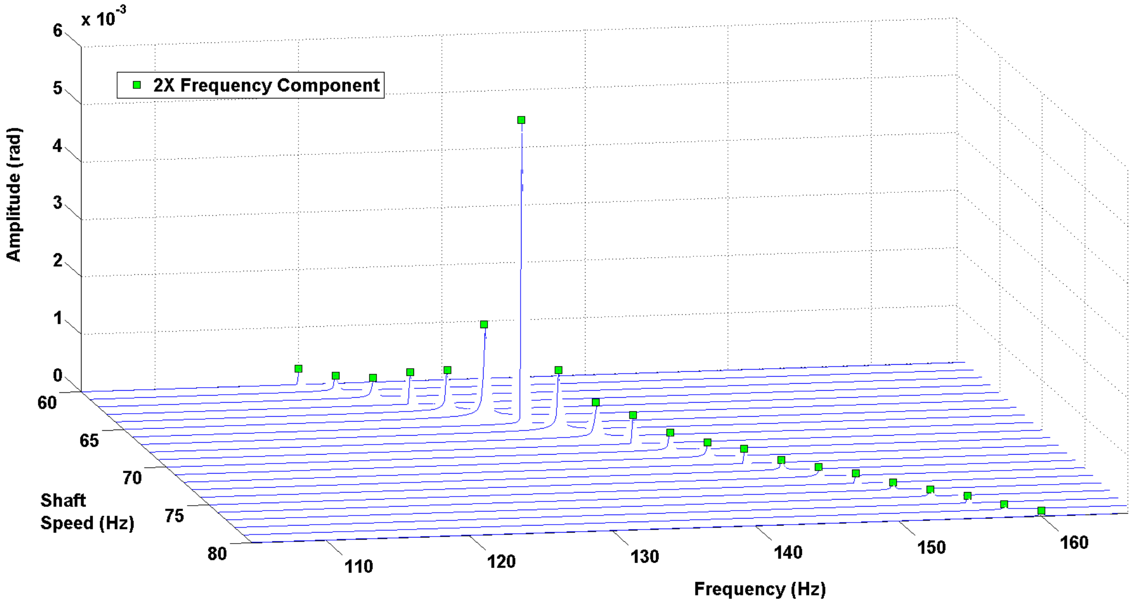

(b) Crack depth: 40%

Figure 6.18: Gaping Fatigue Crack: Steady-state response of γ_ξ for a crack located 6.35 mm from the support

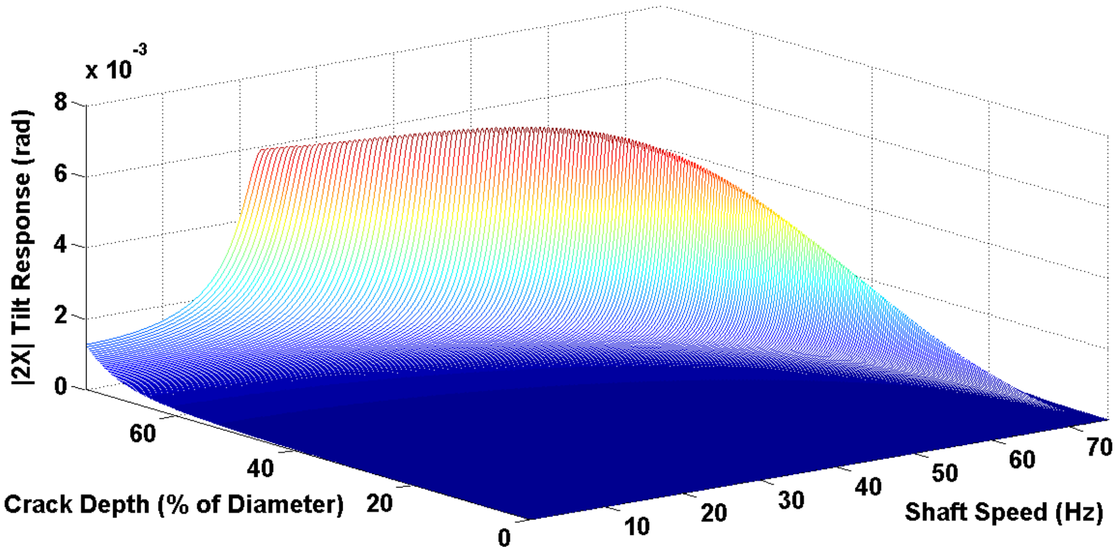

Figure 6.19: Gaping Fatigue Crack: Magnitude of 2X harmonic of angular response for a fixed location crack

employed to estimate the crack compliance is no longer quantitatively accurate.

6.3.2 Variable Gaping Fatigue Crack Location

Figure 6.21 presents the magnitude of the rotor's 2X resonant angular response as a function of crack depth and location. From the plot, it is clear that as the crack becomes deeper and draws closer to the support, the magnitude of the 2X resonant response increases. Once again, the changing relationship between the crack compliance coefficients induces unexpected results for crack depths above approximately 60%. The previous case investigated a line of constant crack location. Figure 6.21 demonstrates that as crack depth increases for a constant crack location, the magnitude of the 2X resonance plateaus for constant crack location lines (as evidenced in Figs. 6.19 and 6.20).

Orbital plots of the rotor's center C are provided in Figs. 6.22, 6.23, and 6.24 for shaft speeds of 50 Hz, 70 Hz, and 100 Hz, respectively. Several pairs of crack depth and location yielding the same 2X resonance frequency of 70 Hz are investigated. Once again, the response far from resonance is influenced strongly by the static deflection

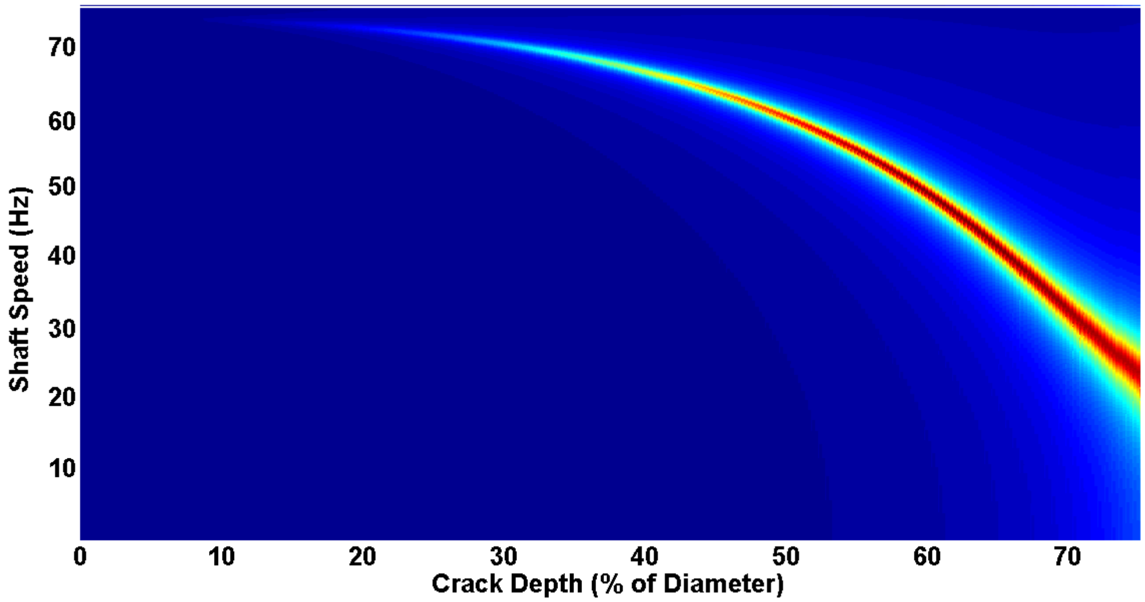

Figure 6.20: Gaping Fatigue Crack: Color-map representation of 2X angular response magnitude for a fixed location crack

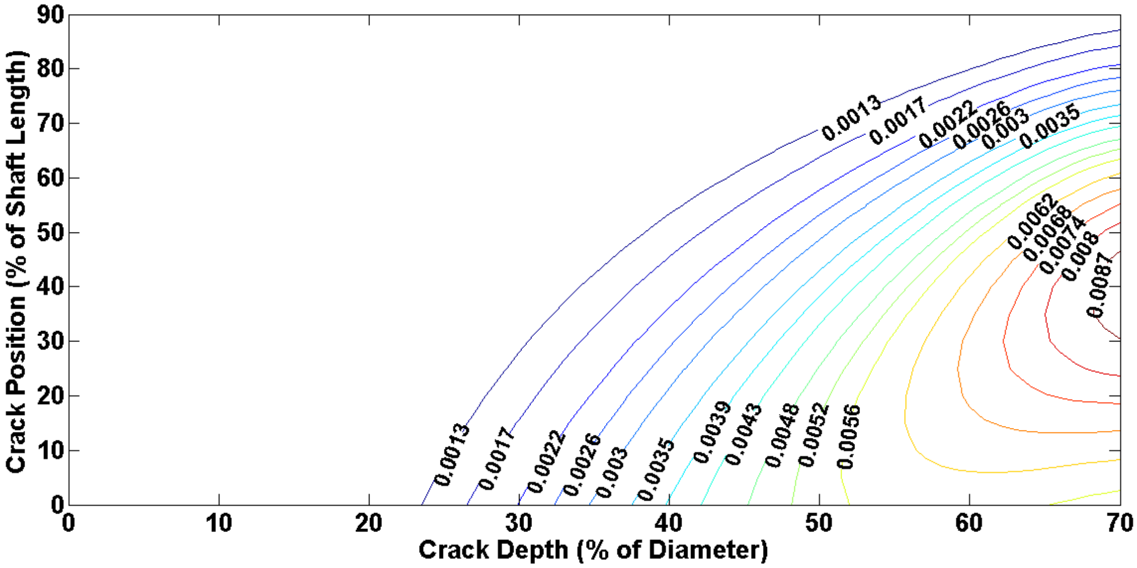

Figure 6.21: Gaping Fatigue Crack: 2X resonant magnitude of angular response versus crack location and depth

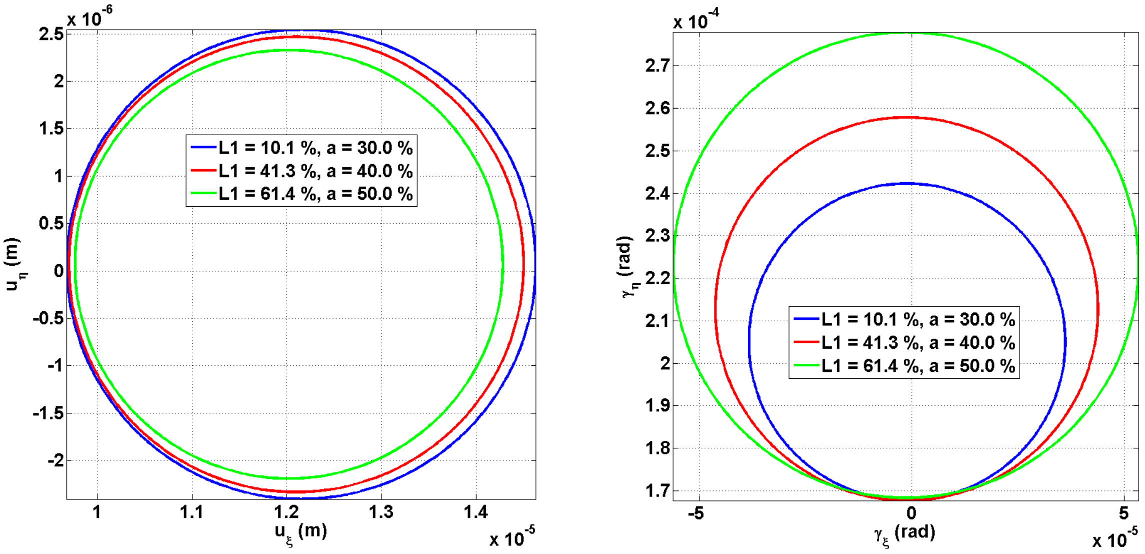

(a) Lateral response orbit

(b) Angular response orbit

Figure 6.22: Gaping Fatigue Crack: Steady-state rotor orbits for several equal 2X resonance frequency pairs at resonance (n = 50 Hz)

of the system. At resonance, dynamic effects dominate, thus reducing the magnitude of the orbit's offset compared to the radius. The angular response is once again influenced more strongly by the crack than the lateral response. The diagnostic implications of this observation are discussed in Chapter 7.

Comparing Fig. 6.24 to the corresponding notch results (Fig. 6.13) clearly indicates that the profile of the response is qualitatively different for the two crack models. As the notch moves closer to the rotor and increases in depth, the angular offset increases faster than for the gaping fatigue crack. The primary difference between the notch and gaping crack models is the presence of several additional coupling terms in the gaping crack compliance matrix, Eq. 3.34. By setting these coupling terms to zero, the profile of Fig. 6.24 shifts to resemble that shown in Fig. 6.13.

Just as with the notch, presentation of only the rotor's orbit fails to explicate the relationship between the orbits for different shaft speeds. Figures 6.25, 6.26, and 6.27 provide the orbital modes for a crack where $a = 40\%$ and $L_1 = 40.3\%$. To present the results most clearly, the coordinate which is statically deflected is plotted on the

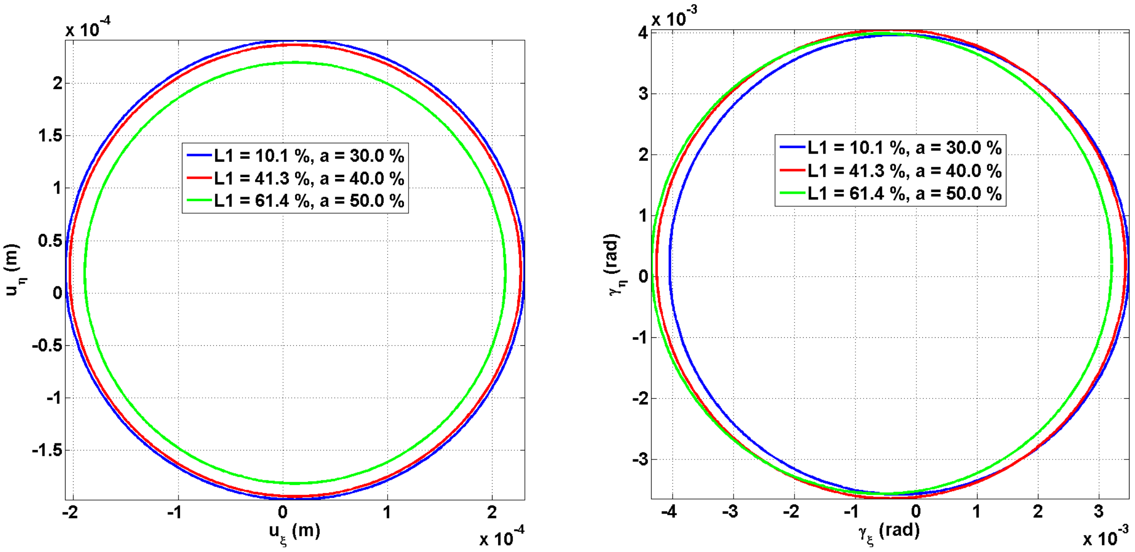

(a) Lateral response orbit

(b) Angular response orbit

Figure 6.23: Gaping Fatigue Crack: Steady-state rotor orbits for several equal 2X resonance frequency pairs at resonance (n = 70 Hz)

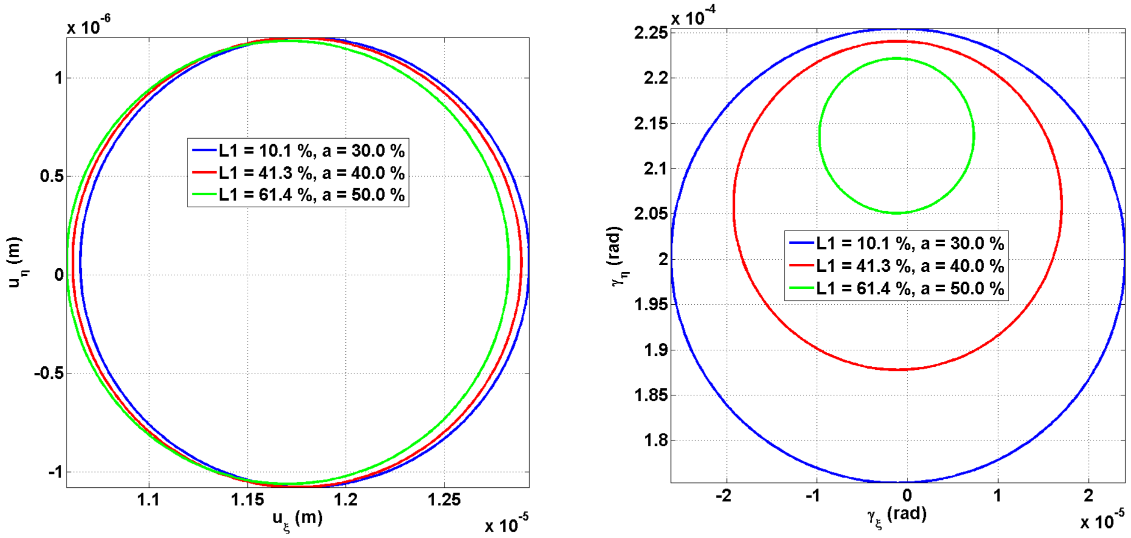

(a) Lateral response orbit

(b) Angular response orbit

Figure 6.24: Gaping Fatigue Crack: Steady-state rotor orbits for several equal 2X resonance frequency pairs above resonance (n = 100 Hz)

vertical axis (u_ξ and γ_η).

Once again, the orbital mode below the 2X resonance indicates that the system is dominated by stiffness effects. The crack acts as a joint, and the load caused by gravity increases the deflections (both lateral and angular) following the joint. At resonance, the offset is negligible in comparison to the radius of the 2X harmonic, and the displacements increase smoothly across the length of the shaft. Above the 2X resonance frequency, inertial effects dominate. The rotor attempts to return to its equilibrium position, and the crack assists by providing additional compliance. Aspects of the orbital modes relevant to condition monitoring are discussed in Chapter 7; specifically, the practicality of employing modes to diagnose the location of the crack.

6.4 Summary of Forced Response Results

A forced response analysis of both crack models is presented, along with a method for transforming the rotating frame results to the inertial frame. For each crack model, two situations are investigated: a fixed-location crack and a crack where the location and depth are allowed to vary. The gravity-forced response is obtained using the equations of motion and also the Complex Extended Transfer Matrix. When a crack and gravity are present, a 2X harmonic frequency appears in the system response. Also, the transient response indicates that the crack excites both forward and backward whirl components. The steady-state 2X response is shown to reach its maximum at the 2X resonance frequency, and decrease substantially as the shaft speed is varied away from resonance. The fixed-location investigation demonstrates that as the crack increases in depth, the 2X resonance frequency decreases while the magnitude of the resonance increases.

The magnitude of the steady-state 2X component of the rotor's angular response is provided versus crack depth and location for both crack models. Once again, the

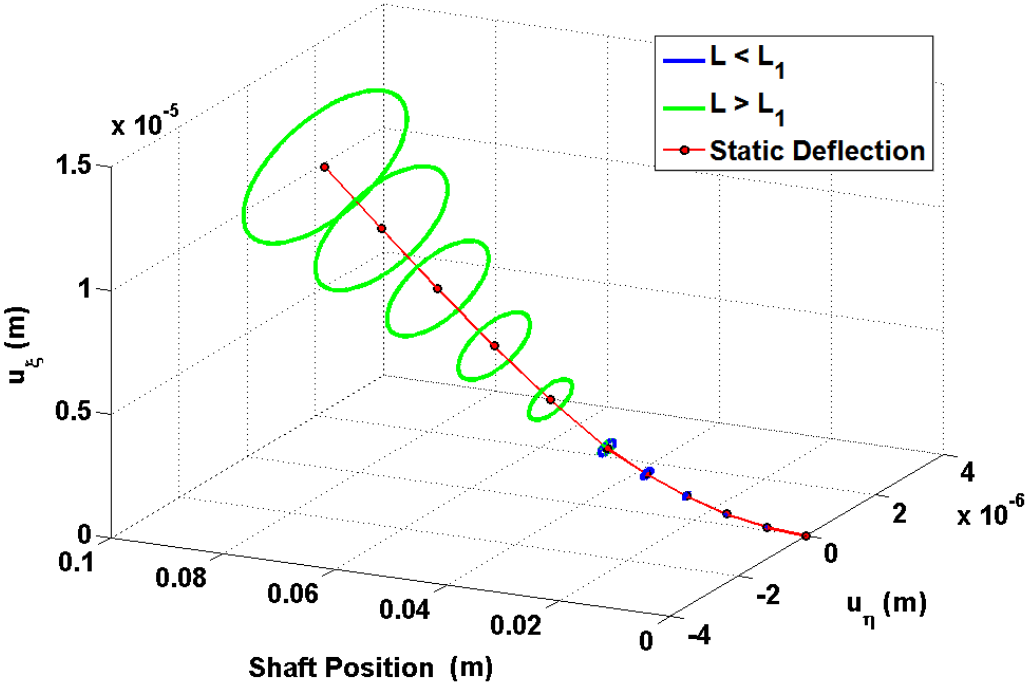

(a) Lateral response orbit

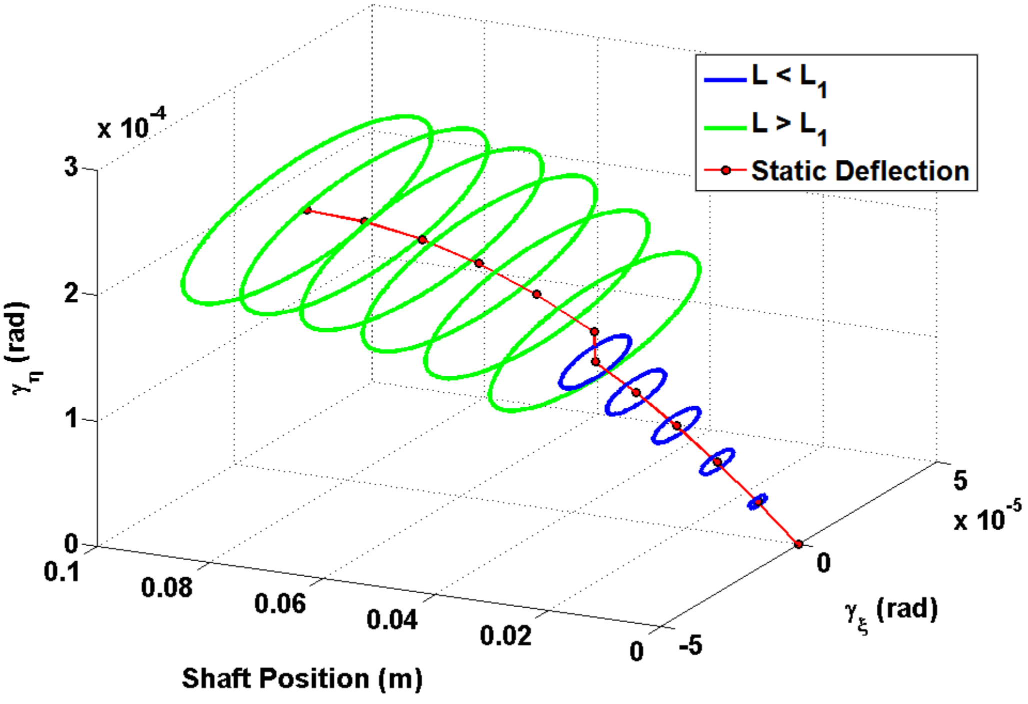

(b) Angular response orbit

Figure 6.25: Gaping Fatigue Crack: Steady-state orbital modes below resonance (n = 50 Hz, $L_1 = 41.3\%$, a = 40%)

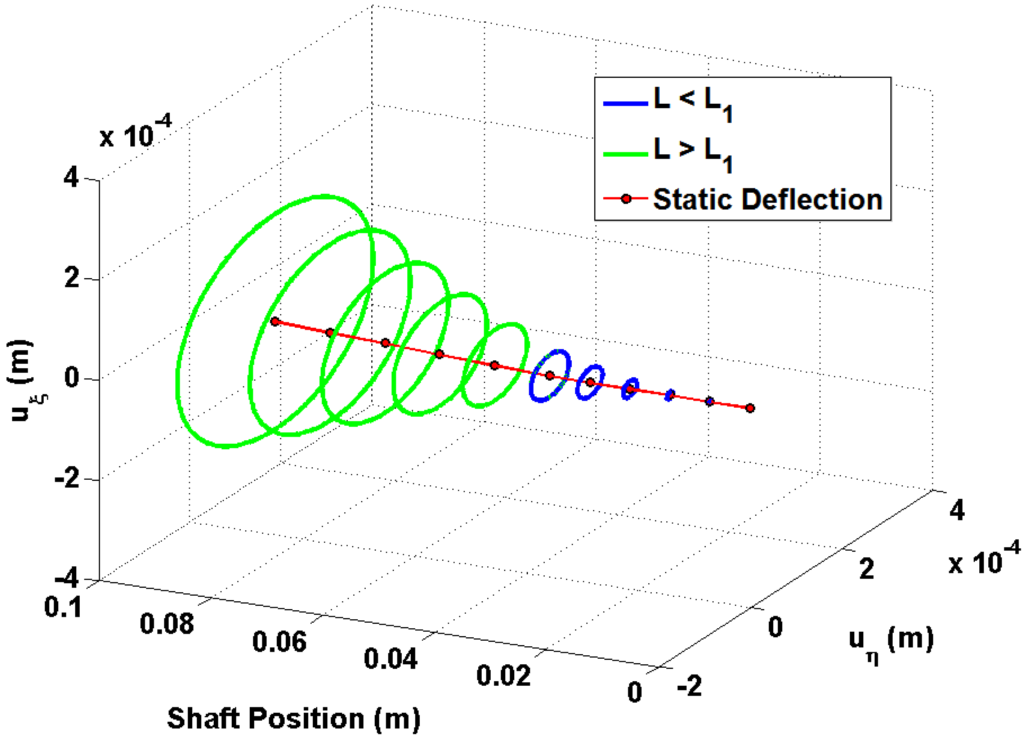

(a) Lateral response orbit

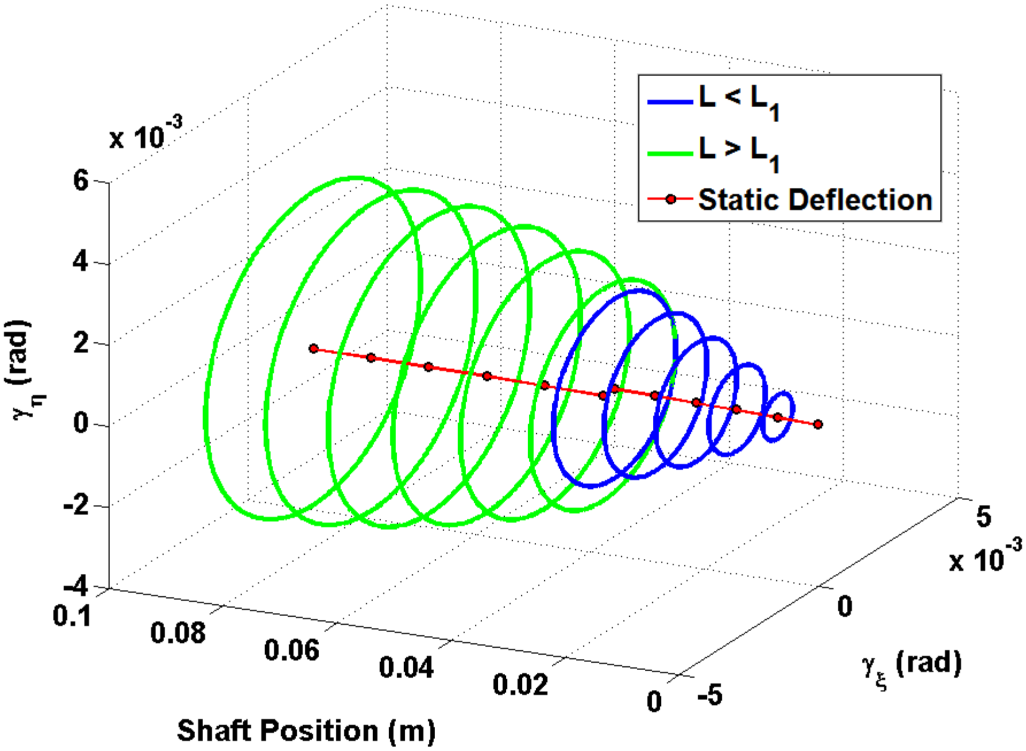

(b) Angular response orbit

Figure 6.26: Gaping Fatigue Crack: Steady-state orbital modes at resonance (n = 72 Hz, L_1 = 41.3%, a = 40%)

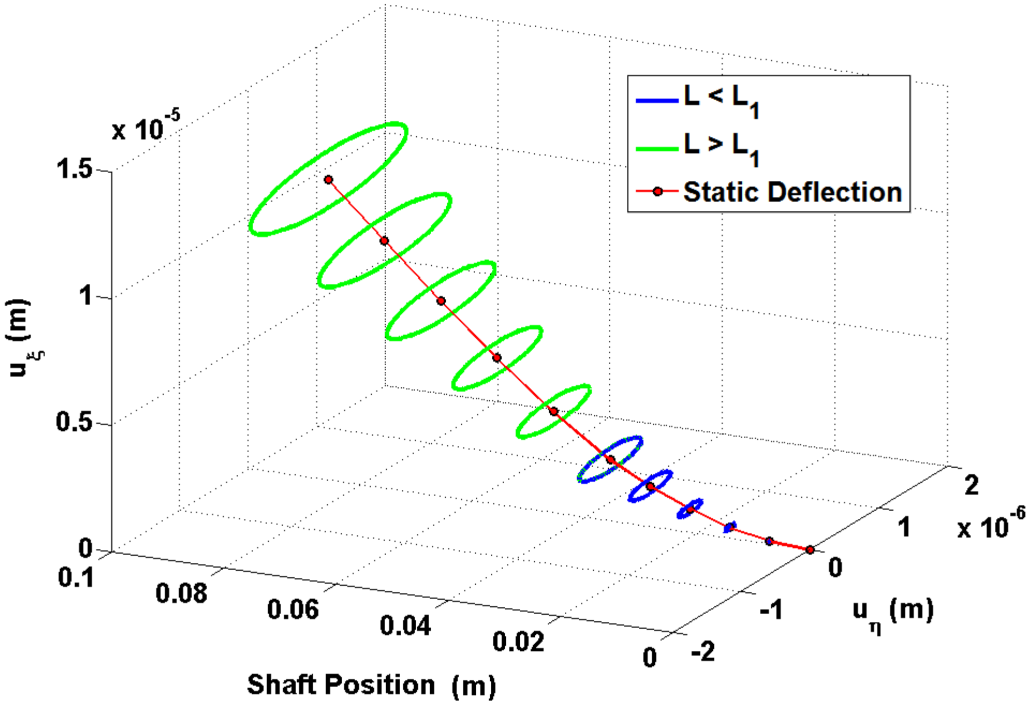

(a) Lateral response orbit

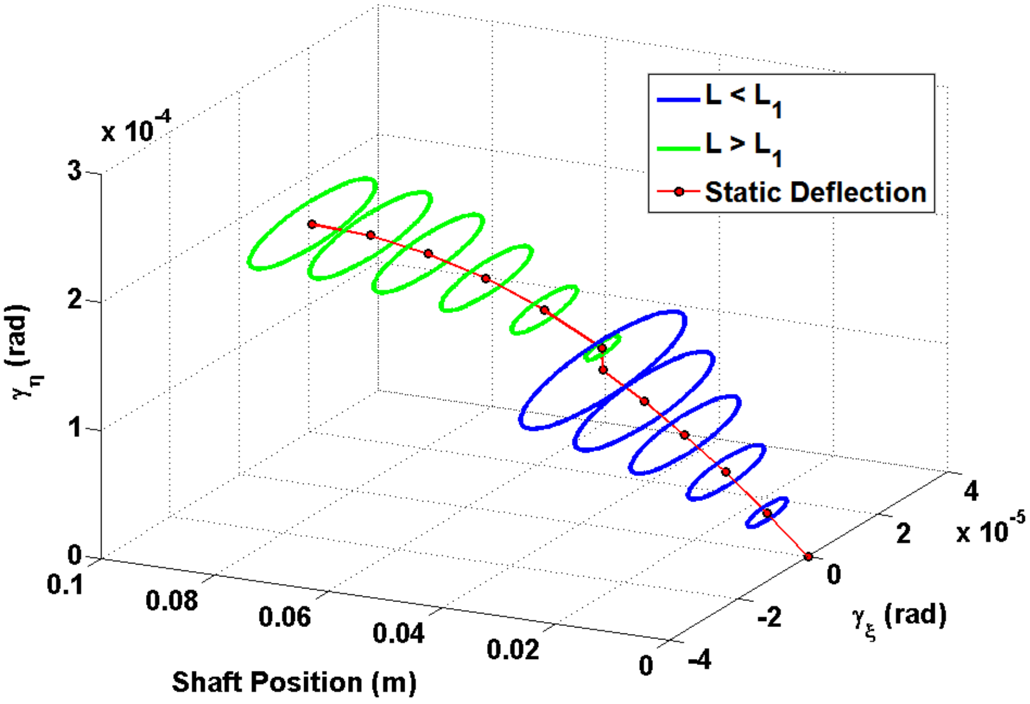

(b) Angular response orbit

Figure 6.27: Gaping Fatigue Crack: Steady-state orbital modes above resonance (n = 100 Hz, $L_1 = 41.3\%$, a = 40%)

trend indicates that as the system stiffness is reduced, the 2X resonance frequency decreases while the magnitude of the resonance increases. Orbits of the steady-state response of the rotor are given for several crack depth and location pairs yielding the same 2X resonance frequency and over several shaft speeds. The concept is extended to the orbital modes, and the profile of the steady-state shaft deflection (both lateral and angular) is provided. The relation between the orbits is discussed qualitatively.

Chapter 7 extensively interprets the results given in this chapter, in the context of crack detection and diagnosis. Specifically, the results presented for the scenario in which crack depth and location are free to vary are employed to diagnose the parameters of the crack.

CHAPTER VII

CRACK DIAGNOSTICS

Crack detection provides the operator of a rotordynamic system information concerning only the presence of a crack; the operator does not know where the crack has formed or its depth, which are two important indicators of crack severity. This work investigates the feasibility of employing the 2X shaft speed harmonic to detect a crack and diagnose its parameters (i.e., location and depth). Furthermore, a successful crack diagnosis system should employ simple methods and procedures for extracting and processing the dynamic response of the system.

The difficulty in employing a simple measurement system (both hardware and signal processing techniques) to diagnose crack depth and location is that often a single piece of information is sought to provide two crack parameters. However, the results from the previous chapter indicate that a single measurement, such as the 2X resonance frequency, is inadequate to diagnose multiple crack parameters (see Figs. 5.14 and 6.21).

In accordance with the results presented in Chapters 5 and 6, two signals are proposed for diagnosing the parameters of the crack: the 2X resonance frequency and the magnitude of the rotor's angular response at resonance. The suggested procedure is presented, along with qualitative observations relating to practical fault diagnosis. Orbital shapes (of the rotor and the shaft) are discussed as a possible detection and diagnosis tool. Distinctions between the notch and gaping fatigue crack are discussed pertaining to crack diagnosis. First, a discussion on crack detection is presented to contextualize the discussion on crack diagnostics.

7.1 Employing the 2X Shaft Speed Harmonic for Crack Detection

Using only the presence of the 2X harmonic to detect a transverse shaft crack is problematic. For example, Sanderson [66] investigates crack detection in the turbo-generator of a nuclear power plant and finds that a crack was not detected until it had reached 25% depth. A majority of the condition monitoring systems relying on the 2X shaft speed harmonic for crack detection assume the machinery is in a normal, on-line state of operation (that is, operation is occurring at a single predetermined shaft speed).

Figure 6.6a provides the gravity-forced response of the notched system over a range of shaft speeds far from the critical 2X resonance frequency. The response for a shaft speed range encompassing the 2X resonance frequency is given in Figs. 6.7 and 6.18 for the notch and gaping fatigue crack, respectively. Though the figures are for a single crack depth and location, a = 40 % at 6.35 mm (0.25 inches) from the support, practical observations for real crack detection are drawn.

The magnitude of the 2X shaft speed harmonic is minute when the shaft speed is far from the 2X resonance frequency (as seen in Fig. 6.6a). Near the 2X resonance frequency, the magnitude of the 2X harmonic greatly increases (Figs. 6.7 and 6.18b). Comparison of the aforementioned figures elucidates that even for a crack of 40% depth, the magnitude of the 2X harmonic can be prohibitively small if the operational shaft speed of the system is far from resonance. Compared to operational noise and measurement error, the 2X harmonic may in fact be undetectable in these regimes.

Furthermore, the detection of a crack depends on the shaft speed and the crack's depth and location. Figures 6.10 and 6.21 provide the magnitude of the angular response at the 2X resonant shaft speed for both crack models, over a range of possible crack depths and locations. From the plots, it is clear that the angular 2X resonant magnitude is relatively small for many combinations of crack depths and locations, particularly when the crack is shallow or close to the rotor. Detecting the 2X harmonic even at resonance is dependent on the properties of the specific measurement apparatus, e.g., the sensor's accuracy or the measurement location. Therefore, even for operation near the 2X resonant shaft speed, crack detection is a complicated procedure and cannot be assured. It is also seen through comparison of Figs. 6.10 and 6.21 that a notch crack is substantially harder to detect than a commensurate gaping fatigue crack. This result is expected, as the gaping fatigue crack results in a greater loss of stiffness than a notch of equal depth and location.

The steady-state orbits of the rotor center can also provide detection information. Away from resonance, static deflections dominate the offset of the rotor's orbit. Recall that Figs. 6.13b and 6.24b provide the rotor's angular orbit at a shaft speed of 100 Hz for the notch and gaping fatigue cracks, respectively. The radius of the orbit is substantially less than the offset. Comparing the offset (either angular or lateral) to that for an undamaged system could provide useful diagnostic information.

The use of orbits for crack detection is complicated by the presence of additional phenomena such as imbalance. Figure 7.1 provides the angular orbit for a gaping fatigue crack system (a = 40%, L_1 = 41%) with a small imbalance ($m_e\epsilon = 5(10)^{-6}$ kg m) at 100 Hz. Clearly, the orbit shape changes dramatically from that seen in Fig. 6.24b. Caution must be taken to filter the signal such that only the 2X component remains.

An ideal condition monitoring system employs real-time methods to detect a fault. As discussed previously, typical on-line methods entail that the machinery resides in normal operation while condition monitoring occurs. Though not ideal, it is judicious and practical to vary the shaft speed across the 2X resonance frequency if a crack is suspected (for example, a start-up/shut-down procedure can be employed). If a crack is indeed present, the magnitude of the 2X shaft speed harmonic should increase considerably as the shaft speed nears the 2X resonance frequency. The variation of

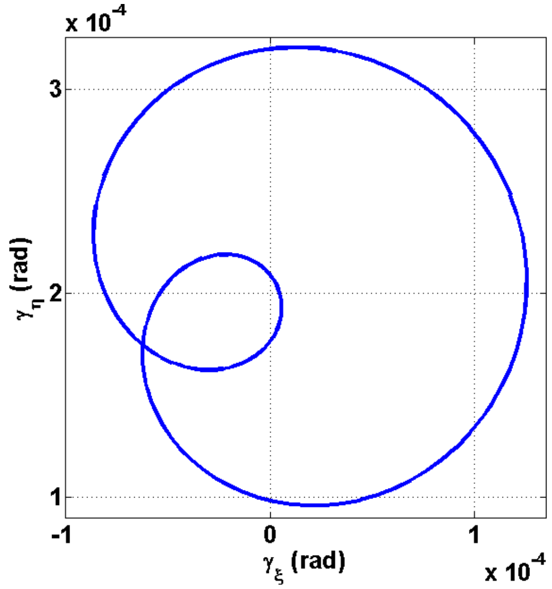

Figure 7.1: Total orbit for a gaping fatigue crack (a = 40%, L_1 = 41%) with a small imbalance ($m_e\epsilon = 5(10)^{-6}$ kg m)

the shaft speed across the 2X resonance frequency requires the operator to have a reasonable estimation of the 2X resonance frequency. To obtain an *a priori* estimate of the 2X resonance frequency, an accurate system model is required.

7.2 Crack Parameter Diagnosis

The crack's depth and location both influence the system's stiffness, and therefore, both influence the profile of the 2X harmonic. Though crack depth is often emphasized due to trepidation of catastrophic failure caused by deep cracks, crack location can be equally hazardous due to high stresses at the crack cross-section. Crack propagation depends on the amplitude of the cyclic stress present at the crack cross-section. The highest stresses in an overhung shaft occur at locations closest to the support because the load due to gravity causes the greatest internal bending moments at these locations. High stresses are also experienced at locations with high stress concentrations; cracks are most likely to initiate and propagate quickly at these locations.

Therefore, the location of the crack determines its propagation rate; cracks in regions experiencing diminished stress propagate slower than cracks in regions of high stress. Diagnosing the crack's location is crucially important for safe operation of rotordynamic systems.

A crack diagnosis procedure is presented here, in relation to the analytic results provided in Chapters 5 and 6. When a crack is suspected, the first step in determining these parameters is to determine the profile of the 2X harmonic by varying the shaft speed across the 2X resonance frequency. Recall that Figs. 5.8 and 5.14 provide the 2X resonance frequency versus crack depth and location for the notch and gaping fatigue crack models, respectively. Measuring the 2X resonance frequency restricts the crack parameters to pairs of depths and locations comprising a contour of equal 2X resonance frequency.

Once the 2X resonance frequency is known, pairs of crack locations and depths comprising a 2X resonance frequency contour are extracted by finding an equivalent crack location corresponding to a set of crack depths. For example, if the target 2X resonance frequency is 71.0 Hz, a free response analysis is performed for a range of crack depths, iterating the crack location until the target frequency is obtained. A crack location and depth pair yielding the target 2X resonance frequency is a point on the contour line, and the entire contour line is composed of many such points. In this fashion, crack locations are found for any given target 2X resonance frequency and crack depth range. Figure 7.2 highlights an example measured 2X resonance frequency contour, with a sample pair of crack depth and location shown.

Several practical qualitative observations applicable to both crack models are made by observing trends in Figs. 5.8 and 5.14. First, the difficulty in detecting small cracks or cracks far from the support is immediately clear by the lack of contours in the leftmost region of the plot. The 2X resonance frequency is fairly stable in this region; that is, changes in crack depth and/or location do not result in large

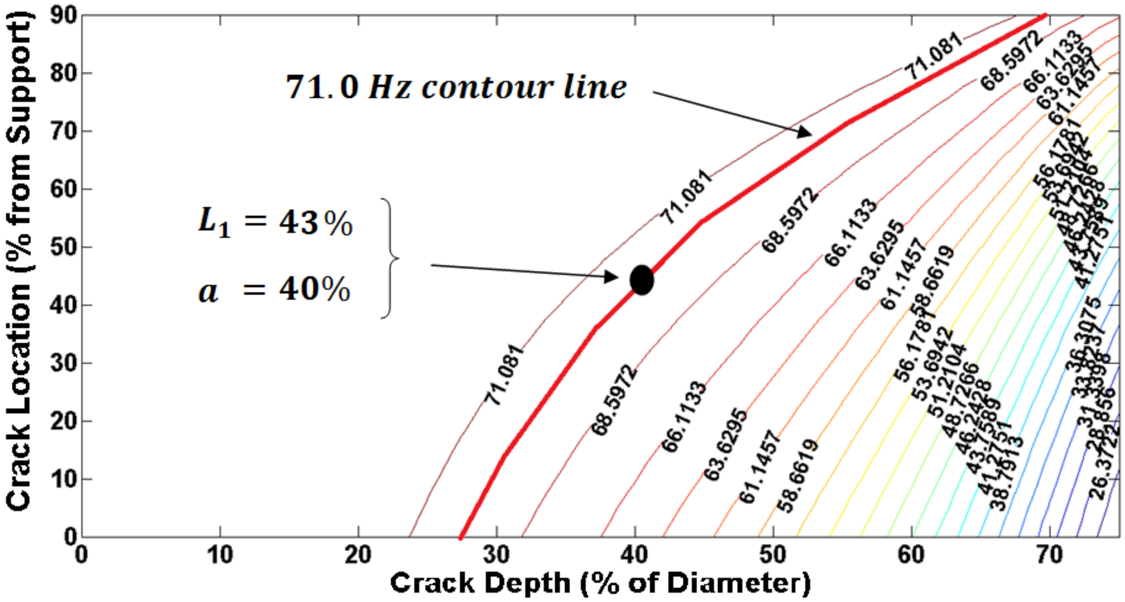

Figure 7.2: Obtaining the 2X resonance frequency of the system

changes in the 2X resonance frequency. To detect cracks in the leftmost region, the 2X resonance frequency must be measured with a high degree of accuracy (this practical limitation will be discussed shortly). However, comparing the notch crack model (Fig. 5.8) and the gaping fatigue crack model (Fig. 5.14) shows that a gaping fatigue crack is easier to detect than a notch of commensurate depth and location, as the 2X resonance frequency for the gaping fatigue crack changes more pronouncedly with variations in crack parameters. This conclusion is expected considering that a gaping fatigue crack results in a greater loss of stiffness than a notch of equal depth/location.

Each 2X resonance frequency contour begins at a specific crack depth and likewise terminates at a particular crack location. This observation has important implications for qualitatively assessing the severity of a crack, given only the 2X resonance frequency. For example, from Fig. 5.14, assume that the 2X resonance frequency is measured to be approximately 66.3 Hz, and a gaping fatigue crack is suspected. The minimum depth of the crack obtained from the figure is approximately 38%, and the crack can be no further from the bearing than approximately 90% of the shaft length. Recognition of this possible range of crack depth and location provides the operator with an immediate sense of crack severity, requiring no further measurement. Though the results are interpreted here using a gaping fatigue crack, the same conclusions can be drawn concerning a notch. Given a specified (or measured) 2X resonance frequency, knowledge of a permissible range of crack depths and locations is often inadequate. Additional analysis or measurement must be performed to extract the actual pair of crack location and depth from the additional pairs comprising the target 2X resonance frequency contour.

The magnitude of the 2X resonant angular response provides an additional parameter to assist in distinguishing crack location and depth. The magnitude of the 2X resonant tilt response of the rotor is obtained along a constant 2X resonance frequency contour line using the Complex Extended Transfer Matrix. Figure 7.3 gives the magnitude of the 2X resonant tilt versus pair number for a notch with a 2X resonance frequency of 73.0 Hz. The term 'pair' refers to combinations of notch locations and depths yielding the same 2X resonance frequency. The pair number corresponds to the notch's depth expressed as a percent of shaft diameter. Also, since the pairs begin with a crack of 0% depth, each 2X resonance frequency does not exist for the entire range of crack depth and location pairs, as evident on the contour plot provided in Fig. 5.8.

Figure 7.3 shows that the magnitude of the 2X resonant tilt response of the rotor varies for different pairs of notch depths and locations giving a 73.0 Hz 2X resonance frequency. Measurement of the 2X resonant tilt magnitude specifies (or at least limits) the range of possible notch depth/location pairs. For example, if the 2X resonance frequency was measured to be 73.0 Hz, and the magnitude of the 2X resonant tilt found to be $1.8(10)^{-4}$ radians, then the notch depth/location would correspond to pair 63 (that is, a notch depth of 63% and the corresponding notch location necessary to generate a 73.0 Hz 2X resonance frequency). A similar plot is provided in Fig. 7.4

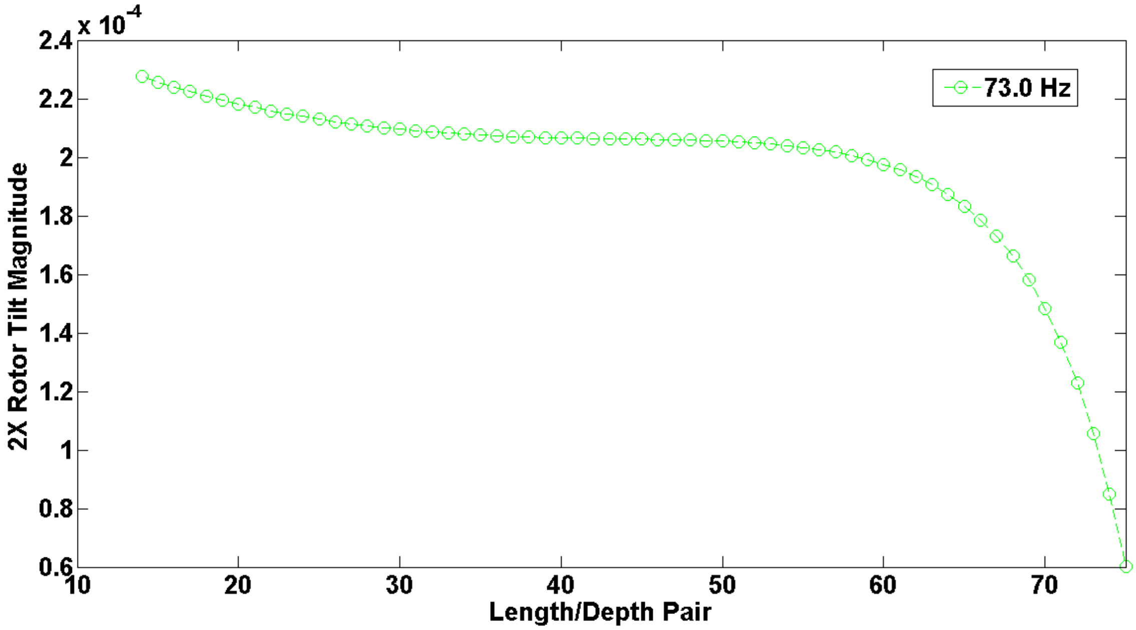

Figure 7.3: Notch Crack: Locus of 2X resonant tilt magnitudes for a target 2X resonance frequency of 73 Hz

for an example 2X resonant frequency of 70.0 Hz. In this case, not all values of the 2X resonant tilt magnitude are unique. However, given a measured 2X resonant tilt magnitude, it is likely that given the nature of propagation the crack depth/location pair is at the location of highest stress. This example indicates that it is not always possible to distinguish crack depth from location, though the procedure reduces the possible combinations.

For reference, a locus of curves such as those found in Figs. 7.3 and 7.4 is provided in Fig. 7.5. Figure 7.6 provides the same information as Fig. 7.5, but plotted versus pair number rather than notch depth and location. The figures immediately signify that it is easier to separate notch depth from location for lower values of the 2X resonance frequency, as the locus demonstrates a larger magnitude of response along with an increased defining structure. This conclusion is intuitive considering that lower 2X resonance frequencies correspond to a greater loss of stiffness. A greater loss of stiffness implies that smaller changes in parameters (i.e., notch location and

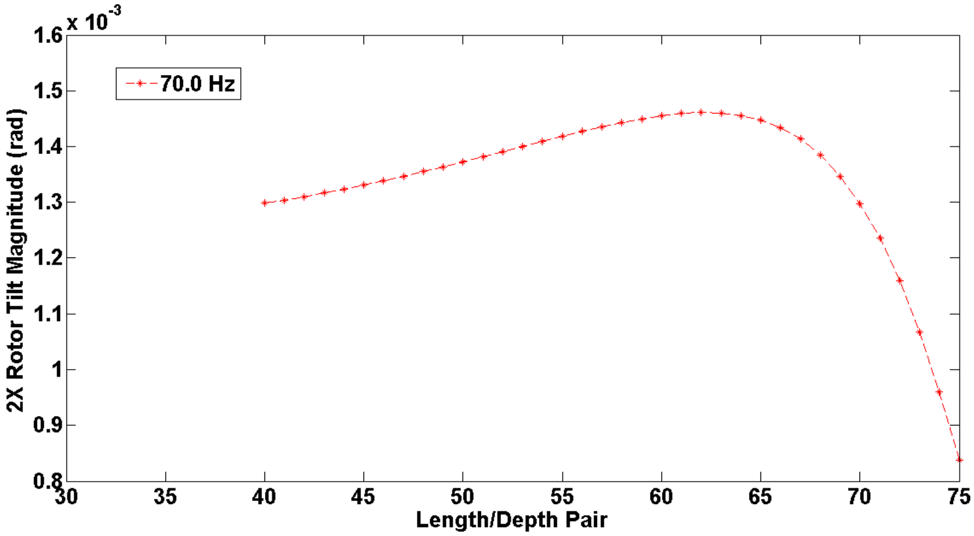

Figure 7.4: Notch Crack: Locus of 2X resonant tilt magnitudes for a target 2X resonance frequency of 70 Hz

depth) result in larger changes in the 2X resonant tilt magnitude. In addition, the 2X resonant tilt magnitude is larger for curves corresponding to lower values of the 2X resonance frequency.

Equivalent results are presented for the gaping fatigue crack model. Figure 7.7 demonstrates the 2X resonant tilt magnitude locus for crack depth/location pairs providing a 73.0 Hz 2X resonant frequency. Figure 7.7 provides the 2X resonant tilt magnitude locus for a 70.0 Hz 2X resonance frequency. Comparing the results from the two models shows that the gaping fatigue crack results in a greater drop in magnitude as the crack depth/location pair number increases. The higher resolution in 2X resonant tilt magnitude allows shallower gaping fatigue cracks to be identified with greater confidence as compared to notches producing the same 2X resonance frequency.

Figure 7.9 provides a locus of crack depth/location pairs for a range of 2X resonance frequencies. The figure implies that it is easier to distinguish crack depth and location for lower values of the 2X resonance frequency, as a larger magnitude

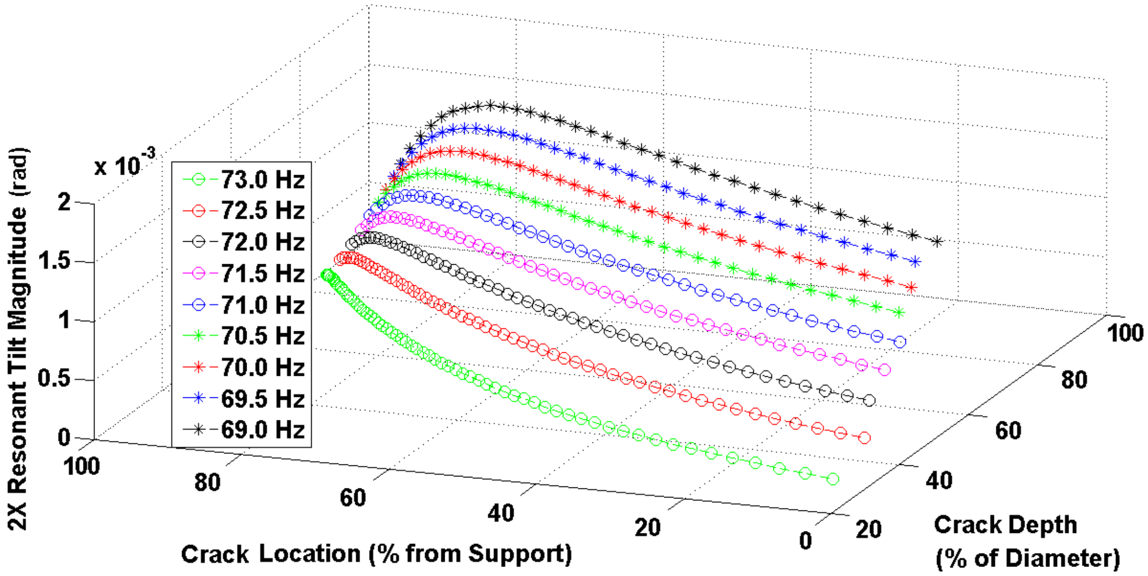

Figure 7.5: Notch Crack: Locus of 2X resonant tilt magnitudes for a range of target 2X resonance frequencies versus notch location and depth

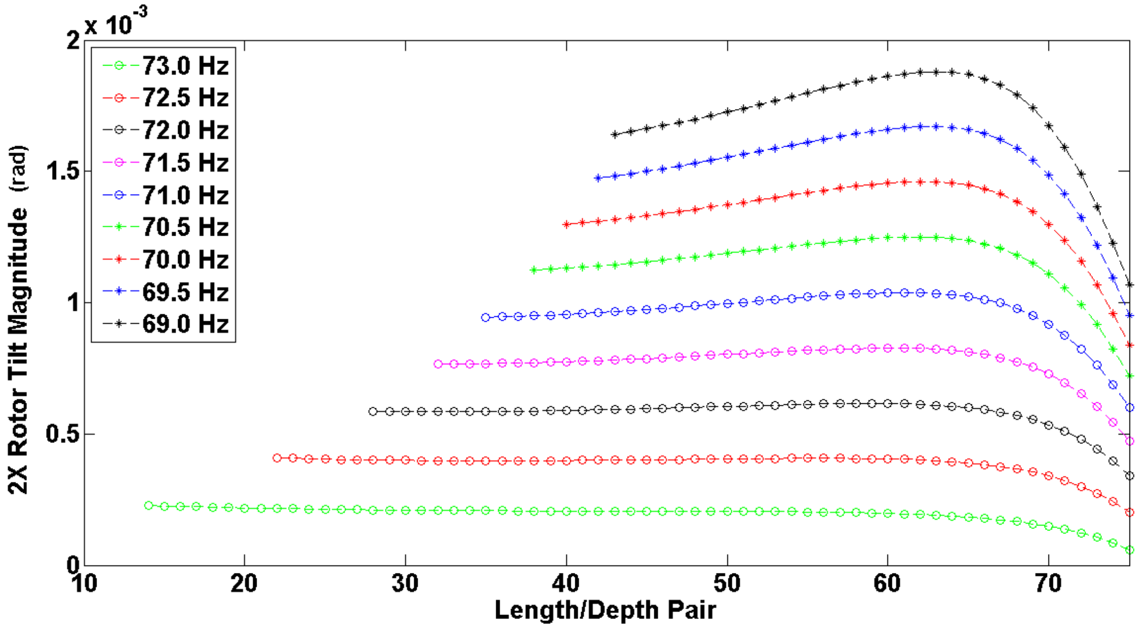

Figure 7.6: Notch Crack: Locus of 2X resonant tilt magnitudes for a range of target 2X resonance frequencies

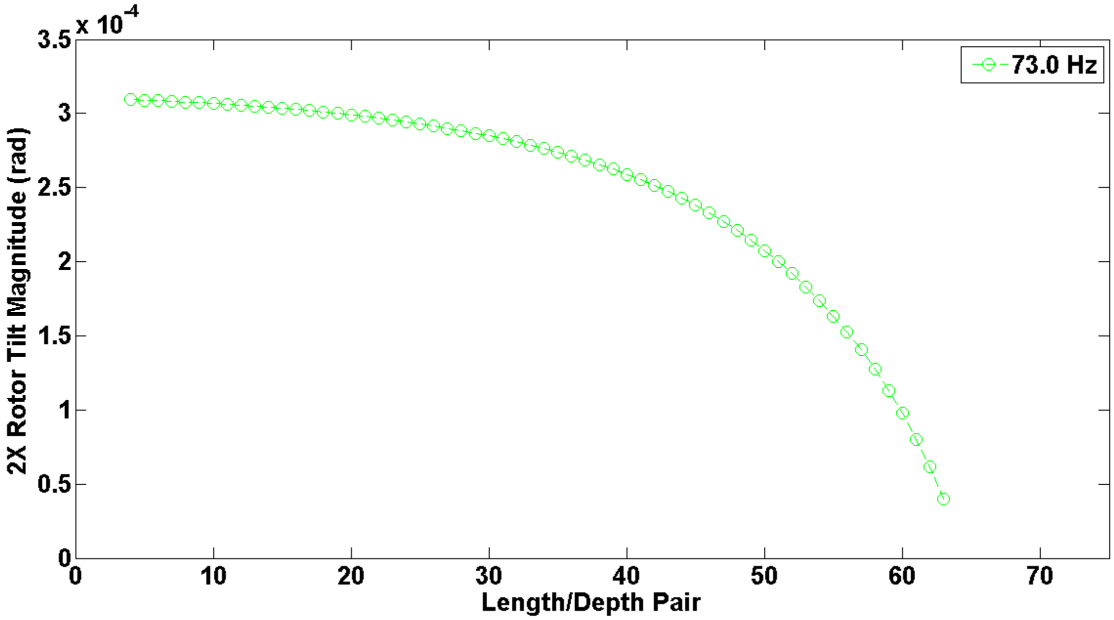

Figure 7.7: Gaping Fatigue Crack: Locus of 2X resonant tilt magnitudes for a target 2X resonance frequency of 73 Hz

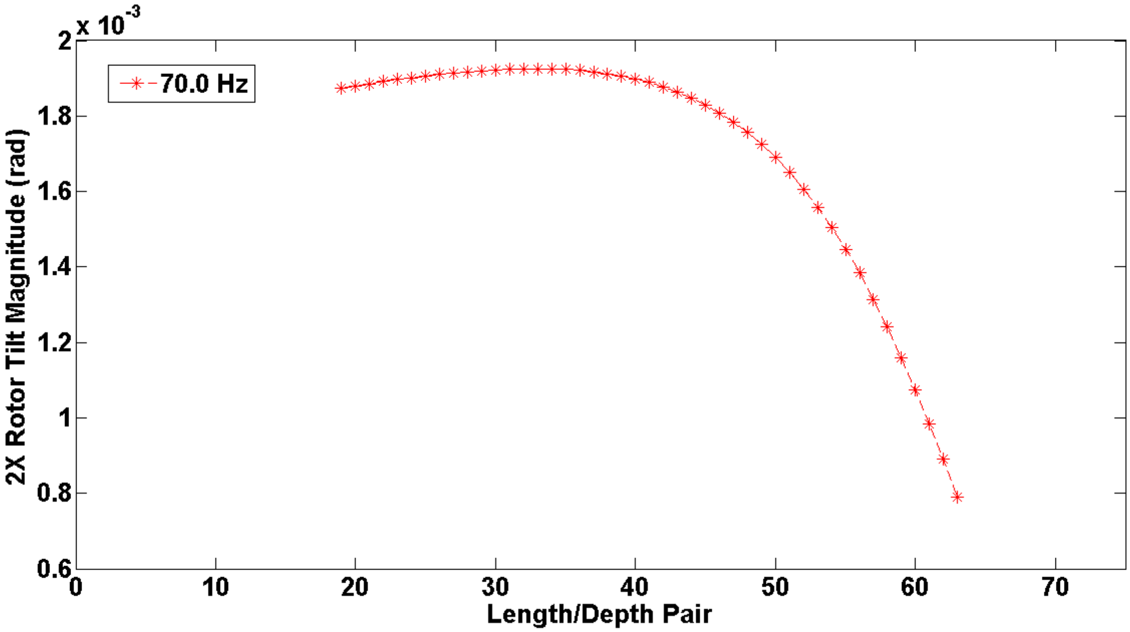

Figure 7.8: Gaping Fatigue Crack: Locus of 2X resonant tilt magnitudes for a target 2X resonance frequency of 70 Hz

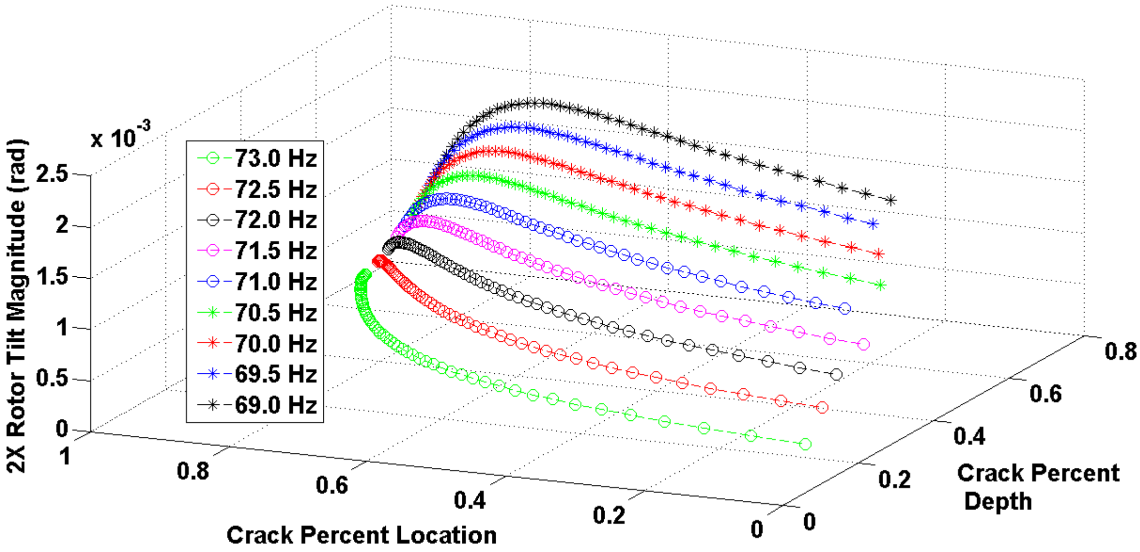

Figure 7.9: Gaping Fatigue Crack: Locus of 2X resonant tilt magnitudes for a range of target 2X resonance frequencies versus crack location and depth

of 2X resonant tilt response is observed. Figure 7.10 provides the same information as Fig. 7.9, but plots the 2X resonant tilt magnitude versus pair number rather than crack location and depth.

The diagnostic procedure is summarized in the following steps:

1. Vary the shaft speed of the system, and record the 2X resonance frequency.
2. Identify the measured 2X resonance frequency contour (this provides a range of possible crack depths and locations).
3. Measure the magnitude of the 2X resonant response.
4. Compare the 2X resonant magnitude to a known locus of magnitudes for the specified 2X resonance frequency contour, generated by a high-fidelity rotor system model.
5. Identify the specific crack depth and location, or provide a reasonable range of estimates.

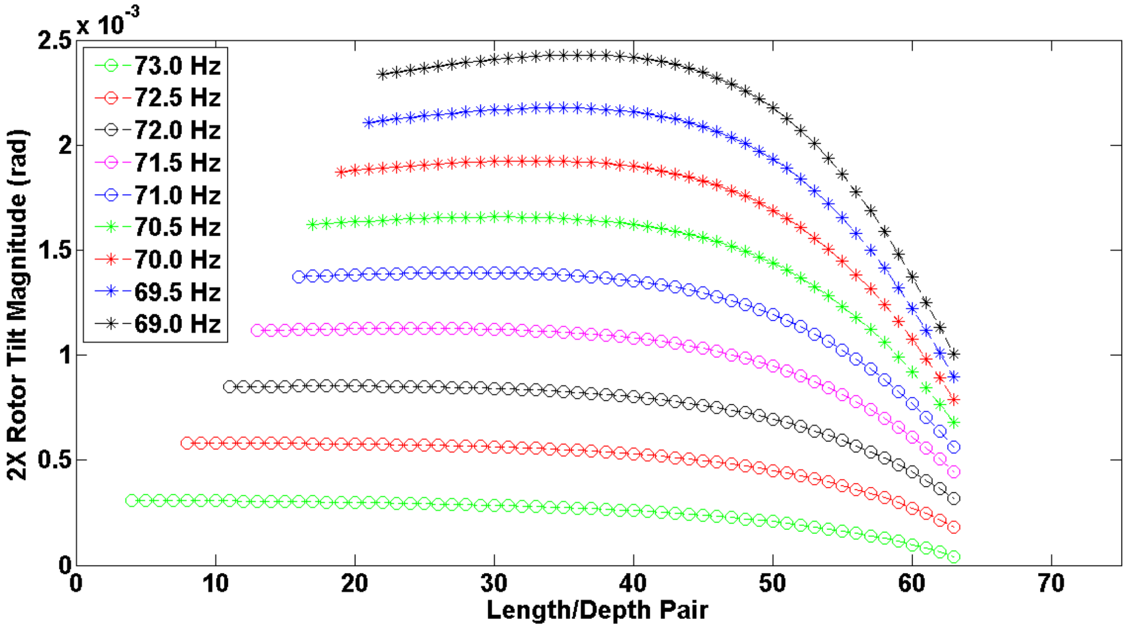

Figure 7.10: Gaping Fatigue Crack: Locus of 2X resonant tilt magnitudes for a range of target 2X resonance frequencies

7.3 Employing Orbital Shapes for Crack Diagnostics

Orbital shapes are often used for rotordynamic condition monitoring, as the orbit shape can indicate the fault type or severity. A gaping fatigue crack is discussed here, though the conclusions are equally valid for the notch. Figures 6.22 - 6.24 provide the rotor's orbit for shaft speeds below, at, and above the 2X resonance frequency, respectively. For each shaft speed, three pairs of crack depth and location are investigated; these pairs are selected because they generate the same 70 Hz resonance frequency.

In all three cases, the lateral orbits are virtually indistinguishable for different pairs of crack location and depth. However, the angular orbits below and above the 2X resonance frequency display prominent deviations. Figure 6.23 indicates that the resonant response is very similar for crack location/depth pairs generating the same 2X resonance frequency. In Section 7.2, only the magnitude of the rotor's 2X harmonic at resonance is employed. By observing the rotor's steady-state orbit below and above the 2X resonance, equal 2X resonance frequency crack pairs can be readily distinguished. If sufficiently accurate instrumentation is available, the radius of the orbit and the orbit offset provides a robust mechanism for distinguishing crack depth from location (along with a measurement of the 2X resonance frequency).

Practically, the deflections observed in Figs. 6.22 and 6.24 are very small. The smallest deflection which can be measured by the available experimental test rig is 0.1 μm. The orbital radii and offsets are clearly either on the threshold of this range or below this range, depending on the specific crack depth/location pair of interest (for the angular orbits, the probes are mounted 12.4 mm from the rotor's center; this radius along with the angle dictates the measured distance of the rotor from the probe). The orbits would perhaps be experimentally separable for shaft speeds closer to resonance, or for a system with increased mass or decreased stiffness.

The orbital mode shapes likewise have diagnostic potential. Recall the angular modes for a gaping fatigue crack below and above resonance (Figs. 6.22b and 6.22b, respectively). The figures clearly indicate the location of the crack by a discontinuity in the angular orbit. Once the location of the crack is identified, a measurement of the 2X resonance frequency could provide the crack depth. However, practical implications limit the use of angular orbital modes for crack diagnostics. First, measurement of the angular deflection along the shaft would require many measurement positions. The cost of these sensors, as well as typically harsh conditions between the shaft and housing, limit the success of mode shape measurement. Furthermore, the angular deflections far from the 2X resonance frequency are minute, requiring very accurate sensors.

7.4 Practical Implications and Shortcomings

Application of the methods discussed above must account for practical implications and various shortcomings. To realize the aforementioned procedure experimentally for diagnosis of crack location and depth, a high degree of accuracy in measurement of the 2X resonance frequency and 2X resonant tilt magnitude must be obtainable, especially to detect shallow cracks. The difficulty in detection of shallow cracks or cracks close to the rotor is qualitatively evident by the large regions displaying little change in Figs. 5.8 and 5.14, and quantitatively evident in Figs. 7.6 and 7.10. The magnitude of the rotor's 2X resonant tilt is much smaller for small cracks, or cracks close to the rotor, than for more severe cracks, and is less sensitive to variations in crack depth and location. Observing Fig. 7.7 for a gaping fatigue crack, tilt magnitudes as small as $0.5(10)^{-4}$ rad must be measured to distinguish the crack location and depth.

Furthermore, the operator must have the ability to access many 2X resonance frequency curves, such as those shown in Figs. 7.6 and 7.10. Either the operator must be proficient enough to execute the required software to generate the curves, or the operator must have access to a sufficiently large database of crack depth and location pairs. Overall, it is shown that a gaping fatigue crack is easier to detect than a notch crack. This is important, as the gaping fatigue crack is more likely to be encountered in real operation.

Most importantly, the model of the system must emulate the actual system to a high degree of fidelity to distinguish crack depth and location realistically. The model must accurately account for damping, support conditions, and the distributed nature of the shaft mass to obtain a reasonable estimate of the 2X resonance frequency and the 2X resonant tilt magnitude as a function of crack location and depth. A sensitivity analysis could be performed to assess the threshold of realistically detectable/diagnosable faults; this task is left to future work.

It is also important to recognize that the results and conclusions given in this work are valid primarily for the overhung rotordynamic system discussed in Chapter 3. The diagnostic procedures rely on the overhung nature of the rotor; because of this, the results may not be even qualitatively similar for other rotor systems (such as the Jeffcott rotor, for example). Crack diagnostics is intimately dependent on the specific system under investigation. Related to the nature of the specific system is the position of the measurement probes. In this case, the probes were placed to measure the rotor's angular deflection. Typically, probes are placed on the bearings. However, the deflection of the shaft is often minuscule at the bearings, leading to a low resolution vibration signal. The probes should be placed such that they extract the largest response possible. It is also observed in this work that cracks closer to the rotor (the measurement point) are much more difficult to detect. The relation between probe placement and the specific fault under investigation should dictate the optimum location of the probes.

The primary goal of the work is not to present a fool-proof method to distinguish crack position and depth, but instead to demonstrate that it is possible to employ sensible, simple, and typical condition monitoring signals to diagnose crack location and depth. Many qualitative aspects of the results presented in this chapter can be employed by a savvy operator to narrow down the possible combinations of crack depth and location when a crack is suspected. In this manner, the dynamic interplay between crack depth and location can be better understood and accounted for in transverse fatigue crack detection and diagnosis.

CHAPTER VIII

CONCLUSIONS AND FUTURE WORK

8.1 Conclusions

The principal motivation of this work is to perform gaping crack diagnostics in an overhung rotordynamic system using simple vibration signatures. The primary signature employed is the profile of the rotor's angular 2X harmonic. Specifically, this work uses the behavior of the 2X harmonic near the 2X resonance frequency as a tool for crack detection and diagnosis. Qualitative and quantitative aspects of the response are sought for crack detection and the diagnosis of the crack's depth and location.

First, a dynamic model of a undamaged rotordynamic system is developed to provide a consistent dynamic model. A linear set of four-degree-of-freedom, coupled differential equations of motion are derived using Newtonian methods in a rotating frame. The degrees of freedom are the lateral displacements of the rotor's center and the rotor's angular tilt. This consistent dynamic model is employed to study the effects of two gaping crack models.

The first of these models is a rectangular-profiled notch crack. A notch has a finite width, and the rectangular profile of the notch prohibits its direct propagation. The stiffness of the notch is determined by its area moments of inertia. The stiffness matrix of a notched Euler-Bernoulli shaft is developed using Castiglianos Theorem. Though rarely appearing in real crack scenarios, notches are often manufactured for experimental crack detection investigations. Even though a notch fails to emulate a true fatigue crack, the notch can serve as an excellent model for qualitatively understanding crack detection and diagnosis.

A more realistic crack model is the gaping fatigue crack. The gaping fatigue crack models a true fatigue crack, as the width of the crack is negligible. A gaping fatigue crack is capable of propagation due to the infinite stress at the crack tip. The stiffness matrix of a shaft displaying at a gaping fatigue crack is derived through application of transfer matrix methods. Analytic results presented in this work indicate that a gaping fatigue crack results in a greater loss of stiffness than a notch of commensurate depth and location.

Transfer matrix techniques provide an expedient method for extracting the rotor's steady-state response. Various transfer matrix methods are discussed in detail, for both inertial and rotating reference frames. A summary of the Real Transfer Matrix is provided. The Real Transfer Matrix employs real-valued coordinates and is best suited for the analysis of orthotropic systems. The Real Transfer Matrix suffers from several inherent deficiencies; most notably, the inability to distinguish forward and backward whirl. The Complex Transfer Matrix overcomes the deficiencies of the Real Transfer Matrix. Specifically, a complex-valued coordinate redefinition is introduced which naturally separates the whirl directions. A detailed discussion of the Complex Transfer Matrix is provided. The Complex Extended Transfer Matrix provides a mechanism to include forcing in the analysis.

Two scenarios for both crack models are investigated. In the first, a fixed-location crack 6.35 mm from the support is analyzed. The analysis is presented for two primary reasons: to investigate the influence of only crack depth, and to provide a benchmark to compare to previous results. The second scenario investigates variations in both crack depth and location.

The system's dynamic characteristics must be understood well to develop a successful crack diagnosis routine. A free response analysis of the equations of motion for both crack models is performed. From the free response analysis, the 2X resonance frequency is obtained versus crack depth and location. The results indicate that the

2X resonance frequency is insufficient for crack diagnosis. The same 2X resonance frequency is obtained for many distinct pairs of crack depths and locations. However, a contour plot of the 2X resonance frequency can provide a lower bound of the crack depth (i.e., a best case scenario), as specific 2X resonance contours originate at specific crack depths.

A forcing function is provided in a rotating frame, including gravity and rotating imbalance. Solution of the forced equations of motion indicates that the 2X harmonic only appears in the presence of a crack and gravity. It is observed that a rotating imbalance only generates a 1X harmonic in steady-state, while a crack solely induces a 2X harmonic. The linearity of the system necessitates that the imbalance does not influence the 2X harmonic, and vice versa. A transient solution of the equations of motion demonstrates that the 2X resonance occurs when the 2X harmonic intersects a system eigenvalue. Furthermore, the results indicate that the 2X harmonic's magnitude is minute when the shaft speed is far from the 2X resonance frequency. Consequently, crack detection and diagnosis is difficult when the shaft speed is far from the 2X resonance frequency. Practical crack condition monitoring necessitates that the operator be free to vary the shaft speed across the 2X resonance frequency. Transfer matrix methods are employed to extract the rotor's steady-state 2X angular response versus shaft speed. The magnitude of the 2X resonant tilt magnitude is provided versus crack depth and location.

Two unique sources of information are presented to distinguish two crack parameters. The analytic results (i.e., contour plots of 2X resonant frequency and 2X resonant magnitude) demonstrate that one measurement is insufficient for separation of crack depth and location. A procedure for crack diagnosis is provided relying on the 2X resonant frequency and angular 2X resonant magnitude. Measurement of the 2X resonance frequency restricts the possible values of crack location and depth to a certain locus of pairs. The magnitude of the measured angular 2X resonance is compared to the crack depth and locations comprising the measured 2X resonance frequency contour. Following comparison, the crack depth and location is either known or limited to a certain range.

Rotor orbits are provided for several crack depth and location pairs giving the same 2X resonance frequency. Shaft speeds below resonance, at resonance, and above resonance are investigated. In all cases, the 2X steady-state response induces a circular orbit. Dynamic effects dominate at resonance, and the radius of the orbit is much greater than the static deflections. Hence, the orbits for both the lateral and angular response are primarily indistinguishable concentric circles, even for very different crack depth/location pairs. The angular orbits above and below resonance are distinctly different for different pairs of crack depth and location pairs. However, the magnitude of the orbit is small, as the shaft speed is removed from resonance. The accuracy of the instrumentation therefore dictates the ability to employ orbits as crack diagnostic tools. The concept of steady-state orbits is extended to provide the orbital mode shapes at various shaft speeds. It is obvious that the angular mode could hypothetically provide a valuable tool for diagnosing crack location. Unfortunately, practical limitations mostly preclude the ability to incorporate real-time mode monitoring of a real rotordynamic system.

In all cases, it is found that a gaping fatigue crack introduces a greater loss of stiffness than a notch placed at a commensurate location. Hence, smaller gaping fatigue cracks result in greater changes in the measurable parameters (2X resonant frequency and magnitude) as compared to a notch. The larger change in parameters allows for smaller gaping fatigue cracks to be realistically detected than notches of equivalent depth. This result is important, as it implies real fatigue cracks are easier to diagnose than notches of equivalent depth and location.

The procedures highlighted above do not propose a panacea for crack diagnosis;

several shortcomings must be discussed and contextualized when attempting crack diagnosis. First, and most importantly, the accuracy of the model is imperative towards comparing measured results to analytic results, as diagnosis of crack parameters relies on the ability to distinguish relatively small changes in the 2X resonance frequency and tilt magnitude. Many effects, such as stiffness, damping, and support conditions, must be precisely represented in the system model. Likewise, the instrumentation employed to measure the dynamic response of the rotor must possess a high degree of accuracy to detect small variations in the signals of interest. Furthermore, the results presented in this work are valid only for an overhung rotordynamic system; analysis of different systems would likely result in vastly different results and conclusions.

As with all crack detection and diagnosis routines, the results presented in this work indicate that shallow cracks are difficult to detect and diagnose. Moreover, the results presented herein demonstrate that cracks close to the rotor (or the measurement location, more generally) can be very difficult to detect. However, it is likely that these cracks present a less severe impact on the system, as the relatively unchanged 2X resonance frequency and 2X resonant tilt magnitude are indicative of a smaller loss of stiffness. Understanding the interplay between crack location and depth is essential. To disregard or over-simplify the effect of crack location presents a grossly oversimplified model incapable of diagnosing real transverse fatigue cracks. Crack location and depth play an equally important role in determining the system's stiffness.

8.2 Future Work

The most important consideration for future work is inclusion of crack breathing behavior. Breathing behavior introduces shaft speed harmonics in addition to the 2X, such as the 1X and the 3X harmonics. It is plausible that this increase in information provides more robust crack diagnosis routines. The analytic techniques required to investigate the dynamics of a cracked system displaying breathing behavior are significantly more involved than those used to investigate a gaping crack. Foremost, transfer matrix techniques would no longer be applicable, as the system's stiffness even in a rotating frame would contain at best linear time periodic coefficients. Numeric solution of the nonlinear equations would be required to obtain the rotor's steady-state response.

It is well known that transverse cracks introduce coupling between the lateral, axial, and torsional degrees of freedom. This coupling phenomena has been previously employed to detect transverse fatigue cracks [28, 31, 44]. The equations of motion given in this analysis should be expanded to include additional torsional and axial degrees of freedom, as the coupling is a robust crack indicator.

Many real world turbomachinery systems are simply supported rather than overhung. The analysis could be repeated for a simply supported case, though measurement of the rotors angular response would be experimentally challenging. A more realistic approach would be to incorporate fluid film bearings at the support, and measure the corresponding deflection of the shaft at the bearing. It is hypothesized that the difference in signals measured at both bearings could be used to diagnose the crack depth and location.

A finite element method should be developed to incorporate the aforementioned changes (breathing behavior, coupling, and fluid film effects). Fortunately, a wealth of research exists on the application of finite elements for rotating cracked shafts. The use of a finite element method would allow for the inclusion of a wide array of different tribo-elements and nonlinear effects. As such, the effects of simultaneous multiple faults could be assessed (such as seal face contact, breathing cracks, shaft misalignment, etc.). Multiple fault detection is important, as real rotordynamic systems are susceptible to a wide array of potential faults.

An improvement in calculating the true compliance of a real fatigue crack could provide more accurate crack compliance predictions for deep cracks. The crack compliance coefficients determined via the strain energy release rate are local; for deep cracks, a portion of the cracked surface may no longer be considered local. A hybrid model where a portion of the crack remains open while a portion experiences breathing could provide more accurate results for deep cracks.

An important reason for performing crack diagnostics is to assess the remaining lifetime of the machine (prognostics). To fully understand crack prognostics, the phenomenon of crack propagation must be understood. Crack growth is typically described in relation to the parameter da/dN, which is a measure of the crack growth per cycle. Knowledge of this parameter as it relates to the depth and location of the crack could provide meaningful prognostic information. An estimate of the remaining cycles until failure allows the operator to keep the machine in operation while plans are made to either repair or replaced the cracked shaft.

APPENDIX A

DYNAMICS OF THE ROTOR: ACCELERATION AND ANGULAR MOMENTUM

Formulation of the rotor's acceleration and angular momentum are critical to the dynamic model of the overhung rotordynamic system. The acceleration and angular momentum of the rotor are developed in an inertial and rotating reference frame.

A.1 Acceleration of the Center of Mass

A.1.1 Inertial Reference Frame

Figure 3.3 provides the rotor plane and degrees of freedom, and is reproduced here in Fig. A.1 for clarity (see Fig. 3.2 for a presentation of the reference frames). The position of the rotor's center of mass C with respect to origin O (the undeflected location of the rotor's center) is given by the position vector

$$\bar{r}_{C/O} = u_\xi \hat{e}_\xi + u_\eta \hat{e}_\eta, \tag{A.1}$$

where $\hat{e}_\xi$ and $\hat{e}_\eta$ are unit vectors in the inertial reference frame. Since the reference frame is inertial, the second derivative of Eq. A.1 is

$$\ddot{\bar{r}}_{C/O} = \ddot{u}_\xi \hat{e}_\xi + \ddot{u}_\eta \hat{e}_\eta. \tag{A.2}$$

Equation A.2 is used directly to obtain the dynamic forces $m\bar{a}_C$ acting on the rotor in the inertial reference frame.

A.1.2 Rotating Reference Frame

The general acceleration of one point P_2 with respect to another point P_1 is

$$\bar{a}_{P_2} = \bar{a}_{P_1} + \dot{\bar{\omega}} \times \bar{r}_{P_2/P_1} + \bar{\omega} \times \left(\bar{\omega} \times \bar{r}_{P_2/P_1}\right) + 2\bar{\omega} \times \left(\dot{\bar{r}}_{P_2/P_1}\right)_{xyz} + \left(\ddot{\bar{r}}_{P_2/P_1}\right)_{xyz} \tag{A.3}$$

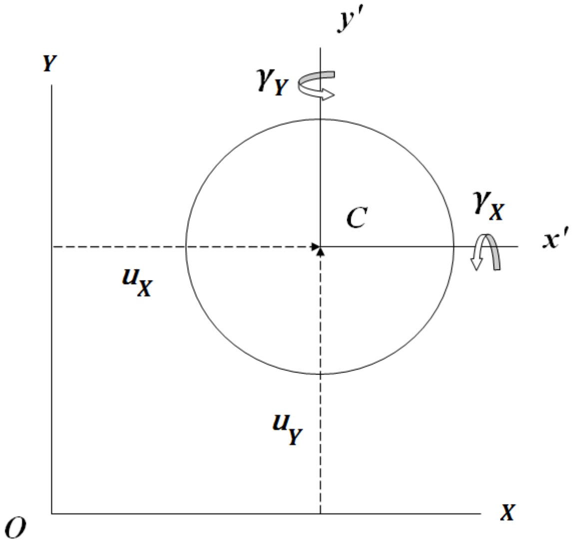

Figure A.1: Rotor degrees of freedom

where $\bar{\omega}$ is the angular velocity of the rotating reference frame (in this case, $\bar{\omega} = n\hat{K}$), $\bar{r}_{P_2/P_1}$ is a position vector from point P_1 to P_2, and the subscript XYZ denotes the motion as observed by an observer in the XYZ frame. Point O is selected as the reference point for determining the acceleration of point C, as O is stationary and thus has zero velocity and acceleration. Using these points in a reference frame rotating at constant n, Eq. A.3 reduces to

$$\bar{a}_C = \bar{n} \times \left(\bar{n} \times \bar{r}_{C/O}\right) + 2\bar{n} \times \left(\dot{\bar{r}}_{C/O}\right)_{XYZ} + \left(\ddot{\bar{r}}_{C/O}\right)_{XYZ}, \tag{A.4}$$

where the position vector $\bar{r}_{C/O}$ in the rotating frame XYZ is

$$\bar{r}_{C/O} = u_X \hat{I} + u_Y \hat{J}. \tag{A.5}$$

Evaluation of Eq. A.4 provides the components of the acceleration of the center of mass, C, in the rotating reference frame:

$$\begin{aligned} a_C^X &= \ddot{u}_X - n^2 u_X - 2\,n\,\dot{u}_Y \\ a_C^Y &= \ddot{u}_Y - n^2 u_Y + 2\,n\,\dot{u}_X \\ a_C^Z &= 0 \end{aligned} \tag{A.6}$$

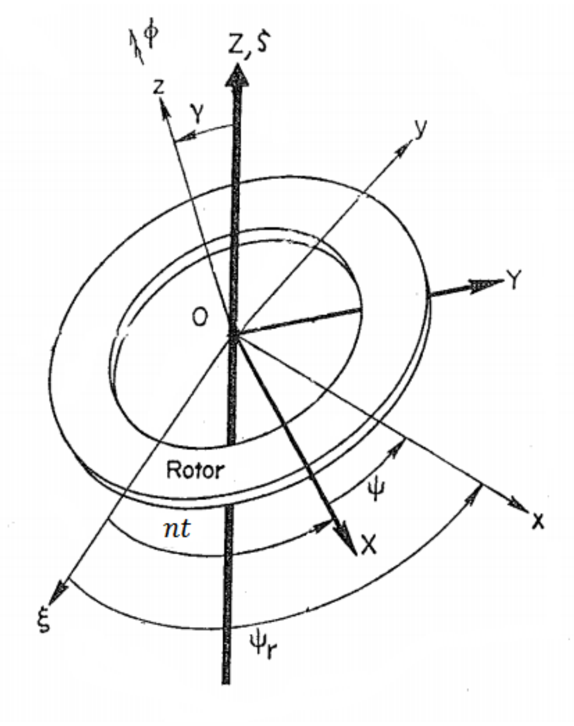

Figure A.2: Rotating reference frames

A.2 Angular Momentum

A.2.1 Rotating Reference Frame

Green and Etsion [5] first provide the general angular momentum of the flexibly mounted rotor. Green [6] expands the formulation and employs Lagrange's method to derive the rotor equations of motion. Several reference frames are crucial towards understanding the origin of the angular momentum. These reference frames, shown in Fig. A.2, are the following:

1. $\xi\eta\zeta$: Inertial reference frame, fixed at the undeflected location of the rotor's geometric center, O (where C is the rotor's center).
2. XYZ: Rotating reference frame where X and Y remain perpendicular to the shaft. The frame is still attached at the rotor's geometric center, and rotates with a hypothetical undeflected shaft at frequency n.

3. $x_1y_1z_1$: Frame shifted from XYZ by the relative precession ψ about axis Z (not shown in Fig. A.2).
4. xyz: Rotating reference frame shifted from $x_1y_1z_1$ by the nutation γ, which occurs about the x axis (and the x_1 axis). The axes x and y remain in the plane of the rotor's face, though the frame is not fixed to the rotor (the rotor spins relative to the frame at $\dot{\phi}$).

Several crucial rotations must likewise be defined:

1. nt: The angle between ξ and X, where n is the shaft speed.
2. ψ: The relative precession angle between x and X.
3. ψ_r: The absolute precession angle, defined such that $\psi_r = \psi + nt$.
4. γ: The nutation of the rotor about the x axis.
5. ϕ: The spin angle of the rotor relative to the xyz frame.

Green and Etsion [5] develop a transmission law stating that

$$\dot{\phi} = -\dot{\psi}, \tag{A.7}$$

which is true so long as $\gamma^2 << 1$. Essentially, the statement requires that all points on the rotor must return to their original position following one revolution; this conclusion is visualized by Green [6] through the use of space and body cones. In addition, it can be shown that

$$\dot{\psi}_r = \dot{\psi} + n. \tag{A.8}$$

The angular momentum of the rotor's center of mass, $\{h_C\}$, is given by

$$\{h_C\} = [I_C]\{\lambda\}, \tag{A.9}$$

where $\{\lambda\}$ is the absolute angular velocity of the rotor and $[I_C]$ is the inertia tensor. The inertia tensor is most easily defined in the xyz frame, as the rotor is symmetric with regard to the frame. The absolute angular velocity is the sum of the rotor's precession ($\dot{\bar{\psi}}_r$), nutation ($\dot{\bar{\gamma}}$), and spin ($\dot{\bar{\phi}}$) components:

$$\bar{\lambda}^{xyz} = \dot{\bar{\psi}}_r^{xyz} + \dot{\bar{\gamma}}^{xyz} + \dot{\bar{\phi}}^{xyz}, \tag{A.10}$$

where the superscript xyz indicates that the vectors are formed in the xyz reference frame. Evaluating Eq. A.10 gives:

$$\bar{\lambda}^{xyz} = \dot{\gamma}\hat{x} + \dot{\psi}_r \sin\gamma \hat{y} + \left[n + \dot{\psi}_r(\cos\gamma - 1)\right]\hat{z}, \tag{A.11}$$

where $\hat{x}, \hat{y}$ and $\hat{z}$ denote unit vectors in the xyz frame. The angular momentum of the rotor is then found to be:

$$\{h_C\}^{xyz} = \left\{\begin{array}{c} I_t\dot{\gamma} \\ I_t\dot{\psi}_r \sin\gamma \\ I_p\left[n + \dot{\psi}_r(\cos\gamma - 1)\right] \end{array}\right\}. \tag{A.12}$$

Defining this result in the XYZ frame is desirable, as the generalized degrees of freedom are also defined in XYZ. Hence, several rotation transformations are necessary. First, a rotation transformation is developed which moves a general vector $\{A\}$ from XYZ to $x_1y_1z_1$:

$$\{A\}^{x_1y_1z_1} = [R_1]\{A\}^{XYZ} \tag{A.13}$$

where, since the rotation is of magnitude ψ and about the Z axis,

$$[R_1] = \begin{bmatrix} \cos\psi & \sin\psi & 0 \\ -\sin\psi & \cos\psi & 0 \\ 0 & 0 & 1 \end{bmatrix}. \tag{A.14}$$

Similarly,

$$\{A\}^{xyz} = [R_2]\{A\}^{x_1y_1z_1}, \tag{A.15}$$

where, since the rotation is of magnitude γ and about the x_1 axis,

$$[R_2] = \begin{bmatrix} 1 & 0 & 0 \\ 0 & \cos\gamma & \sin\gamma \\ 0 & -\sin\gamma & \cos\gamma \end{bmatrix}. \tag{A.16}$$

The angular momentum of the rotor is thus found through application of these transformations:

$$\{h_C\}^{XYZ} = [R_1]^T [R_2]^T \{h_C\}^{xyz} . \tag{A.17}$$

The final expression is linearized by assuming $\gamma^2 << 1$, such that $\sin\gamma \simeq \gamma$ and $\cos\gamma \simeq 1$. In addition, tilts in the X and Y directions (γ_X and γ_Y, respectively) are found from the following relations:

$$\gamma_X = \gamma \cos\psi \tag{A.18}$$

$$\gamma_Y = \gamma \sin\psi . \tag{A.19}$$

These relations can be verified using the previously given rotation transformations. To find $\dot{\gamma}_X$ and $\dot{\gamma}_Y$, Eqs. A.18 and A.19 are differentiated:

$$\dot{\gamma}_X = \dot{\gamma} \cos\psi - \gamma \sin\psi\dot{\psi} \tag{A.20}$$

$$\dot{\gamma}_Y = \dot{\gamma} \sin\psi + \gamma \cos\psi\dot{\psi} . \tag{A.21}$$

The terms $\ddot{\gamma}_X$ and $\ddot{\gamma}_Y$ are likewise found via differentiation of Eqs. A.20 and A.21. Substituting Eqs. A.18 - A.21 into the result from Eq. A.17 gives the following form of the angular momentum following linearization:

$$\begin{aligned} h_{C,X} &= I_t(\dot{\gamma}_X - n\gamma_y) + I_p n \gamma_Y \\ h_{C,Y} &= I_t(\dot{\gamma}_Y + n\gamma_x) - I_p n \gamma_X \\ h_{C,Z} &= I_t(\dot{\psi} + n)^2 \gamma^2 + I_p n . \end{aligned} \tag{A.22}$$

However, keep in mind that the dynamic moments on the rotor must be evaulated prior to linearization. The dynamic moments are calculated from

$$\sum \bar{M}_C = \frac{d\bar{h}_C}{dt} = \frac{\partial \bar{h}_C}{\partial t} + \bar{n} \times \bar{h}_C , \tag{A.23}$$

where $\bar{n}$ is the angular velocity of the rotating frame XYZ. Evaluation of Eq. A.23 gives

$$\begin{aligned} M_x &= I_t\left(\ddot{\gamma}_X - n^2\gamma_X - 2n\dot{\gamma}_Y\right) + I_p\left(n\dot{\gamma}_Y + n^2\gamma_X\right) \\ M_y &= I_t\left(\ddot{\gamma}_Y - n^2\gamma_Y + 2n\dot{\gamma}_X\right) - I_p\left(n\dot{\gamma}_X - n^2\gamma_Y\right) \ , \\ M_z &= O(\gamma^2) \approx 0 \end{aligned} \tag{A.24}$$

where M_z is negligible, as it is of order γ^2.

A.2.2 Inertial Reference Frame

The inertial dynamic moments are similarly obtained by recognizing that the angular momentum can be transferred directly from $x_1y_1z_1$ to $\xi\eta\zeta$ by rotating through the angle ψ_r. The tilts γ_ξ and γ_η are then defined by

$$\gamma_\xi = \gamma \sin \psi_r \tag{A.25}$$

$$\gamma_\eta = \gamma \cos \psi_r. \tag{A.26}$$

Repeating an analogous process to that described above gives the following inertial frame dynamic moments, as derived by Green [67]:

$$\begin{aligned} M_\xi &= I_t \; \ddot{\gamma}_\xi + I_p n \dot{\gamma}_\eta \\ M_\eta &= I_t \; \ddot{\gamma}_\eta - I_p n \dot{\gamma}_\xi \\ M_\zeta &= 0. \end{aligned} \tag{A.27}$$

APPENDIX B

AREA MOMENTS OF INERTIA

The notched shaft stiffness depends on the area moments of inertia of the notch cross-section. The notch cross-section is shown in Fig. B.1, where the notch depth is a and its half-width is b. The centroid is designated $\bar{C}$. The area moments of inertia $\tilde{I}_x^C$ and $\tilde{I}_y^C$ about the x and y axes are

$$\tilde{I}_x^C = \int_A y^2 dx\, dy \tag{B.1}$$

and

$$\tilde{I}_y^C = \int_A x^2 dx\, dy, \tag{B.2}$$

which are calculated about the center of the uncracked cross-section, where the reference frame is attached. Evaluation of Eqs. B.1 and B.2 leads to expressions for the area moments of inertia of the notch cross-section:

$$\tilde{I}_x^C = \frac{1}{4}\left(R^3 - R^2 a\right)\mu^{1/2} - \frac{1}{2}\left(R-a\right)\mu^{3/2} + \frac{R^4}{4}\tan^{-1}\left(\frac{R-a}{\mu^{1/2}}\right) + \frac{1}{8}\pi R^4 \tag{B.3}$$

$$\tilde{I}_y^C = \frac{1}{6}\left(R-a\right)\mu^{3/2} + \frac{1}{4}\left(R^3 - R^2 a\right)\mu^{1/2} + \frac{R^4}{4}\tan^{-1}\left(\frac{R-a}{\mu^{1/2}}\right) + \frac{1}{8}\pi R^4 \tag{B.4}$$

where

$$\mu = 2Ra - a^2. \tag{B.5}$$

The parallel axis theorem is now employed to transform the area moments of inertia from the center of the uncracked shaft (point C) to the centroid of the notch section. As the centroid is along the y axis, the centroidal area moment of inertia about y is the following:

$$I_y = \tilde{I}_y^C. \tag{B.6}$$

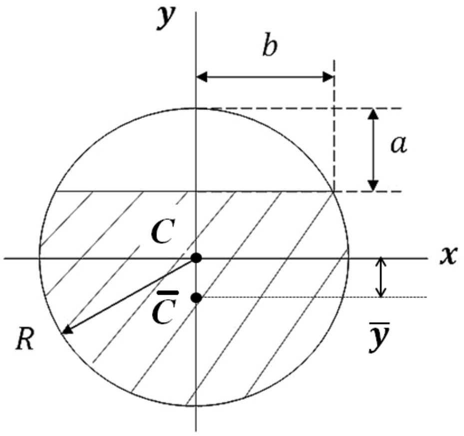

Figure B.1: Notch cross-section

The parallel axis theorem gives the area moment of inertia I_x:

$$I_x = \tilde{I}_x^C - A\bar{y}^2, \tag{B.7}$$

where A is the area of the notch cross-section and $\bar{y}$ is the distance from the center of the uncracked section to the centroid of the notch section. These parameters are found to be

$$A = (R - a)\,\mu^{1/2} + R^2 \sin^{-1}\left(1 - \frac{a}{R}\right) + \frac{\pi R^2}{2} \tag{B.8}$$

and

$$\bar{y} = \frac{2}{3A}\mu^{3/2}. \tag{B.9}$$

As expected, the expression for the area of the uncracked cross-section is equal to that of a half circle when the notch depth is 50%. Furthermore, the location of the centroid reduces to the center of the circular cross-section when the depth of the notch is zero. The area moments of inertia about the centroid of the notch cross-section are evaluated and plotted in Fig. B.2, being normalized by the area moment of inertia of the uncracked cross-section. As expected, the normalized area moments of inertia are equal to those of an uncracked circular cross-section for a zero-depth notch and decay to zero as the depth of the notch becomes equal to the diameter of the shaft. In addition, the area moments of inertia were calculated by numerically integrating

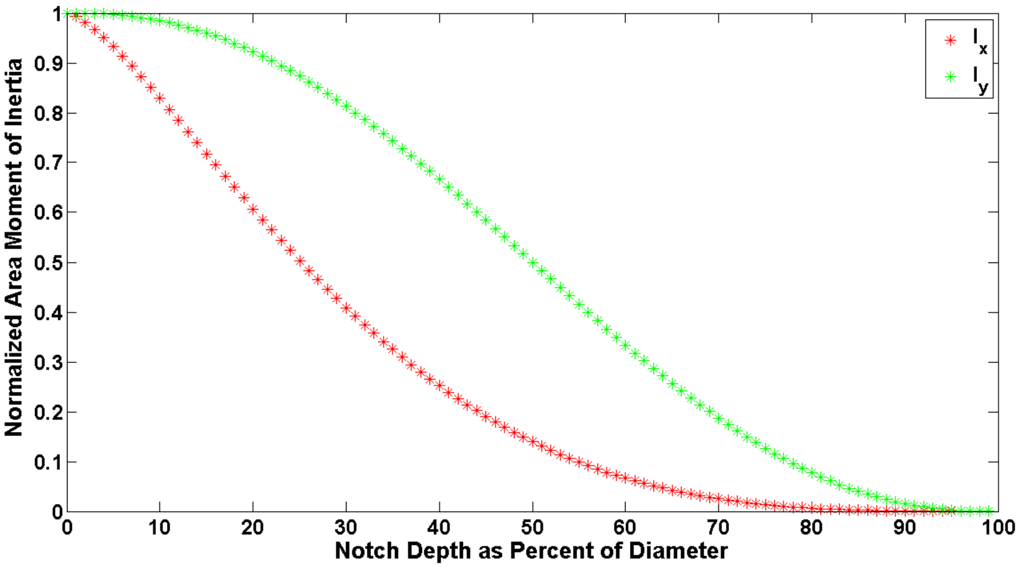

Figure B.2: Normalized notch area moments of inertia

Eqs. B.1 and B.2. The numerically-determined area moments of inertia were found to be equal to those obtained analytically using Eqs. B.3 and B.7.

APPENDIX C

NOTCH COMPLIANCE

The compliance matrix of the notched shaft is determined using Castigliano's Theorem. For brevity, only two example calculations are presented here, with the remainder following an analogous procedure. The first example gives the linear deflection of the shaft caused by a force, while the second gives the angular deflection caused by a force. For convenience, the coordinate system is attached to the free end of the shaft, with the z-axis pointing towards the cantilevered end; this assists in reducing the complexity of the calculations. According to Castigliano's Theorem, the linear deflection δ_y due to an applied load F_y at the end of the shaft (i.e., the rotor) and in the same direction is

$$\delta_y = \frac{\partial U}{\partial F_y} = \int_0^L \frac{M_x^{F_y}}{EI_x} \left(\frac{\partial M_x^{F_y}}{\partial F_y} \right) dz. \tag{C.1}$$

The first step in determining the deflection is to obtain a closed-form expression of the internal bending moment generated within the shaft segment. A shaft segment with applied loading and corresponding coordinate system is shown in Fig. C.1 to assist in this task. The internal bending moment induced by application of a force in

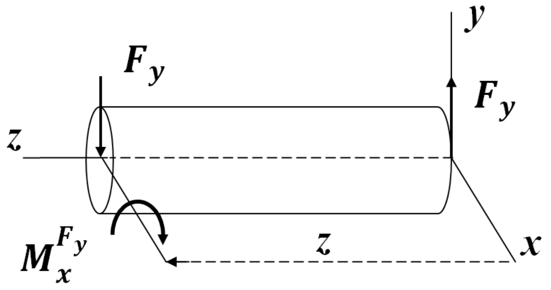

Figure C.1: Internal bending moments in the shaft due to applied load F_y

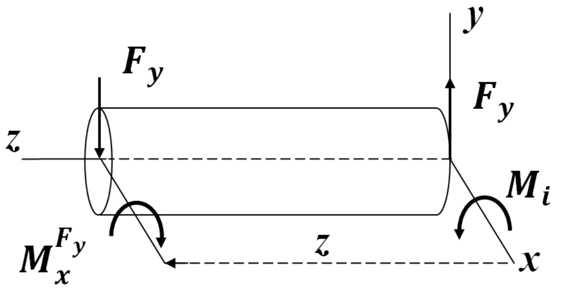

Figure C.2: Internal bending moments in the shaft due to applied loads F_y and M_i

the y direction is found through static balance to be

$$M_x^{F_y} = F_y z, \tag{C.2}$$

where z is the distance along the z-axis to the cross-sectional plane of interest. The concept is now applied to the full notched shaft shown in Fig. 3.4. Substitution of Eq. C.2 into Eq. C.1 yields

$$\delta_y^{F_y} = \int_0^{L_2} \frac{F_y z}{E I_x}(z)dz + \int_{L_2}^{L_2+L_c} \frac{F_y z}{E I_x^C}(z)dz + \int_{L_2+L_C}^{L_2+L_c+L_1} \frac{F_y z}{E I_x}(z)dz, \tag{C.3}$$

where I_x and I_x^C are the area moments of inertia of the uncracked and notched cross-sections, respectively. Evaluation of the integrals in Eq. C.3 provides the following expression for the deflection δ_y:

$$\delta_y^{F_y} = \frac{F_y}{3E}\left(\frac{L_2^3}{I_x} + \frac{(L_2+L_C)^3 - L_2^3}{I_x^C} + \frac{(L_2+L_C+L_1)^3 - (L_2+L_c)^3}{I_x}\right). \tag{C.4}$$

Note than when either the area moments of inertia are equal or the width of the notch is set to zero, Eq. C.4 reduces to an undamaged cantilevered Euler-Bernoulli beam. The process for obtaining angular deflections due to applied moments is applied analogously.

Determining the angular deflection caused by a force or the linear deflection caused by a moment is more involved. Castigliano's Theorem is only valid for finding deflections in the same direction as the applied force. To compensate for this caveat, a virtual force or moment in the direction of the desired displacement must be applied. This virtual load is then set to zero after all derivatives in Eqs. 3.7 and 3.8 are evaluated. This process is demonstrated in the following example. Figure C.2 displays a shaft segment with an applied force F_y. Since the angular deflection about the x-axis is desired, a virtual moment must be applied about that axis. The virtual moment M_i is shown in Fig. C.2. The internal bending moment generated by this system of real and virtual loads is

$$M_x^{F_y} = F_y z + M_i. \tag{C.5}$$

The angular deflection found using Eq. 3.8 is

$$\gamma_x^{F_y} = \int_0^L \frac{M_x^{F_y}}{EI_x} \left(\frac{\partial M_x^{F_y}}{\partial M_i} \right) dz. \tag{C.6}$$

Following evaluation of the derivative, the virtual applied moment M_i is set to zero. Piece-wise integration over the length of the notched beam shown in Fig. 3.4 gives

$$\gamma_x^{F_y} = \int_0^{L_2} \frac{F_y z}{EI_x}(1)dz + \int_{L_2}^{L_2+L_c} \frac{F_y z}{EI_x^C}(1)dz + \int_{L_2+L_C}^{L_2+L_c+L_1} \frac{F_y z}{EI_x}(1)dz. \tag{C.7}$$

Evaluation of the above integral relates the applied force F_y and the angular deflection γ_x according to:

$$\gamma_x^{F_y} = \frac{F_y}{2E} \left(\frac{L_2^2}{I_x} + \frac{(L_2+L_C)^2 - L_2^2}{I_x^C} + \frac{(L_2+L_C+L_1)^2 - (L_2+L_c)^2}{I_x} \right). \tag{C.8}$$

Once the deflection at the rotor is found, the compliance coefficient is found by setting the corresponding applied load to unity. The remainder of the compliance matrix terms are analogously found, where the super-subscript indicates either axis x or y:

$$C_{11_j} = \frac{1}{3E} \left(\frac{L_2^3}{I_j} + \frac{(L_2+L_C)^3 - L_2^3}{I_j^C} + \frac{(L_2+L_C+L_1)^3 - (L_2+L_C)^3}{I_j} \right) \tag{C.9}$$

$$C_{12_j} = C_{21_j} = \frac{1}{2E} \left(\frac{L_2^2}{I_j} + \frac{(L_2+L_C)^2 - L_2^2}{I_j^C} + \frac{(L_2+L_C+L_1)^2 - (L_2+L_C)^2}{I_j} \right) \tag{C.10}$$

$$C_{22_j} = \frac{1}{E}\left(\frac{L_2}{I_j} + \frac{L_C}{I_j^C} + \frac{L_1}{I_j}\right). \tag{C.11}$$

The first subscript (e.g., '11') represents the nature of the element; '11' would represent a direct compliance term relating a deflection to an applied linear force. The subscript '22' denotes the direct relationship between angular deflections and applied moments. Coupling terms are likewise recognized through the use of a subscript such as '12' or '21'. Arranging these coefficients into the general compliance matrix gives

$$\left\{\begin{array}{c} u_x \\ u_y \\ \gamma_x \\ \gamma_y \end{array}\right\} = \begin{bmatrix} C_{11_y} & 0 & 0 & C_{12_y} \\ 0 & C_{11_x} & -C_{12_x} & 0 \\ 0 & -C_{21_x} & C_{22_x} & 0 \\ C_{21_y} & 0 & 0 & C_{22_y} \end{bmatrix} \left\{\begin{array}{c} F_x \\ F_y \\ M_x \\ M_y \end{array}\right\}. \tag{C.12}$$

As expected, the aforementioned terms of the compliance matrix reduce to those of a constant cross-section cantilevered beam when either the area moments of inertia are equivalent or when the width of the notch L_C is set to zero (see Fig. 4.3 for a physical intuition concerning the compliance matrix).

APPENDIX D

GAPING FATIGUE CRACK COMPLIANCE

An overhung shaft displaying a gaping fatigue crack is shown below in Fig. D.1, with a set of applied loads on the free end. The compliance matrix of the cracked overhung shaft is found using the transfer matrix. To accomplish this, the crack compliance matrix (Eq. 3.18) must first be rearranged into a transfer matrix form:

$$[F_{crack}] = \begin{bmatrix} 1 & 0 & 0 & -c_{22} & 0 & 0 & 0 & 0 \\ 0 & 1 & c_{44} & 0 & 0 & 0 & c_{45} & 0 \\ 0 & 0 & 1 & 0 & 0 & 0 & 0 & 0 \\ 0 & 0 & 0 & 1 & 0 & 0 & 0 & 0 \\ 0 & 0 & 0 & 0 & 1 & 0 & 0 & -c_{33} \\ 0 & 0 & c_{54} & 0 & 0 & 1 & c_{55} & 0 \\ 0 & 0 & 0 & 0 & 0 & 0 & 1 & 0 \\ 0 & 0 & 0 & 0 & 0 & 0 & 0 & 1 \end{bmatrix}_{8\times 8} . \tag{D.1}$$

The stiffness of the system is gleaned through three elements: the left-most Euler-Bernoulli beam segment L_1, the compliance introduced by the crack, and the beam

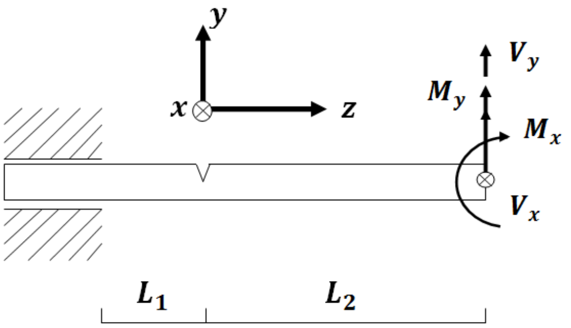

Figure D.1: Overhung shaft displaying gaping fatigue crack and applied loadings segment of length L_2 to the right of the crack. The overall transfer matrix is formed by multiplying the individual element transfer matrices:

$$[U] = [F_2][F_{crack}][F_1] \tag{D.2}$$

such that

$$\{S\}^{AP} = [U]\{S\}^{SU}, \tag{D.3}$$

where AP denotes the applied boundary conditions on the free end, and SU denotes the support boundary conditions generated at the cantilevered end. The goal is to find the displacements at the free end induced by the loading conditions at that location. The state vector of boundary conditions on the free end, including applied loadings, is:

$$\{S\} = \left\{ \begin{array}{cccccccc} u_x & \gamma_y & M_y^A & -V_x^A & -u_y & \gamma_x & M_x^A & V_y^A \end{array} \right\}^T, \tag{D.4}$$

while the boundary conditions at the cantilevered end are

$$\{S\} = \left\{ \begin{array}{cccccccc} 0 & 0 & M_y^R & -V_x^R & 0 & 0 & M_x^R & V_y^R \end{array} \right\}^T. \tag{D.5}$$

The superscripts R and A denote 'reaction' and 'applied', respectively. Applying these boundary conditions allows for Eq. D.3 to be split into two relationships. The first relates the deflections at the free end to the support reactions:

$$\left\{ \begin{array}{c} u_x \\ \gamma_y \\ -u_y \\ \gamma_x \end{array} \right\} = \begin{bmatrix} U_{13} & U_{14} & U_{17} & U_{18} \\ U_{23} & U_{24} & U_{27} & U_{28} \\ U_{53} & U_{54} & U_{57} & U_{58} \\ U_{63} & U_{64} & U_{67} & U_{68} \end{bmatrix} \left\{ \begin{array}{c} M_y^R \\ -V_x^R \\ M_x^R \\ V_y^R \end{array} \right\}, \tag{D.6}$$

where the subscript on the entries denotes position within the overall transfer matrix $[U]$. The second relates the applied loading conditions to the support reactions:

$$\left\{ \begin{array}{c} M_y^A \\ -V_x^A \\ M_x^A \\ V_y^A \end{array} \right\} = \begin{bmatrix} U_{33} & U_{34} & U_{37} & U_{38} \\ U_{43} & U_{44} & U_{47} & U_{48} \\ U_{73} & U_{74} & U_{77} & U_{78} \\ U_{83} & U_{84} & U_{87} & U_{88} \end{bmatrix} \left\{ \begin{array}{c} M_y^R \\ -V_x^R \\ M_x^R \\ V_y^R \end{array} \right\}. \tag{D.7}$$

Equations D.6 and D.7 are re-written as:

$$\{\delta\} = [Z_1]\{F\}^R \tag{D.8}$$

and

$$\{F\}^A = [Z_2]\{F\}^R. \tag{D.9}$$

Relating the above two equations provides an expression for the compliance matrix of the entire system:

$$\{\delta\} = [Z_2][Z_1]^{-1}\{F\}^A = [C]\{F\}^A \tag{D.10}$$

where the overall compliance matrix is $[C]$, the vector of applied loadings is $\{F\}^A$, and the vector of displacements is $\{\delta\}$. The components of $[C]$ are the following (keep in mind that the c_{ij} terms are the additional compliances introduced by the crack, as discussed in Chapter 3):

$$[C] = \begin{bmatrix} C_{11} & -c_{45}L_2^2 & c_{45}L_2 & C_{14} \\ -c_{45}L_2^2 & C_{22} & C_{23} & -c_{45}L_2 \\ c_{45}L_2 & C_{32} & C_{33} & c_{45} \\ C_{41} & -c_{45}L_2 & c_{45} & C_{44} \end{bmatrix} \tag{D.11}$$

where

$$C_{11} = c_{22} + c_{44}L_2^2 + \frac{(L_1+L_2)^3}{3EI} \tag{D.12}$$

$$C_{22} = c_{33} + c_{55}L_2^2 + \frac{(L_1+L_2)^3}{3EI} \tag{D.13}$$

$$C_{33} = c_{55} + \frac{(L_1+L_2)}{EI} \tag{D.14}$$

$$C_{44} = c_{44} + \frac{(L_1+L_2)}{EI} \tag{D.15}$$

and

$$C_{14} = C_{41} = c_{44}L_2 + \frac{(L_1+L_2)^2}{2EI} \tag{D.16}$$

$$C_{23} = C_{32} = -c_{55}L_2 - \frac{(L_1+L_2)^2}{2EI}. \tag{D.17}$$

As expected, the compliance matrix reduces to that of an Euler-Bernoulli beam of length $L_1 + L_2$ when the crack compliances are set to zero.

APPENDIX E

DEVELOPMENT OF THE REAL TRANSFER MATRIX

Recall the general 8×1 state vector for the Real Transfer Matrix defined in a rotating reference frame

$$\{S\}_j = \{\ u_X \quad \gamma_Y \quad M_Y \quad -V_X \quad -u_Y \quad \gamma_X \quad M_X \quad V_Y\}^T \ , \tag{E.1}$$

and an inertial reference frame

$$\{S\}_j = \{\ u_\xi \quad \gamma_\eta \quad M_\eta \quad -V_\xi \quad -u_\eta \quad \gamma_\xi \quad M_\xi \quad V_\eta\}^T \ , \tag{E.2}$$

where the state vector quantities have been previously defined in Chapter 4. A point element is shown in Fig. E.1 for clarity. Though coordinates X and Y are shown, the figure is equally valid for inertial coordinates ξ and η. The point matrix is derived in an inertial and rotating reference frame; the works by Lee and Green [7] and Varney and Green [2] provide comprehensive derivations for the Real Transfer Matrix and asymmetric field matrix, respectively.

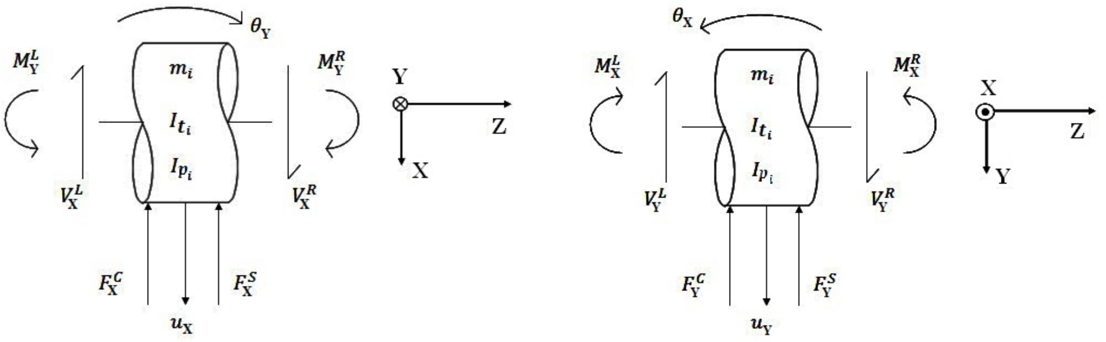

(a) Bending in the XZ plane (b) Bending in the YZ plane

Figure E.1: Point element formulation

E.1 Point Matrix Derivation

E.1.1 Inertial Reference Frame

The point matrix is a condensation of the steady-state equations of motion and continuity conditions for a single lumped inertia. Newton-Euler mechanics are used to formulate the equations of motion. The loads on a point element are due to internal shear and bending reactions as well as external stiffness and damping. These loads are shown on the free-body diagram in Fig. E.1, where the external stiffness and damping forces are designated F_j^S and F_j^C, respectively. These forces are represented in matrix form, where the stiffness forces are

$$\left\{ \begin{array}{c} F_\xi^S \\ F_\eta^S \end{array} \right\} = - \begin{bmatrix} k_{\xi\xi} & k_{\xi\eta} \\ k_{\eta\xi} & k_{\eta\eta} \end{bmatrix} \left\{ \begin{array}{c} u_\xi \\ u_\eta \end{array} \right\} \tag{E.3}$$

and the damping forces are

$$\left\{ \begin{array}{c} F_\xi^C \\ F_\eta^C \end{array} \right\} = - \begin{bmatrix} d_{\xi\xi} & d_{\xi\eta} \\ d_{\eta\xi} & d_{\eta\eta} \end{bmatrix} \left\{ \begin{array}{c} \dot{u}_\xi \\ \dot{u}_\eta \end{array} \right\}. \tag{E.4}$$

Equating the dynamic and applied forces on point element j provides two equations of motion (see Appendix A for details):

$$m_j \ddot{u}_\xi = V_\xi^R - V_\xi^L - F_\xi^C - F_\xi^S \tag{E.5}$$

$$m_j \ddot{u}_\eta = V_\eta^R - V_\eta^L - F_\eta^C - F_\eta^S. \tag{E.6}$$

Expressing the angular momentum about the rotor's center of mass decouples the linear and angular degrees of freedom (see Appendix A for a formulation of the angular momentum). Equating dynamic and applied moments provides the equations of motion governing the point element's angular motion:

$$I_t \ddot{\gamma}_\xi + I_p n \dot{\gamma}_\eta = M_\xi^R - M_\xi^L \tag{E.7}$$

$$I_t \ddot{\gamma}_\eta - I_p n \dot{\gamma}_\xi = M_\eta^R - M_\eta^L. \tag{E.8}$$

Expressing kinematic continuity across the point element gives the following relations:

$$u_\xi^R = u_\xi^L \tag{E.9}$$

$$u_\eta^R = u_\eta^L \tag{E.10}$$

$$\gamma_\xi^R = \gamma_\xi^L \tag{E.11}$$

$$\gamma_\eta^R = \gamma_\eta^L. \tag{E.12}$$

Steady-state conditions are assumed such that the complex-valued response of each state vector quantity occurs at a frequency equal to the whirl frequency p. Assuming steady-state conditions provides the following equations, written such that the state vector quantities on the right are a function of those on the left:

$$\begin{aligned}
u_\xi^R &= u_\xi^L \\
\gamma_\eta^R &= \gamma_\eta^L \\
M_\eta^R &= -I_t\, p^2 \gamma_\eta^L - i I_p\, p\, n\, \gamma_\xi^L + M_\eta^L \\
V_\xi^R &= (-m\, p^2 + i\, d_{\xi\xi}\, p + k_{\xi\xi})\, u_\xi^L \\
&\quad + (i\, d_{\xi\eta} p + k_{\xi\eta})\, u_\eta^L + V_\xi^L \\
u_\eta^R &= u_\eta^L \\
\gamma_\xi^R &= \gamma_\xi^L \\
M_\xi^R &= -I_t\, p^2 \gamma_\xi^L + i I_p\, p\, n\, \gamma_\eta^L + M_\xi^L \\
V_\eta^R &= (-m\, p^2 + i\, d_{\eta\eta}\, p + k_{\eta\eta})\, u_\eta^L \\
&\quad + (i\, d_{\eta\xi}\, p + k_{\eta\xi})\, u_\xi^L + V_\eta^L.
\end{aligned} \tag{E.13}$$

Placing these equations into matrix form provides the point matrix $[P_j]$ for the j^{th} point element in an inertial frame:

$$[P_j]^{IF}_{8\times 8} = \begin{bmatrix} 1 & 0 & 0 & 0 & 0 & 0 & 0 & 0 \\ 0 & 1 & 0 & 0 & 0 & 0 & 0 & 0 \\ 0 & -I_t p^2 & 1 & 0 & 0 & -iI_p np & 0 & 0 \\ mp^2 - id_{\xi\xi}p - k_{\xi\xi} & 0 & 0 & 1 & id_{\xi\eta}p + k_{\xi\eta} & 0 & 0 & 0 \\ 0 & 0 & 0 & 0 & 1 & 0 & 0 & 0 \\ 0 & 0 & 0 & 0 & 0 & 1 & 0 & 0 \\ 0 & iI_p np & 0 & 0 & 0 & -I_t p^2 & 1 & 0 \\ id_{\eta\xi}p + k_{\eta\xi} & 0 & 0 & 0 & mp^2 - id_{\eta\eta}p - k_{\eta\eta} & 0 & 0 & 1 \end{bmatrix}. \tag{E.14}$$

E.1.2 Rotating Reference Frame

A similar procedure gives the point matrix in a rotating reference frame (as derived by Casey [37]), though external stiffness and damping forces are excluded (these can be included using the Complex Extended Transfer Matrix). The corresponding rotating frame acceleration and angular momentum is provided in Appendix A; upon assuming a steady-state solution to the elemental equations of motion, the transfer matrices in a rotating reference frame can be found. In the rotating frame, the response occurs at the relative whirl frequency p_r. The rotating-frame point matrix is

$$[P_j]^{RF}_{8\times 8} = \begin{bmatrix} [D]_{4\times 4} & -[G]_{4\times 4} \\ [G]_{4\times 4} & [D]_{4\times 4} \end{bmatrix}, \tag{E.15}$$

where

$$[D]_{4\times 4} = \begin{bmatrix} 1 & 0 & 0 & 0 \\ 0 & 1 & 0 & 0 \\ 0 & (I_p - I_t)\, n^2 - I_t\, p_r^2 & 1 & 0 \\ m\,(p_r^2 + n^2) & 0 & 0 & 1 \end{bmatrix} \tag{E.16}$$

and

$$[G]_{4\times4} = \begin{bmatrix} 0 & 0 & 0 & 0 \\ 0 & 0 & 0 & 0 \\ 0 & -i(2I_t - I_p)np_r & 0 & 0 \\ 2i\,m\,n\,p_r & 0 & 0 & 0 \end{bmatrix}. \tag{E.17}$$

APPENDIX F

DETAILS OF THE COMPLEX TRANSFER MATRIX

The ability to distinguish forward and backward whirl is the primary advantage of the Complex Transfer Matrix (CTM) over the Real Transfer Matrix (RTM). The CTM method is first developed by Varney and Green [36]. The distinction between the methods is seen through analysis of the simple overhung rotordynamic system shown in Fig. F.1. The discrete system consists of a single lumped mass at the rotor (point matrix $[P]$) and one massless beam with flexural rigidity EI and length L (field matrix $[F]$). The transfer matrix method then gives

$$\{S\}^{FE} = [U]\{S\}^{SU}, \tag{F.1}$$

where the overall transfer matrix $[U]$ is

$$[U] = [P][F]. \tag{F.2}$$

The superscripts FE and SU designate the free end and support, respectively. A symbolic analysis elucidates why the CTM method separates forward and backward

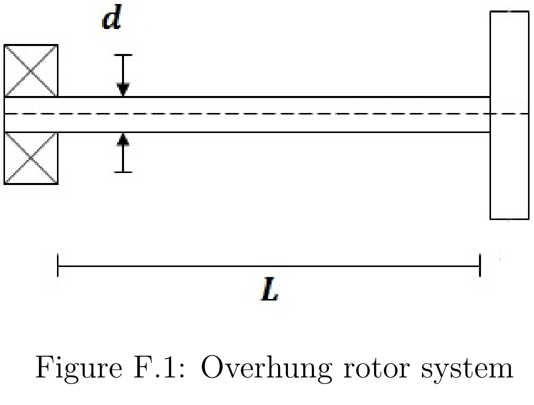

Figure F.1: Overhung rotor system

whirl, while a numeric analysis demonstrates the separation. The analysis is performed for both a rotating and inertial reference frame.

F.1 Inertial Frame

Chapter 4 gives the inertial point and field matrices for the RTM and CTM methods. The characteristic equation is found as a function of the shaft speed n, the absolute whirl frequency p, and the physical parameters of the system. Using the RTM, the characteristic equation for the generally non-synchronous, undamped system is

$$Q(p) = a_8\,p^8 + a_6\,p^6 + a_4\,p^4 + a_2\,p^2 + 1 = 0. \tag{F.3}$$

For the undamped cantilevered system discussed above, the coefficients of Eq. F.3 are evaluated symbolically and summarized in Table F.1 (inclusion of damping generates odd powers of p in the characteristic equation). The constants A, B, and C are a function of only the system's physical parameters (but do not include the shaft speed). It is clear from Table F.1 that the shaft speed n appears in the characteristic equation only in even powers; the same eigenvalues p are therefore obtained regardless of whether n is positive or negative. Therefore, the RTM is incapable of naturally distinguishing forward and backward whirl directions. For a general system composed of many point masses and beam segments, the same ambiguity persists.

In comparison, the CTM generates the following generally non-synchronous characteristic equation:

$$Q(p) = b_4\,p^4 + b_3\,p^3 + b_2\,p^2 + b_1\,p + 1 = 0. \tag{F.4}$$

The coefficients of Eq. F.4 are given in Table F.1. In this case, it is clear that different eigenvalues are obtained when n is either positive or negative (i.e., forward or backward, respectively). This unique trait of the CTM precipitates separation of forward and backward whirl, as forward and backward whirl depend on the sign of n.

Table F.1: Characteristic equation coefficients

	RTM		CTM
a_8	$\dfrac{(I_t^2 - I_p^2)L^8 m^2}{144E^4 I^4}$	b_4	$\dfrac{I_t m L^4}{12E^2 I^2}$
a_6	$A - \dfrac{I_p^2 m^2 L^8}{144E^4 I^4} n^2$	b_3	$\dfrac{-I_p m L^4}{12E^2 I^2} n$
a_4	$B + \dfrac{I_p^2 m L^5}{6E^3 I^3} n^2$	b_2	$\dfrac{-mL^3 - 3I_t L}{3EI}$
a_2	$C - \dfrac{I_p^2 L^2}{E^2 I^2} n^2$	b_1	$\dfrac{I_p L}{EI} n$

The synchronous whirl characteristic equations provide further insight into the CTM's unique separation capability. The forward and backward synchronous whirl characteristic equations obtained using the CTM are, respectively:

$$\frac{mL^4(I_t - I_p)}{12E^2I^2}p^4 + \frac{L(3I_p - 3I_t - mL^2)}{3EI}p^2 + 1 = 0 \tag{F.5}$$

and

$$\frac{mL^4(I_t + I_p)}{12E^2I^2}p^4 - \frac{L(3I_p + 3I_t + mL^2)}{3EI}p^2 + 1 = 0. \tag{F.6}$$

However, the characteristic equations found using the RTM are identical for forward and backward synchronous whirl. Distinction of forward and backward whirl is therefore impossible without further analysis. Moreover, these identical characteristic equations are merely a product of the characteristic equations found using the CTM for forward and backward synchronous whirl (i.e., the product of Eqs. F.5 and F.6).

For each point matrix included in the overall transfer matrix, the order of the characteristic equation is incremented by either four (CTM) or eight (RTM). Therefore, for N point elements, the order of the characteristic equation is either $4N$ (CTM) or

$8N$ (RTM). For systems with many point elements, the use of the RTM generates a characteristic equation of prohibitively high order. Hence, one advantage of the CTM is clear: the order of the characteristic equation is reduced by a factor of 2. The decrease in the order of the characteristic equation results in a significant decrease in computation time and increased accuracy of the roots.

F.2 Rotating Frame

Though the rotating frame RTM separates forward and backward whirl, it suffers from an additional shortcoming. Extraneous roots are found when the backward synchronous whirl line intersects the superfluous lines of the Campbell diagram generated by mirroring (this mirroring inhibits graphical separation of forward and backward whirl). When using the RTM in a rotating frame, care must be taken to distinguish true synchronous whirl speeds from extraneous speeds. For the backward synchronous whirl, the characteristic equation found using the rotating frame RTM can be factored in the following form:

$$Q_{tot} = Q_1 Q_2, \tag{F.7}$$

where Q_{tot} is the total characteristic equation and Q_1 and Q_2 are polynomial factors of Q_{tot}. For the simple cantilevered system, these polynomials are

$$Q_1 = \frac{mL^4(I_p + I_t)}{3(8EI)^2} p_r^4 - \frac{L(3I_p + 3I_t + mL^2)}{12EI} p_r^2 + 1 \tag{F.8}$$

and

$$Q_2 = \frac{9mL^4(3I_t - I_p)}{(8EI)^2} p_r^4 - \frac{3L(-3I_p + 9I_t + mL^2)}{4EI} p_r^2 + 1. \tag{F.9}$$

The roots of Eq. F.8 provide the backward synchronous whirl frequencies, while the roots of Eq. F.9 correspond to the equation's extraneous roots. This issue is circumvented by using the CTM, as the method provides only the correct roots (as well as inherently distinguishing forward and backward whirl).

Table F.2: Parameters of the example system

m	91.9 kg
I_t	1.436 $kg \cdot m^2$
I_p	0.718 $kg \cdot m^2$
E	206.9 GPa
L	0.2 m
d	0.05 m

F.3 Numeric Analysis

The RTM and CTM are used to analyze the simple system shown in Fig. F.1. The analysis is performed in both inertial and rotating reference frames. The diameter of the circular cross-section overhung shaft is d, with elastic modulus E and cross-sectional area moment of inertia I. The mass of the shaft of length L is assumed to be massless compared to the rotor. The parameters of the system are summarized in Table F.2. These parameters are chosen so that a majority of the whirl speeds are relatively close in magnitude, so as to best demonstrate the differences between the RTM and CTM methods.

F.3.1 Inertial Reference Frame

Inertial frame Campbell diagrams are generated using the RTM (Fig. F.2) and the CTM (Fig. F.3). It is clear from Fig. F.2 that the RTM is incapable of separating forward and backward whirl; each whirl speed, both synchronous and non-synchronous, is mirrored across the horizontal shaft speed axis. The ability of the CTM to distinguish these frequencies is seen in Fig. F.3, as each synchronous whirl speed is unique.

F.3.2 Rotating Reference Frame

The synchronous whirl speeds and Campbell diagram are also given for a rotating reference frame. Figures F.4 and F.5 provide the Campbell diagrams generated using the RTM and CTM in a rotating frame, respectively. Comparison of Figs. F.4

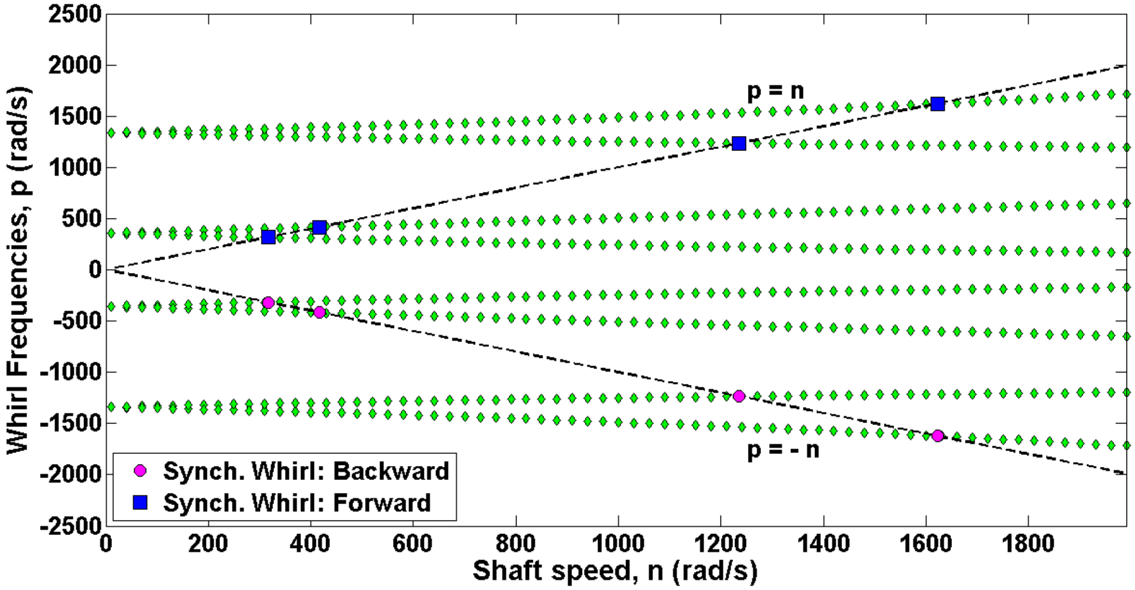

Figure F.2: Campbell diagram: RTM, inertial frame

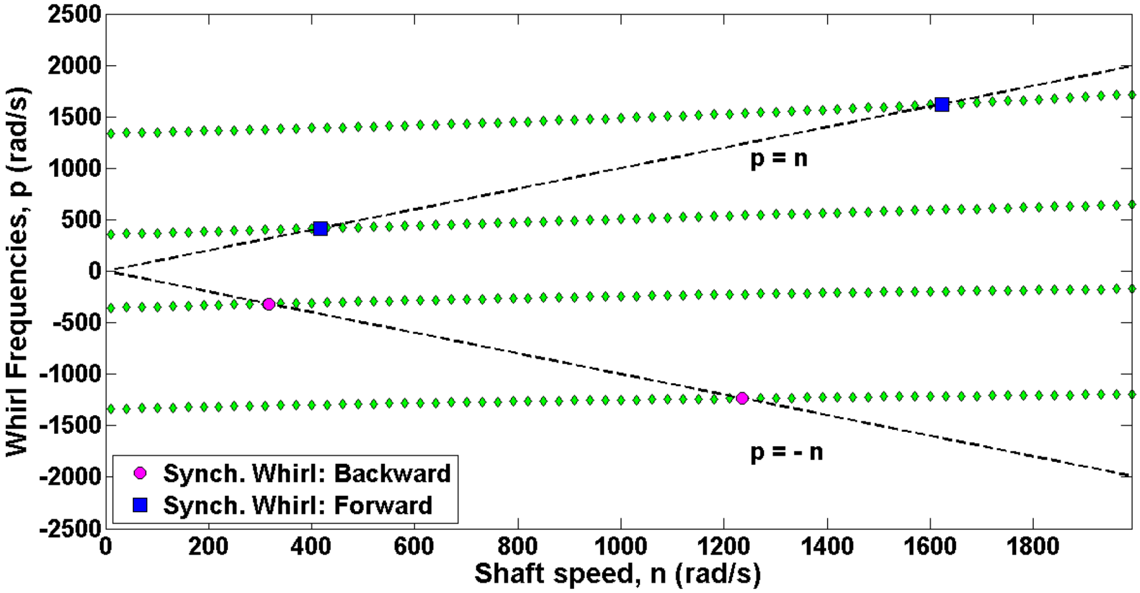

Figure F.3: Campbell diagram: CTM, inertial frame

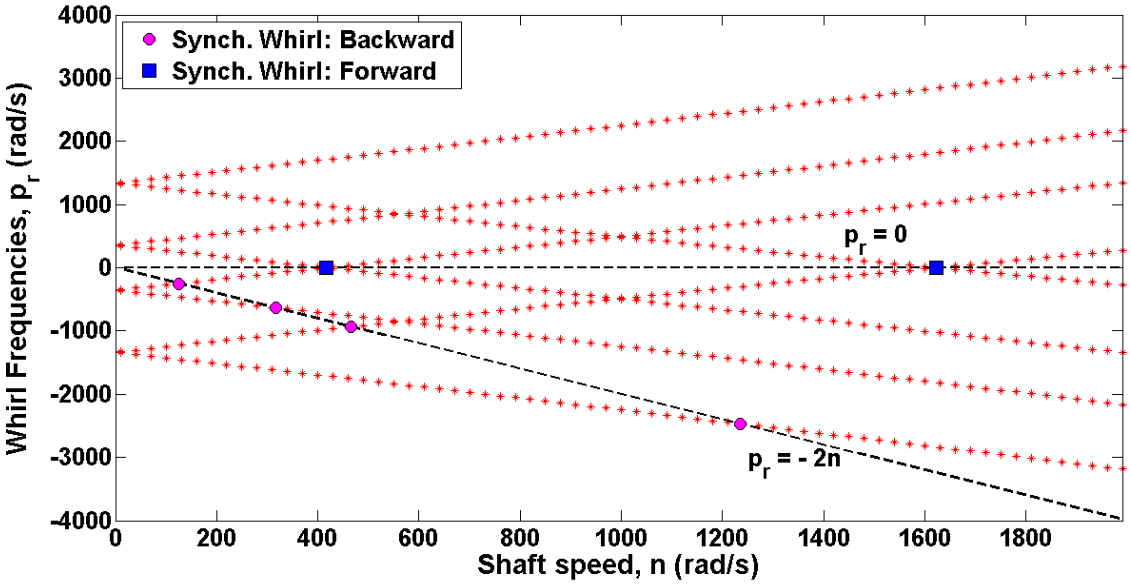

Figure F.4: Campbell diagram: RTM, rotating frame

and F.5 exposes superfluous synchronous whirl frequencies, as discussed prior. The extraneous frequencies are identified in Fig. F.4 as the frequencies corresponding to intersections of the $p = -2n$ line with the locus of frequencies displaying a positive slope. The frequencies are clearly extraneous, as they are not corroborated by either the inertial frame transfer matrix analysis or the rotating frame CTM analysis (Fig. F.5). As expected, the rotating reference frame adaptation of the CTM distinguishes forward and backward whirl while simultaneously eliminating the superfluous whirl frequencies.

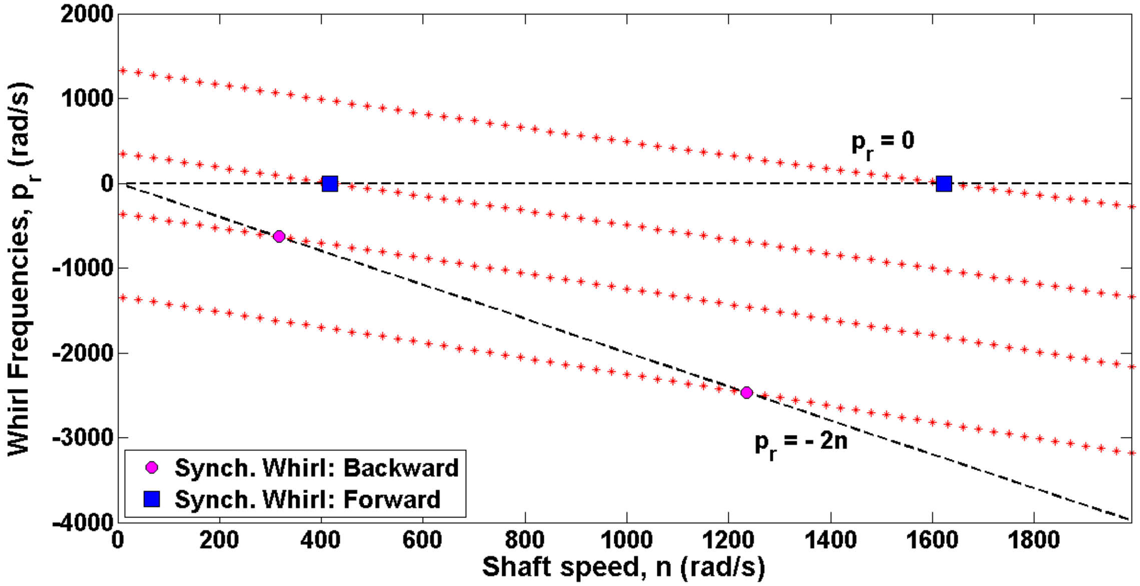

Figure F.5: Campbell diagram: CTM, rotating frame

REFERENCES

[1] Green, I., and Casey, C., 2005. "Crack Detection in a Rotor Dynamic System by Vibration Monitoring—Part I: Analysis". *ASME Journal of Engineering for Gas Turbines and Power,* ***127***(2), pp. 425 – 436.

[2] Varney, P., and Green, I., 2012. "Crack Detection in a Rotor Dynamic System by Vibration Monitoring - Part II: Extended Analysis and Experimental Results". *ASME Journal of Engineering for Gas Turbines and Power,* ***134***(11), pp. 112501.1 – 112501.10.

[3] Bently, D., and Muszynska, A., 1986. "Early Detection of Shaft Cracks on Fluid-handling Machines". *Proceedings of ASME International Symposium on Fluid Machinery Trouble Shooting. 1986 Winter Annual Meeting, Anaheim, California,* ***7***, December, pp. 53 – 58.

[4] Sabnavis, G., Kirk, R. G., Kasarda, M., and Quinn, D., 2004. "Cracked Shaft Detection and Diagnostics: A Literature Review". *Shock and Vibration Digest,* ***36***, pp. 287 – 296.

[5] Green, I., and Etsion, I., 1986. "A Kinematic Model for Mechanical Seals with Antirotating Locks or Positive Drive Devices". *ASME Journal of Tribology,* ***108***(1), pp. 42 – 45.

[6] Green, I., 2008. "On the Kinematics and Kinetics of Mechanical Seals, Rotors, and Wobbling Bodies". *Mechanism and Machine Theory,* ***43***(7), pp. 909 – 917.

[7] Lee, A., and Green, I., 1994. "Rotordynamics of a Mechanical Face Seal Riding on a Flexible Shaft". *ASME Journal of Tribology,* ***116***(2), pp. 345 – 351.

[8] Lee, A., and Green, I., 1994. "Higher Harmonic Oscillations in a Non-contacting FMR Mechanical Face Seal Test Rig". *ASME Journal of Vibration and Acoustics,* ***116***(2), pp. 161 – 167.

[9] Lee, A., and Green, I., 1995. "Physical Modeling and Data Analysis of the Dynamic Response of a Flexibly Mounted Rotor Mechanical Seal". *ASME Journal of Tribology,* ***117***, pp. 130 – 135.

[10] Zou, M., Dayan, J., and Green, I., 2000. "Dynamic Simulation and Monitoring of a Non-Contacting Flexibly Mounted Rotor Mechanical Face Seal". *Proceedings of the Institution of Mechanical Engineers, Part C: Journal of Mechanical Engineering Science,* ***214***(9), pp. 1195 – 1206.

[11] Zou, M., and Green, I., 1999. "Clearance Control of a Mechanical Face Seal". *Tribology Transactions,* ***42***(3), pp. 535 – 540.

[12] Zou, M., Dayan, J., and Green, I., 2000. "Feasibility of Contact Elimination of a Mechanical Face Seal Through Clearance Adjustment". *Journal of Engineering for Gas Turbines and Power,* ***122***, pp. 478 – 484.

[13] Dayan, J., Zou, M., and Green, I., 2002. "Contact Elimination in Mechanical Face Seals Using Active Control". *Control Systems Technology, IEEE Transactions,* ***10***(3), pp. 344 – 354.

[14] Dimarogonas, A., and Paipetis, S., 1983. *Analytical Methods in Rotor Dynamics.* Applied Science Publishers.

[15] Papadopoulos, C. A., and Dimarogonas, A. D., 1987. "Coupled Longitudinal and Bending Vibrations of a Rotating Shaft With an Open Crack". *Journal of Sound and Vibration,* ***117***(1), pp. 81 – 93.

[16] Dimarogonas, A. D., 1996. "Vibration of Cracked Structures: A State of the Art Review". *Engineering Fracture Mechanics,* ***55***, pp. 831 – 857.

[17] Silva, J., and Gomez, A., 1990. "Experimental Dynamic Analysis of Cracked Free-Free Beams". *Experimental Mechanics,* ***30***(1), pp. 20 – 25.

[18] Gomez, A., and Silva, J., 1991. "Theoretical and Experimental Data on Crack Depth Effects in the Dynamic Behaviour of Free-Free Beams". In 9th International Modal Analysis Conference (IMAC), Vol. 1, pp. 274 – 283.

[19] Rao, J. S., 1996. *Rotor Dynamics*, 3rd ed. New Age International, New Delhi.

[20] Mayes, I., and Davies, W., 1976. "The Vibrational Behaviour of a Rotating Shaft System Containing a Transverse Crack". *Conference on Vibrations in Rotating Machinery*, pp. 53 – 64.

[21] Inagaki, T., Kanki, H., and Shiraki, K., 1982. "Transverse Vibrations of a General Cracked Rotor Bearing System". *Journal of Mechanical Design,* ***104***, pp. 1 – 11.

[22] Sinou, J., 2009. "An Experimental Investigation of Condition Monitoring for Notched Rotors Through Transient Signals and Wavelet Transform". *Experimental Mechanics,* ***49***(5), pp. 683 – 695.

[23] Dimarogonas, A., and Papadopoulos, C., 1983. "Vibration of Cracked Shafts in Bending". *Journal of Sound and Vibration,* ***91***(4), pp. 583 – 593.

[24] Irwin, G., 1957. "Analysis of Stresses and Strains Near the End of a Crack Traversing a Plate". *Journal of Applied Mechanics.*

[25] Papadopoulos, C. A., and Dimarogonas, A. D., 1988. "Coupled Longitudinal and Bending Vibrations of a Cracked Shaft". *ASME Journal of Vibration, Acoustics, and Stress Reliability Design,* ***110***(1), pp. 1 – 8.

[26] Papadopoulos, C., and Dimarogonas, A., 1992. "Coupled Vibration of Cracked Shafts". *Journal of Vibration and Acoustics,* ***114***, p. 461.

[27] Gounaris, G., Papadopoulos, C., and Dimarogonas, A., 1996. "Crack Identification in Beams by Coupled Response Measurements". *Journal of Computers and Structures,* ***58***(2), pp. 299 – 305.

[28] Gounaris, G., and Papadopoulos, C., 2002. "Crack Identification in Rotating Shafts by Coupled Response Measurements". *Engineering Fracture Mechanics,* ***69***(3), pp. 339 – 352.

[29] Papadopoulos, C., 2008. "The Strain Energy Release Approach for Modeling Cracks in Rotors: A State of the Art Review". *Mechanical Systems and Signal Processing,* ***22***(4), pp. 763 – 789.

[30] Papadopoulos, C. A., 2004. "Letter to the Editor: Some Comments on the Calculation of the Local Flexibility of Cracked Shafts". *Journal of Sound and Vibration,* ***278***, pp. 1205 – 1211.

[31] Darpe, A., Gupta, K., and Chawla, A., 2004. "Coupled Bending, Longitudinal and Torsional Vibrations of a Cracked Rotor". *Journal of Sound and Vibration,* ***269***(1), pp. 33 – 60.

[32] Penny, J. E. T., and Friswell, M. I., 2007. "The Dynamics of Cracked Rotors". Structural dynamics; IMAC XXV, pp. 198 – 207.

[33] Inagaki, T., Kanki, H., and Shiraki, K., 1980. "Response Analysis of a General Asymmetric Rotor-Bearing System". *Journal of Mechanical Design,* ***102***, pp. 147 – 157.

[34] Pestel, E., and Leckie, F., 1963. *Matrix Methods in Elastomechanics.* McGraw-Hill New York.

[35] Genta, G., 2005. *Dynamics of Rotating Systems.* Mechanical Engineering Series. New York, NY : Springer Science+Business Media, Inc., 2005.

[36] Varney, P., and Green, I., 2012. "Rotordynamic Analysis using the Complex Transfer Matrix". ASME IDETC/CIE.

[37] Casey, C., 2000. "Crack Detection in a Rotordynamic System by Vibration Monitoring". Master's thesis, Georgia Institute of Technology.

[38] Grabowski, B., 1980. "The Vibrational Behavior of a Turbine Rotor Containing a Transverse Crack". *ASME, Transactions, Journal of Mechanical Design,* ***102***, pp. 140 – 146.

[39] Wauer, J., 1990. "Modeling and Formulation of Equations of Motion for Cracked Rotating Shafts". *International Journal of Solids and Structures,* ***26***(8), pp. 901 – 914.

[40] Gasch, R., 2008. "Dynamic Behaviour of the Laval Rotor With a Transverse Crack". *Mechanical Systems and Signal Processing,* ***22***(Special Issue: Crack Effects in Rotordynamics), pp. 790 – 804.

[41] Gasch, R., 1976. "Dynamic Behavior of a Simple Rotor with a Cross-sectional Crack". *Vibrations in Rotating Machinery*, pp. 123 – 128.

[42] Szolc, T., Tauzowski, P., Knabel, J., and Stocki, R., 2004. "Nonlinear and Parametric Coupled Vibrations of the Rotor-Shaft System as Fault Identification Symptom Using Stochastic Methods". *Nonlinear Dynamics,* ***57***(4), pp. 533 – 557.

[43] Wu, X., Meagher, J., and Judd, C., 2007. "Investigation of Coupled Lateral and Torsional Vibrations of a Cracked Rotor Under Radial Load". In Proceedings of IMAC, Structural Dynamics; IMAC XXV, pp. 103 – 302.

[44] Wu, X., and Meagher, J., 2008. "A Two-Disk Extended Jeffcott Rotor Model Distinguishing a Shaft Crack from Other Rotating Asymmetries". *International Journal of Rotating Machinery.*

[45] Sawicki, J. T., Wu, X., Gyekenyesi, A. L., and Baaklini, G. Y., 2005. "Application of Nonlinear Dynamics Tools for Diagnosis of Cracked Rotor Vibration Signatures". In Proceedings - SPIE The International Society for Optical Engineering, Nondestructive Evaluation and Health Monitoring of Aerospace Materials, Composites, and Civil Infrastructure IV, pp. 286 – 297.

[46] Ferfecki, P., 2007. "Study of Coupling Between Bending and Torsional Vibration of Cracked Rotor System Supported by Radial Active Magnetic Bearings". *Applied and Computational Mechanics,* ***1***(2), pp. 427 – 436.

[47] Darpe, A. K., 2007. "A Novel Way to Detect Transverse Surface Crack in a Rotating Shaft". *Journal of Sound and Vibration,* ***305***, pp. 151 – 171.

[48] Patel, T. H., and Darpe, A. K., 2007. "Influence of Crack Breathing Model on Nonlinear Dynamics of a Cracked Rotor". *Journal of Sound and Vibration,* ***311***, pp. 953 – 972.

[49] Patel, T. H., and Darpe, A. K., 2009. "Coupled Bending-Torsional Vibration Analysis of Rotor with Rub and Crack". *Journal of Sound and Vibration,* ***326***, pp. 740 – 752.

[50] Singh, S., and Tiwari, R., 2010. "Identification of a Multi-Crack in a Shaft System Using Transverse Frequency Response Functions". *Mechanism and Machine Theory,* ***45***, pp. 1813 – 1827.

[51] Bachschmid, N., Pennacchi, P., Tanzi, E., and Vania, A., 2000. "Identification of Transverse Crack Position and Depth in Rotor Systems". *Meccanica,* ***35***(6), pp. 563 – 582.

[52] Quinn, D., Mani, G., Kasarda, M., Bash, T., Inman, D., and Kirk, R., 2005. “Damage Detection of a Rotating Cracked Shaft Using an Active Magnetic Bearing as a Force Actuator - Analysis and Experimental Verification”. *IEEE-ASME Transactions on Mechatronics,* ***10***, pp. 640 – 647.

[53] Bucher, I., and Ewins, D. J., 2001. “Modal Analysis and Testing of Rotating Structures”. *Philosophical Transactions: Mathematical, Physical and Engineering Sciences,* ***359***, pp. 61 – 96.

[54] Bently, D. E., Goldman, P., and Muszynska, A., 1997. “”Snapping” Torsional Response of an Anisotropic Radially Loaded Rotor”. *ASME Journal of Engineering for Gas Turbines and Power,* ***119***, pp. 397 – 403.

[55] Imam, I., Azzaro, S., Bankert, R. J., and Scheibel, J., 1989. “Development of an Online Rotor Crack Detection and Monitoring System”. *Journal of Vibration, Acoustics, Stress and Reliability in Design,* ***111***, pp. 241 – 250.

[56] Nagaraju, C., Narayana, Rao, K., Mallikarjuna, and Rao, K., 2009. “Application of 3D Wavelet Transforms for Crack Detection in Rotor Systems”. *Sadhana,* ***34***(3), pp. 407 – 419.

[57] Ding, Q., 2004. “Backward Whirl and Its Suppression of a Squeeze Film Damper Mounted Rotor/Casing System in Passage through Critical Speed with Rubs”. *Journal of Vibration and Control,* ***10***(4), p. 561.

[58] Jiang, J., 2007. “The Analytical Solution and the Existence Condition of Dry Friction Backward Whirl in Rotor-to-Stator Contact Systems”. *Journal of Vibration and Acoustics,* ***129***, p. 260.

[59] Liao, M., and Gasch, R., 1992. “Crack Detection in Rotating Shafts - An Experimental Study”. In International Conference on Rotating Machinery (IMechE), pp. 289 – 295.

[60] Budynas, R. G., and Nisbett, J. K., 2008. *Shigley’s Mechanical Engineering Design*, 8th ed. McGraw Hill, New York.

[61] Hibbeler, R. C., 2008. *Mechanics of Materials*, 7th ed. Pearson Prentice Hall, New Jersey.

[62] Anderson, T., 2005. *Fracture Mechanics: Fundamentals and Applications.* CRC.

[63] Varney, P., and Green, I., 2012. “Crack Detection in a Rotordynamic System by Vibration Monitoring - Analytical and Experimental Results”. International Joint Tribology Conference.

[64] Varney, P., and Green, I., 2012. “A Comparison of Global Asymmetry and Local Transverse Shaft Cracks in a Rotordynamic System”. STLE Annual Meeting.

[65] Ginsberg, J. H., 2001. *Mechanical and Structural Vibrations: Theory and Applications*, 1st ed. Wiley, New York.

[66] Sanderson, A., 1992. “The Vibration Behaviour of a Large Steam Turbine Generator During Crack Propagation Through the Generator Rotor”. In International Conference on Vibrations in Rotating Machinery (IMechE), Vol. 6, pp. 263 – 273.

[67] Green, I., 1990. “Gyroscopic and Damping Effects on the Stability of a Noncontacting Flexibly-Mounted Rotor Mechanical Face Seal”. *Dynamics of Rotating Machinery*, pp. 153 – 173.